

DESIGN, ANALYSIS, AND INTEGRATION OF
A TURBOELECTRIC PROPULSION AND POWER
SYSTEM FOR UNMANNED AIRCRAFT

By

Kylar Julian Moody

Bachelor of Science in Aerospace Engineering

Bachelor of Science in Mechanical Engineering

Oklahoma State University

Stillwater, OK

2018

Submitted to the Faculty of the
Graduate College of the
Oklahoma State University
in partial fulfillment of
the requirements for
the Degree of
MASTER OF SCIENCE
May, 2020

DESIGN, ANALYSIS, AND INTEGRATION OF
A TURBOELECTRIC PROPULSION AND POWER
SYSTEM FOR UNMANNED AIRCRAFT

Thesis Approved:

Dr. Kurt P. Rouser

Thesis Adviser

Dr. Richard Gaeta

Dr. Jamey Jacob

ACKNOWLEDGEMENTS

First, I would like to thank God for blessing me with the opportunity to attend college and work on an impactful project. I would like to thank my amazing wife Amanda for being so supportive and for loving and caring for me always. I would like to thank my mom, Christy, my dad, Julian, and my nana, Betty, for raising me right, teaching me work ethic, and always encouraging me to do my best even when it is tough. In addition, I would like to thank my advisor, Dr. Kurt Rouser, and committee members, Dr. Richard Gaeta and Dr. Jamey Jacob, for their willingness to share valuable knowledge and resources to assist with my research. I would like to also thank the Mechanical and Aerospace Engineering department faculty and staff for providing facilities and an amazing educational experience. I would like to thank fellow research assistants Nicholas Lucido, Connor McCain, Chase Holland, Cole Replogle, Justin Myers, Matt Durkee, Lauren Jones, Kishankumar Patel and Lucas Utley for assisting with laboratory operations, testing, fabrication, and assembly. I would like to thank Skylar Dennis, Barrett Schwandt, Dolan Motter, and Alex Ott for their significant contribution to installing and testing the system on a vehicle. I would like to offer a special thank you to Dr. Kurt Rouser for investing so much in the project and giving me opportunities I would have otherwise never had; thank you for obtaining funding and sharing your experiences, both professional and personal. Lastly, I would like to thank the sponsors of this project, Baker Hughes: A General Electric Company, and OCAST, the Oklahoma Center for Advancement of Science and Technology.

Name: KYLAR JULIAN MOODY

Date of Degree: MAY, 2020

Title of Study: DESIGN, ANALYSIS, AND INTEGRATION OF A
TURBOELECTRIC PROPULSION AND POWER SYSTEM FOR
UNMANNED AIRCRAFT

Major Field: AEROSPACE AND MECHANICAL ENGINEERING

Abstract: Electrically powered small unmanned aerial systems face limited range and endurance due to the inherently low energy density of current level of technology batteries. Hybrid gas-electric systems are under development and show promising signs of increased range and endurance, however piston based hybrid systems must overcome several challenges to be effective. Turboelectric power systems leverage the high energy density of hydrocarbon fuels in conjunction with the high power density of electric propulsion systems while mitigating some of the typical issues encountered with piston-based hybrid systems. In this study, a 7.3kW turboelectric power system for a small unmanned aircraft is realized through several phases of design, including an airframe integration phase. Though previous literature suggests a range of anticipated electrical efficiencies, the driving factoring contributing to power system losses are not well discussed. Thus, there exists a critical need to develop and validate a design approach that assesses compatibility of components of the electrical system and how component selection affects efficiency. Several overall system models were developed and evaluated for a general turboelectric power system over a range of operating conditions. System level design implications is discussed in detail, enabling optimization of the components during the design phase. An active throttle controller was designed, realized, and evaluated for the system described. The function of the throttle controller ranges from starting and stopping of the turbine to regulation of turbine throttle via feedback control. Switching between power sources and the difficulties associated with this will also be discussed in detail. The turboelectric system was installed on a Mugin 4500 fixed-wing unmanned aerial system and evaluated in terms of thermal management and operability. Results of this study will demonstrate feasibility of turboelectric power systems as an alternative to traditional all-electric propulsion systems and serve as a stepping-stone for future studies on small-scale turboelectric propulsion and power.

TABLE OF CONTENTS

Chapter	Page
I. INTRODUCTION AND RESEARCH QUESTIONS	1
1.1 Introduction and Motivation	1
1.2 Research Questions and Objectives	4
II. REVIEW OF LITERATURE, BACKGROUND, THEORY, AND PRELIMINARY STUDIES	6
2.1 Review of Literature	6
2.2 Background and Theory.....	10
2.2.1 Piston vs. Turbine	10
2.2.2 Energy Density vs. Power Density	13
2.2.3 Hybrid Architecture	14
2.2.4 Turbine Theory	15
2.2.5 Concept of Operation.....	18
2.3 Preliminary Studies.....	19
2.3.1 Mission Analysis.....	20
2.3.2 Baseline Endurance Testing.....	22
III. POWER SYSTEM DESIGN, MODELING, AND VALIDATION	24
3.1 Component Selection.....	24
3.2 Electromechanical System Model.....	26
3.2.1 Rectifier Model	27
3.2.2 Generator Inertial Model.....	29
3.2.3 Generator Electrical Model.....	30
3.2.4 Combined System Model.....	32
3.3 Design of Experiment I: Electrical System Characterization	33
3.4 Test Facility	35
3.5 Results I: Electrical System Characterization and Theoretical Performance ..	36
3.5.1 Friction Losses vs. Rotational Speed.....	36
3.5.2 Theoretical Losses and Electrical Efficiency.....	37
3.5.3 Power System Voltage.....	39
3.5.4 Performance Parameter: Electrical Efficiency vs. Modeled Response...40	
3.6 Turbine Driven Experiment Observations	42

Chapter	Page
3.7 Conclusions, Observations, and Recommendations I: Modeled and Experimental Results.....	43
IV. ELECTRICAL SYSTEM REFINEMENT AND TURBINE THROTTLE CONTROL.....	46
4.1 Stage Loading vs. Current.....	46
4.2 PID Control Theory	49
4.3 Design of Controller: Proportion Control	50
4.3.1 Starting/Stop Turbine.....	51
4.3.2 Voltage Sensing: Rectified Voltage.....	51
4.3.3 Voltage Divider Design	52
4.3.4 Controller Logic.....	53
4.4 Design of Experiment II: Turbine Throttle Control.....	53
4.5 Results II: Proportion Control Response	54
4.5.1 Electrical System Considerations	55
4.5.2 Mechanical System Considerations	57
4.6 Conclusions, Observations, and Recommendations II: Design of Throttle Controller	57
V. FIXED WING VEHICLE INTEGRATION AND TESTING	60
5.1 Vehicle Integration: Mugin 4500.....	60
5.1.1 Propeller Motor Standoffs.....	61
5.1.2 Turboelectric Power System Housing	62
5.1.3 Inlet Sizing	65
5.1.3.1 Turbine Operability.....	66
5.1.3.2 Cooling Requirements	67
5.1.3.3 Inlet Size Calculation.....	69
5.1.4 Completed Integration	71
5.1.4.1 Component Placement	71
5.2 Electrical System Revisions.....	75
5.2.1 Battery Backup	75
5.2.2 Design of Switching Circuit.....	76
5.2.3 Throttle Controller Revisions	77
5.3 Design of Experiment III: Fixed Wing Integration Proof of Concept	78
5.4. Results III: Fixed Wing Integration and Switching Circuit Evaluation.....	80
5.4.1 FLIR Thermal Imaging Results	81
5.4.2 Cabin Temperature Readings.....	82
5.4.3 Switching Circuit Assessment/Troubleshooting.....	82
5.5 Conclusions, Observations, and Recommendations III: Fixed Wing Vehicle Integration.....	84

Chapter	Page
VI. CONCLUSIONS, RECOMMENDATIONS, AND OUTCOMES	86
REFERENCES	92
APPENDICES	97
APPENDIX A: MULTIROTOR INTEGRATION	97
A.1 Stability and Control Considerations	97
A.2 Design Rational.....	101
A.2.1 Revision 1: Fitment and Installation Check	101
A.2.2 Revision 2: Revised Fitment Issues/Weight Reduction	102
A.2.3 Revision 3: Future System	103
A.3 Structural Analysis	104
A.4 Thermal Considerations	107
A.5 Test Flight	109

LIST OF TABLES

Table	Page
1. Results of mission analysis performed comparing piston-hybrid, turboelectric, and all-electric configurations.....	22
2. Results of endurance testing, xFold Travel 12, stock configuration.....	23
3. Components used in experiment for electrical system characterization	33
4. Range and resolution of GT Power inline power meter	34
5. Test matrix evaluated during electrical system characterization	35
6. List of components used in turboelectric test and their power rating	53
7. Mugin 4500 vehicle specifications [39].....	61
8. List of major components for Mugin 4500 turboelectric integration	73
9. List of batteries used and function	74
10. Specifications of driver and switching MOSFETs in switching circuit	77
11. Turboelectric power generation system values of inertia, and angular momentum	98
12. Final revision shelf characteristics.....	104
13. Direct stress on bolts in static case	105
14. Shear stress on bolts in worst case scenario.....	106
15. von Mises stress calculations for bolts, worst case scenario loading	106

LIST OF FIGURES

Figure	Page
1. KingTech K60TP [1] (left) and Turnigy Rotomax 100cc electric motor-generator [2] (right)	2
2. Schematic of natural gas pipeline distribution process [6]	3
3. Figure depicting differences in partial and pure turboelectric systems [12].....	7
4. Desert Aircraft 100CC piston engine [23]	9
5. Comparison of piston engine and gas turbine engine manufacturer specifications.	13
6. Power density vs. energy density of several common propulsion and power systems [28]	14
7. Schematic of series vs. parallel hybrid configurations [21].....	15
8. Temperature entropy diagram of Brayton cycle	17
9. Rendering of proposed concept of operation for rotary (left) and fixed (right) wing turboelectric vehicles	18
10. Schematic of proposed concepts of operation	19
11. Kingtech K60TP [1] (left) and manufacturer power curve (right)	25
12. Equivalent circuit model of three-phase full wave rectifier.....	27
13. Voltage waveform transformation across the rectifier.....	28
14. Current waveform exiting the rectifier	29

Figure	Page
15. Free body diagram of the generator with applied torque	29
16. Equivalent circuit model for BLDC generator.....	30
17. Photo of test setup, including labeled components.....	35
18. Photo of the flexible use wind tunnel test facility.....	36
19. Plot of damping coefficient and total frictional loss vs. shaft speed	37
20. Plot depicting the theoretical electrical efficiency carpet plots as a function of current and shaft speed.....	38
21. Peak theoretical efficiency as a function of current and shaft speed	39
22. Plot of actual voltage vs. shaft speed against modeled values.....	40
23. Plot of theoretical efficiency vs. actual efficiency as a function of shaft speed and current	41
24. Photo of turbine-driven test, first attempt.....	42
25. Stage loading vs current for values of constant voltage	48
26. Schematic of the hybrid system with controller	50
27. Turboelectric system response to proportion control.....	55
28. Mugin 4500 in turboelectric ground test configuration	61
29. SolidWorks assembly of propeller motor standoff	61
30. Photo of propeller motor with standoffs, with and without cowling	62
31. CAD of preliminary turboelectric housing, Rev I	63
32. Prototype turboelectric shelf, initial design	65
33. Benchmarked data for mass flow rate vs. rated thrust	66

Figure	Page
34. Manufacturer specifications for power loss vs. current (left) and maximum ambient temperature with heat sink vs. power loss (right) [41]	67
35. Trade study of mass flow rate of air vs. cabin temperature	68
36. Area required vs airspeed, hot day and standard day estimates.....	69
37. Approximate scale of inlet and exit holes for intake and exhaust air	70
38. Layout of internals, Mugin 4500 airframe	73
39. Section view of the rear compartment of the Mugin 4500	74
40. Integrated turboelectric system showing the updated rectifier location	75
41. Photo of the Mugin 4500 test article, integrated with turboelectric propulsion and power system	79
42. Photo of K-Type thermocouple location relative to turbine exhaust	80
43. FLIR thermal imaging of the Mugin 4500 operating at max thrust.....	82
44. Free body diagram of the dodeca-copter used in the stability and control analysis.....	99
45. First iteration for turboelectric integration.....	102
46. Second iteration for turboelectric shelf.....	103
47. Complete assembly for thermal testing.....	108
48. Experimental leg platform damage during thermal testing.....	108
49. Thermal Imaging data from xFold integration test on mock-up stand	109
50. Weight and structural flight test.....	111

CHAPTER I

INTRODUCTION AND RESEARCH QUESTIONS

1.1 Introduction and Motivation

Hybrid systems are rapidly developing to meet the needs of the developing small Unmanned Aerial Systems (sUAS) market. The sUAS definition according to FAA Part 107 is aircraft FAA in Part 107 as aircraft which weigh less than 55 pounds (including payload) at takeoff; they must also fly in class G airspace within visible line of sight, and below 400 ft. of ceiling at speeds below 100 miles per hour without a waiver. With both commercial and defense sUAS users imposing rigorous mission requirements such as heavy lift capabilities, long range, increased hover endurance, and short takeoff and recovery, the sUAS market is leaning heavily on hybrid electric systems. Hybrid systems offer significant advantages over conventional electric and gas propulsion systems, combining the high power density of batteries with the high energy density of hydrocarbon fuels. Hydrocarbon fuels are on average around 75 times more energy dense than current level of technology batteries, making them more desirable for long range or long endurance missions. Batteries, however, have a higher power density with the capability to discharge at rates of over 400 amps; this is desirable for takeoff, hover, vertical takeoff and landing, short takeoff and landing, and a multitude of other mission requirements. Both rotary-wing and fixed-wing UAS could potentially benefit from the inclusion of a turboelectric propulsion and power system, which is the subject of this current study. Vehicles with adaptive mission profiles, for instance those used with surveying and inspection, would make an excellent testbed for the turboelectric propulsion and power system described in this document; including

both mid-air hover components as well as cruise and loiter components, this type of mission profile best leverages the capabilities of a turboelectric power system



Figure 1. KingTech K60TP [1] (left) and Turnigy Rotomax 100cc electric motor-generator [2] (right)

Though a turbine-based hybrid electric system avoids some of the challenges posed by a piston-based system, both approaches must deal with issues related to overall system efficiency and operability. There is a dearth of existing literature addressing turboelectric system operability; however, overall system efficiency is known to be a function of thermal, propulsive and electrical efficiencies. In general, small combustion engines have low compression ratios due to geometric constraints, resulting in poor thermal efficiency. The hybrid-electric system proposed in this study potentially increases overall efficiency by increasing propulsive efficiency; this is done by distributing power to multiple propulsors at the expense of the electrical efficiency.

The turboelectric power system described has many practical uses among commercial and governmental users. Some potential uses of this technology include but are not limited to long range search and rescue by first responders and law enforcement, atmospheric research, extended endurance flights in cinematography, and even intelligence-surveillance-reconnaissance (ISR) missions within the military. Though there is overlap between the turboelectric system presented and these mission profiles, the motivation for this study is the inspection of oil and natural gas pipeline infrastructure. Over 61 percent of the United States energy comes in the form of oil and natural gas [3], and of the 2.5 million miles of transmission, gathering, and distribution

lines in the United States [4] it is estimated that 60 percent was placed greater than 50 years ago. With this increasing age comes an increasing need for more frequent inspections; the EPA estimates that between 1.9 to 3.1 percent of the natural gas escapes into the atmosphere in a study done over a decade ago, with the number increasing from the previous study [5]. They estimate that about 570 billion cubic feet of natural gas were released because of leaks and venting in the natural gas network between production wells and the local distribution networks in 2009, costing companies billions in lost revenue. This is not to mention the effect on the atmosphere. An overview of the natural gas distribution process can be shown in Fig. 2.

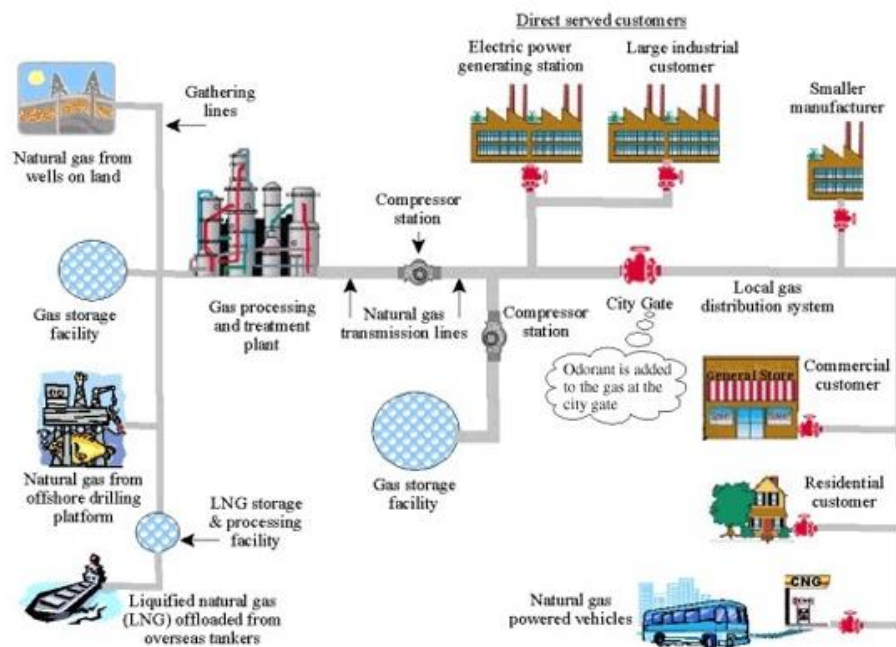


Figure 2: Schematic of natural gas pipeline distribution process [6]

There are several current state non-destructive inspection (NDI) tools used for pipeline inspection. One of these tools is called a PIG (later nicknamed Pipeline Inspection Gadget), named for the sound they make during operation. A PIG is launched into the pipeline and measures wall thickness, so they can detect areas of future trouble, however they cannot be used to detect active leaks. Some companies have taken to the air, employing general aviation aircraft for use in pipeline inspection, however these are generally very high risk and only allow for

visual inspection as the pilot is searching for dead vegetation. More recently, companies have begun utilizing multirotor UAS for this purpose, however the inherently low energy density of current LOT battery technology limits endurance to around 15 minutes with any useful payload. Several UAS manufacturers have begun developing piston-based hybrid systems, which have been shown to effectively increase range and endurance of the vehicle at the expense of increased vibration, additional cooling requirements, and increased system weight. Turbine-based hybrid systems, though not a fuel efficient, can reduce and potentially eliminate all of the above issues encountered when employing a piston-based hybrid system.

1.2 Research Questions and Objectives

The research questions are as follow:

1. What are the system level design considerations when designing a hybrid turboelectric powertrain?
2. What are the vehicle level design considerations when designing a vehicle utilizing a hybrid turboelectric powertrain?
3. Is a turboelectric sUAS a feasible alternative to purely electric sUAS?

Objective I: Develop and evaluate a design tool which focuses on the efficiency and operability of a turboelectric system which also addresses compatibility of the components of the power generation system including the turbine, generator, and rectifier. This design tool will allow for component selection and sizing given a set of component parameters and load characteristics. This will involve development and validation of an analytical model of the power generation system. This is done in order to determine the key system drivers which hinder electrical efficiency. Drivers can range from component parameters, for example resistance or speed rating of electrical components, to mission driven operability requirements, such as the combination of voltage and current needed to operate the aircraft propulsion and power system(s). Several iterations of modeling must be done to ensure that the system is not only behaving as predicted, but to ensure that trade studies and conclusions are accurate and meaningful.

Objective II: Determine vehicle-level challenges and constraints associated with integration and installation of the turboelectric system aboard a fixed-wing aircraft and mitigate/address them. Constraints can range from seemingly simple (e.g., sufficient airflow for turbine operation and cabin cooling) to much more complex (electrical power management and closed-loop feedback control). Active control is essential and is discussed in detail in the latter sections of this document, as well as power management and airframe cooling considerations. In addition to these, there are many other vehicle level considerations discussed in the latter sections of this document.

Objective III: Demonstrate feasibility of turboelectric propulsion and power as an alternative to all electric systems in terms of operability. This objective will entail demonstration of the turboelectric propulsion and power system in conjunction with a traditionally all-electric system. For the prototype airframe, a Mugin 4500 will be outfitted with the turboelectric power system. This system will drive a brushless DC (BLDC) motor and propeller, which will demonstrate feasibility of turboelectric power system. Theory suggests that the hybrid power system will offer advantages in range and endurance compared to the all-electric system, but may suffer in areas such as weight and acoustics. Though this topic is of interest to the UAS community, range and endurance will not be addressed in this feasibility study though it is worth mentioning.

The layout of this document will include a general introduction, background, and theory which relates to all three research questions/objectives. Each chapter beyond this will focus on a specific element of the project, including any additional background, experimental setup, results and discussion, as well as closing remarks for the section. Finally, there will be an all-inclusive conclusion and recommendation for future work, which will summarize lessons learned from each section, respectively.

CHAPTER II

REVIEW OF LITERATURE, BACKGROUND, THEORY, AND PRELIMINARY STUDIES

2.1 Review of Literature

Turboelectric and other hybrid gas-electric propulsion and power systems are not only being researched in the UAS market, but the increased need for longer range and endurance has driven customers in both the commercial and defense market to explore hybrid manned systems. Additional concerns of carbon footprint have also helped push development of electric or hybrid-electric propulsion and power. Brelje and Martins present a summary of proposed concepts including electric, hybrid, and turboelectric architectures [7]. This document details the rapid spike in electrified propulsion efforts for commercial and governmental users. Thipphavong et al. discuss the implications of urban air mobility in metropolitan areas on electrical infrastructure for electrically-driven distributed propulsion aircraft [8]. Turboelectric power generation has potential to reduce the electrical footprint required, potentially making urban air mobility attainable in the near term. Johnson et al. introduce a design study which presents several different concepts for urban air mobility, one of which includes a 15 passenger tilt-wing turboelectric vehicle. [9] This proposal shows that interest in turboelectric propulsion is expanding from large scale commercial transport to smaller scale urban air mobility type platforms. It is not certain if a scaling relation between turboelectric power systems for manned aircraft and unmanned aircraft exists, however this study will enable future design studies to determine these relationships. Large scale aircraft are also exploring the use of turboelectric propulsion and power as a means of reducing carbon footprint and fuel consumption.

The concept of turboelectric propulsion and power was originally developed for analysis and potential use in manned aircraft. Felder et al. discuss the use of distributed turboelectric propulsion to increase range and endurance for passenger aircraft [10], but the megawatt scale of these platforms necessitates technologies such as superconducting motors, generators, and cryogenic coolers. Many sUAS platforms operate on much lower power scales (<15kW) with lower heat transfer rates, allowing for simple convective cooling approaches and making turboelectric propulsion a viable method of power generation at the small scale. Welstead, and Felder discussed the benefit of turboelectric operation in manned aircraft like the Single-aisle Turboelectric Aircraft with an Aft Boundary Layer propulsor (STARC-ABL) citing a calculated reduction in fuel burn by up to 12% over the conventional configuration; however they indicate this technology would not enter into service until 2035 due to gaps in technology [11] as discussed by Felder [10]. Unlike manned aircraft, turboelectric propulsion and power for sUAS can be designed and tested with current level of technology equipment and is very attainable in the near term. Jansen et. al discusses the use of turboelectric, partially-turboelectric, and hybrid systems for use in commercial air travel [12]. Figure 3 shows the key differences between turboelectric and partially-turboelectric systems. The turboelectric system which is the focus of this paper, can also serve as sub-scale research for these larger manned systems, as some information is expected to be applicable at the large scale. The system discussed in this study will operate in a purely turboelectric configuration and is on the order of several kilowatts; the systems discussed by Jansen et al. are on the order of megawatts and are for manned applications.

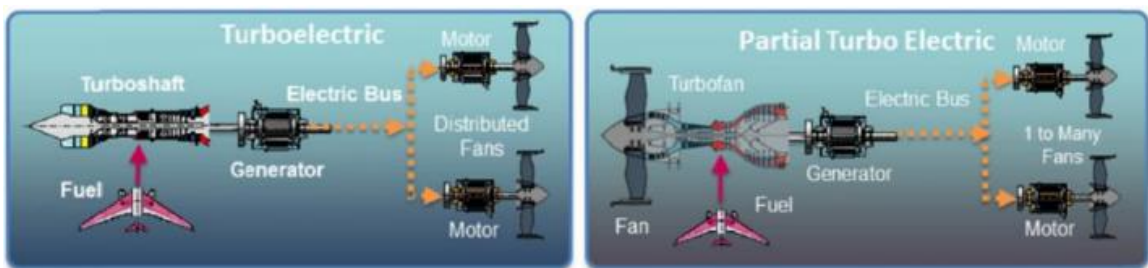


Figure 3. Figure depicting differences in partial and pure turboelectric systems [12]

Jansen et al. [13] discuss several turboelectric concept aircraft and indicate that even with advanced level of technology components for the turboelectric system, overall system heat losses could approach 320kW for the STARC-ABL even with an electrical efficiency on the order of 89.1 percent. This reinforces the current gaps in technology related to integration and thermal management of a turboelectric system at the larger scale, but also shows that this technology is well within reach as the scale decreases. Vratny and Hornung discussed the use of hybrid-electric flight on an Airbus A320 scale vehicle and showed an increase in MTOW by nearly 34% and propulsion system by nearly 56% with the hybridization of the vehicle [14]. Their study indicated an 8.5% reduction in in-flight fuel consumption relative the reference aircraft at the expense of this added weight and a decrease in carbon footprint. Similar to this study, the turboelectric system described in this document is expected to have similar effects on fuel weight and fuel consumption, even at the small unmanned scale. One of the applications of turboelectric power generation is for use in distributed propulsion. Distributed propulsion is enabled by electrification of the propulsion system, allowing power to be distributed electrically rather than mechanically. Kirner et al. present a conceptual design tool used to model both conventional tube-and-wing aircraft and blended body aircraft with the effects of distributed propulsion on fuel economy. [15-16] Their model estimates a fuel efficiency gain of 4.1% on a conventional aircraft and 5.3% on a blended-wing-body aircraft by having distributed propulsors to increase propulsive efficiency. Though this model shows some of the system level trends, it is not validated by experimental data. Liu et al [17] discussed a thermal cycle analysis done to model turboelectric propulsion and power; however, this model did not include an experimental component for validation. The current study will not only develop several models of the system, but each model will be analyzed and validated against experimental data. The models developed in this study address both steady and unsteady electromechanical behavior and will all be validated by experimental data over a range of operating conditions. These results will serve as a stepping stone to developing additional design tools and analysis methods for this rapidly developing technology. While

hybrid-electric systems for manned aircraft are still under long term development, the sUAS market is rapidly evolving to include hybrid power systems as means of increased range and endurance.

There are multiple UAS hybrid-electric systems that have been developed, analyzed, and discussed for both multicopter and fixed-wing applications to increase endurance [18-22]. All of these applications utilize a piston-cylinder internal combustion engine. Piston-based systems present an array of problems, motivating this current study of a turbine-based hybrid electric system. Though generally more fuel efficient, problems such as cylinder wall cooling, vibration, thermal management, and shaft speed limits the potential of piston-based hybrid systems. An example piston engine is shown in Fig. 4.



Figure 4. Desert Aircraft 100CC piston engine [23]

Turbine-based hybrid systems are still in development and offer a higher power-to-weight ratio compared to a piston engine, thus turboelectric systems can have a lower deadweight mass fraction than a comparable piston hybrid system. The advantage generally increases as the scale of the power system increases. This realization sparks the interest of not only commercial but government agencies.

Wilson announced a program to develop fuel-to-electricity systems that group air-breathing propulsion systems with power generation systems used to power electric propulsion systems, showing government and industry interest in increased range and endurance [24].

Rotramel further explored this concept looking at clutch-start parallel configuration on sUAS, in which a combustion engine and electric motor/generator power a common shaft and observed higher complexity and system weight than series hybrid configurations [25]. Purely turboelectric operation follows a more similar architecture to the series hybrid-electric configuration, as clutch start parallel is more applicable in partially turboelectric configurations; a discussion of series and parallel hybrid configurations can be found in the background section of this document.

McKinney et al. discussed other issues encountered when employing a piston-based hybrid system, such as vibration, overall propulsion system weight, and complexity [26]. These challenges are easier to overcome when employing a turbine engine in lieu of a piston engine simply due to the physics at play; this topic is discussed in greater detail in the background section of this document. McKinney's applications looked specifically at the multicopter UAS [27], which is an ideal application of turboelectric systems as both power and energy density are highly sought after.

2.2 Background and Theory

A discussion of relevant background and theory is given in the following section. Theory discussed includes a comparison of piston and turbine engines, energy density vs. power density, hybrid architectures, turbine theory, and the proposed concept of operation to best leverage the benefits of turboelectric propulsion and power.

2.2.1 *Piston vs. Turbine*

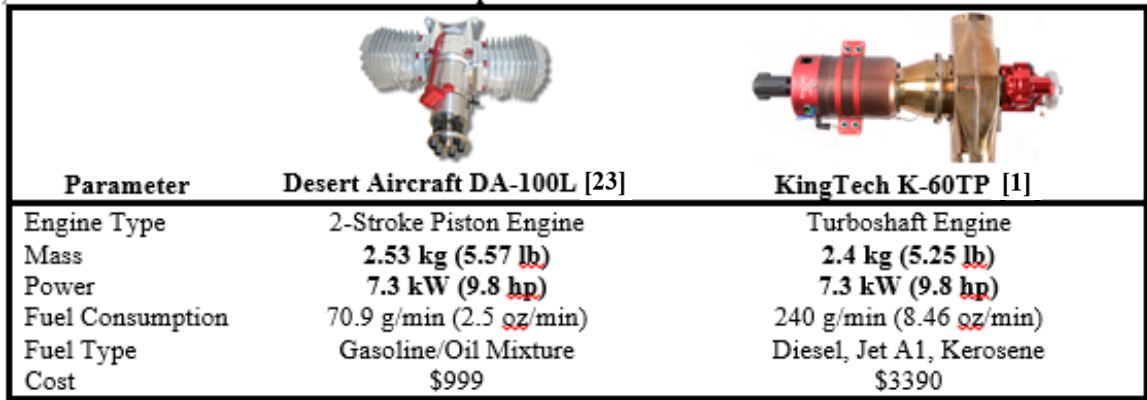
Though generally more fuel efficient than a small turbine engine, small piston-based hybrid-electric systems face an array of issues, including but not limited to vibration, cylinder wall cooling, added system weight, and in certain applications fuel type. McKinney [26] quantified the vibration created by a piston engine when integrated onto a multicopter, however in this study our focus is on the turbine engine. Vibrations, however, for piston engines are inevitable by the nature of the cycle. The Otto cycle is very similar to the Brayton cycle in terms

of processes, however the execution of these processes are different. While the Otto cycle uses a piston-cylinder arrangement for compression and expansion, the Brayton cycle uses high speed rotation and airfoil geometry for compression and expansion. Because of this, flow travels axially through the turbine which imposes very little vibration assuming that the rotating parts are well balanced. On the other hand, the piston engine compression and expansion are achieved by a translating piston-cylinder arrangement, which is the source of much of the vibration. Vibration can be reduced by placing the cylinder heads in a fashion where the momentum of each piston is opposite each other, however this does not fully solve the problem. Turbine engines generally operate at higher speeds than piston engines, thus the effect of vibration would likely be at much higher fundamental frequencies than that of the piston engine; high frequency vibrations should have little effect on the airframe as long as they are low in amplitude. Gyroscopic coupling could prove to be prevalent as well with either system, as rotating machinery is present.

Piston-based hybrid electric systems require cooling of the cylinder heads; this is due to the nature of the cycle. On the large scale, gas turbine engines require cooling passages to keep the turbine from melting during the expansion process, however even at the large scale the weight penalty is negligible, potentially even a none as the cooling passages in turbine blades requires material to be removed. At the small scale, or for turbine inlet temperatures less than 1500 degrees Fahrenheit, no additional cooling is required for the turbine in the general case. Large scale piston engines are generally water cooled, air-cooled, or some combination of the two; however, small scale for RC aircraft piston engines are generally air-cooled. For many applications, this is a satisfactory way of cooling the engine, however in hybrid system applications involving multicopter aircraft this method is not generally sufficient alone. Due to integration challenges associated with installing piston engines on multicopter platforms, the location in which the engine is placed generally does not permit enough airflow over the cylinder heads to adequately cool them, even though the cylinder heads have cooling fins. The addition of auxiliary cooling systems means the addition of weight, auxiliary power, and overall system

complexity. For fixed wing applications in series-hybrid configuration, piston cylinders and heads must either protrude from the airframe or face the same cooling requirements set forth in the multirotor example. Protruding heads is effectively like adding a drag device.

Figure 5 below shows the manufacturer specifications for a Desert Aircraft 100cc piston engine, as well as a KingTech K60TP turboprop engine. Though the piston engine is more fuel efficient as per the manufacturer specifications, the turbine engine system is lighter in total weight and produces the same power as quoted by the manufacturer. The weight estimate on the turbine engine also includes a controllable starter, which is not included on the piston engine. To include a starter on the piston engine, the generator must be used as a starter; in order to do this a radio-controlled speed controlled device circuit must be developed, which allows current to flow bi-directionally into the generator to start the engine. This addition of electronics and enclosures adds weight and complexity to the overall system. When cooling requirements are considered, the power-to-weight advantage of the turbine based system increases further beyond the piston-based system. With a higher power-to-weight ratio, the turboelectric system will have a lower deadweight and be able to carry more fuel for a specified maximum takeoff weight (MTOW). With weight decreasing over the duration of the flight, less power is required which allows the turbine throttle to be reduced over the duration of the flight. It is not expected that the turbine engine will surpass the piston engine in terms of specific fuel consumption, but these advantages could potentially allow the system to see a comparable endurance with that of the piston-based hybrid system. Furthermore, this power-to-weight advantage of the turbine engine over the piston engine is amplified as the scale of the engine increases, making this option viable for use in large scale applications, such as the NASA STARC-ABL concept [11] or the NASA urban air transport concept [8].



Parameter	Desert Aircraft DA-100L [23]	KingTech K-60TP [1]
Engine Type	2-Stroke Piston Engine	Turboshaft Engine
Mass	2.53 kg (5.57 lb)	2.4 kg (5.25 lb)
Power	7.3 kW (9.8 hp)	7.3 kW (9.8 hp)
Fuel Consumption	70.9 g/min (2.5 oz/min)	240 g/min (8.46 oz/min)
Fuel Type	Gasoline/Oil Mixture	Diesel, Jet A1, Kerosene
Cost	\$999	\$3390

Figure 5. Comparison of piston engine and gas turbine engine manufacturer specifications

Though generally not a concern to commercial and industrial users, the ability to run on various types of fuel, such as diesel or Jet A1 (JetA) is desired by military users. Select subscale piston-based systems have the ability to run on heavy-fuel or diesel, however this is a standard feature of many subscale gas turbine systems, including the KingTech and JetCat lineup. This is desirable for reduction of on hand resources, such as additional types of fuel and fuel storage; many military assets operate on diesel as opposed to gasoline.

2.2.2 Energy Density vs. Power Density

Hydrocarbon fuels are on average around 75 times more energy dense than batteries, however batteries exhibit a higher power density. Energy density and power density are both important propulsion system design parameters, however they are important for different reasons. Power density, by definition is the amount of power per unit mass, while energy density is the amount of energy per unit mass. It is important to note that the mass is that of the entire propulsion system. For example, the mass of the electrical load must be included in the energy and power density calculation for batteries; similarly, the mass of the engine, generator, and rectifier and electrical load must be included for the hybrid system energy and power densities. A hybrid system leverages both the high energy density of hydrocarbon fuels and the high power density of electric propulsion systems. A propulsion system with a high power density is desired for mission legs such as takeoff, hover, and climb; these legs may require the highest amount of

power, or instantaneous energy, but not necessarily the highest amount of total energy as they are generally for short periods of time. Energy density on the other hand is desired for lower-power portions of the mission such as loiter, cruise, and powering external accessories. This portion of the mission lasts the longest, thus total endurance can increase substantially by increasing the energy density of the propulsion system. The ability to leverage both energy and power density makes hybrid systems advantageous in the pursuit of increased range and endurance without compromising on power. The power and energy densities of several common types of propulsion and power systems are compared in Fig. 6.

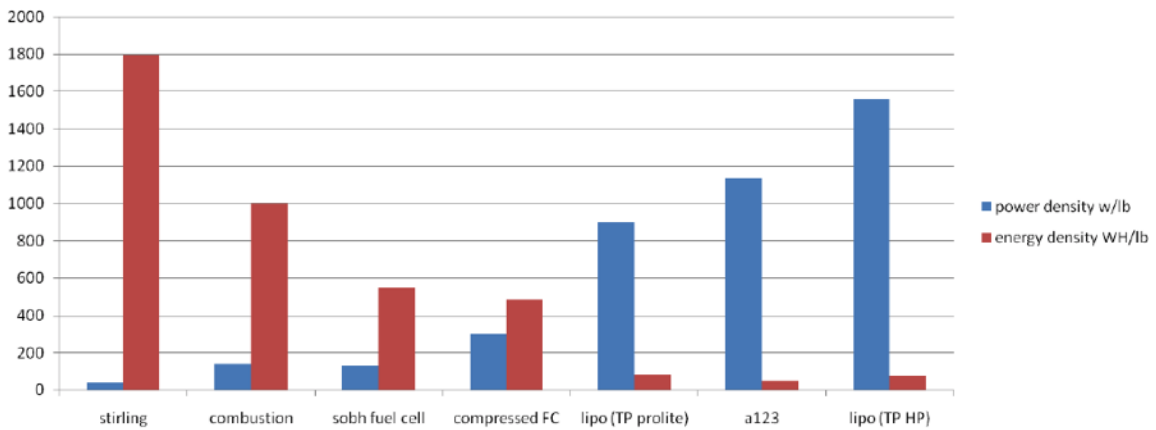


Figure 6: Power density vs. energy density of several common propulsion and power systems

[28]

2.2.3 Hybrid Architecture

There are two power architectures commonly used when discussing hybrid-electric power systems: series hybrid and clutch-start parallel. This is outlined by Hung and Gonzalez [21]. A series hybrid system refers to a system in which the drive motor is used solely for driving the generator in electrical power production; no shaft work is put into the propulsors but rather transmitted electrically to some number of propulsors. A clutch start parallel hybrid configuration differs from this in several regards, one of these being the distribution of mechanical power. In a clutch-start parallel hybrid system, the drive motor shares a shaft with a motor-generator. Some

work from the drive motor will go to the propulsors, while some can go into driving the generator. The motor-generator in this type of system is generally used for powering onboard electronics or recharging batteries, however if a clutch is properly designed for the system the drive motor shaft can be released with and the motor-generator can be used to power the propulsors. In both power architectures involving piston-based hybrid systems, the motor-generator is also used as a starter. Examples of both power architectures can be shown in Fig. 7.

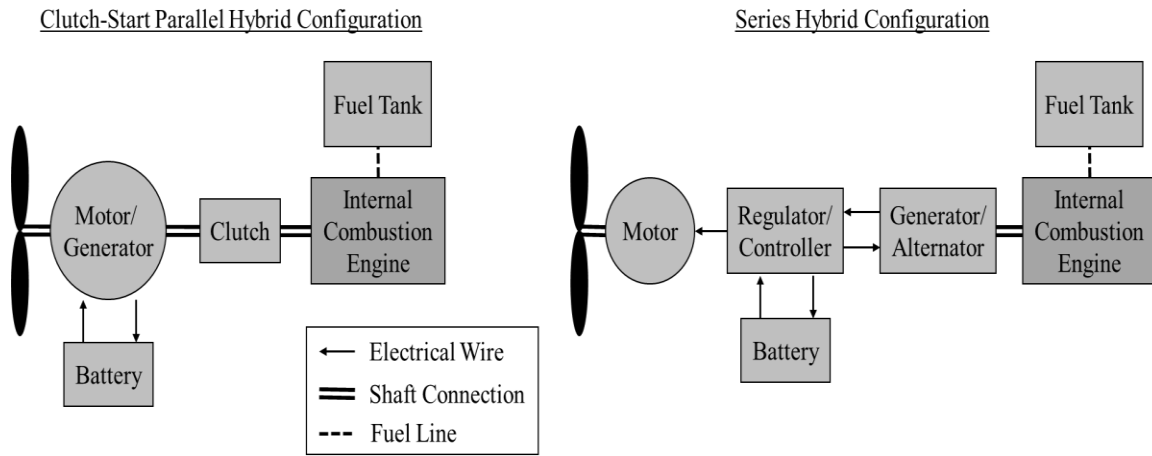


Figure 7. Schematic of series vs. parallel hybrid configurations [21]

As various research on turboelectric systems is evolving, there is agreement among much of the research community that turboelectric propulsion is in a category of its own, favoring the series hybrid configuration with much of its architecture. Additional nomenclature is being developed as the popularity of this system increases.

2.2.4 Turbine Theory

Overall turboelectric efficiency takes into account thermal, propulsive, and electrical efficiencies, as shown in Eqs. 1-3. Rouser et al. [29] explained that a multirotor, distributed propulsion and power system benefits in overall system efficiency due to the distribution of increased propulsive fluid energy over a large propulsive fluid mass. Mattingly and Boyer [30] presented the thermodynamic equations for gas turbine engines as shown below. Thermal efficiency of a small engine is constrained by low overall pressure ratio (OPR) as shown in Eq. 1.

Equation 2 shows that propulsive efficiency increases as the propulsive fluid exhaust velocity (V_9) decreases and approaches 100% as the exhaust velocity approaches the flight speed (V_0). It is possible to improve overall efficiency of a small turboelectric system by increasing propulsive efficiency, even with the penalty of electrical efficiency. Therefore, it is critical to know electrical efficiency in order to predict overall efficiency.

$$\eta_{th} = 1 - \left(\frac{1}{OPR}\right)^{\frac{\gamma-1}{\gamma}} \quad (1)$$

$$\eta_{prop} = \frac{2}{\frac{V_9}{V_0} + 1} \quad (2)$$

$$\eta_o = \eta_{th}\eta_{prop}\eta_{elec} \quad (3)$$

Mattingly and Boyer also present relevant thermodynamic equations for a dual-spool turboshaft engine, given by Eqs. 4-6, which are based on several assumptions: steady, 1-D, adiabatic flow of a calorically perfect gas. The burner efficiency is given in the equation, and is manifested on the T-s diagram as a lower total temperature rise between station numbers 3 and 4. Equation 4 relates the power into the compressor (station numbers 2 to 3) from the high pressure turbine (station numbers 4 to 4.5), accounting for mechanical efficiency. Equation 5 relates power supplied by the power turbine (station numbers 4.5 to 5) to engine shaft power output, also accounting for mechanical efficiency. Equation 6 relates combustor exit total temperature (T_{T4}) to fuel flow rate and fuel heating value (h_{PR}), including a term for burner efficiency.

$$\dot{m}_c c_{p_c} (T_{T3} - T_{T2}) = (\dot{m}_c + \dot{m}_f) c_{p_t} (T_{T4} - T_{T4.5}) \eta_{mech} \quad (4)$$

$$\eta_{mech} (\dot{m}_c + \dot{m}_f) c_{p_t} (T_{T4.5} - T_{T5}) = \tau_s \omega_s \quad (5)$$

$$(\dot{m}_c + \dot{m}_f) c_{p_t} T_{T4} - \dot{m}_c c_{p_c} T_{T3} = \eta_b \dot{m}_f h_{PR} \quad (6)$$

At a stable engine operating condition, Eqns. 4-6 are satisfied, based on a throttle input to regulate fuel flow rate and a shaft power output that meets the electrical load demanded. For a turboelectric system, the electrical load dictates the shaft power required and consequently the required fuel flow rate. Backpressure can result from an electrical load which exceeds the shaft

power available, causing significant operability problems, especially when the turbine is unchoked. This result can be illustrated on the ideal Brayton Cycle temperature-entropy (T-s) diagram shown in Fig. 8 whenever the total temperature difference between stations numbers 4.5 and 9 is insufficient for the shaft power required.

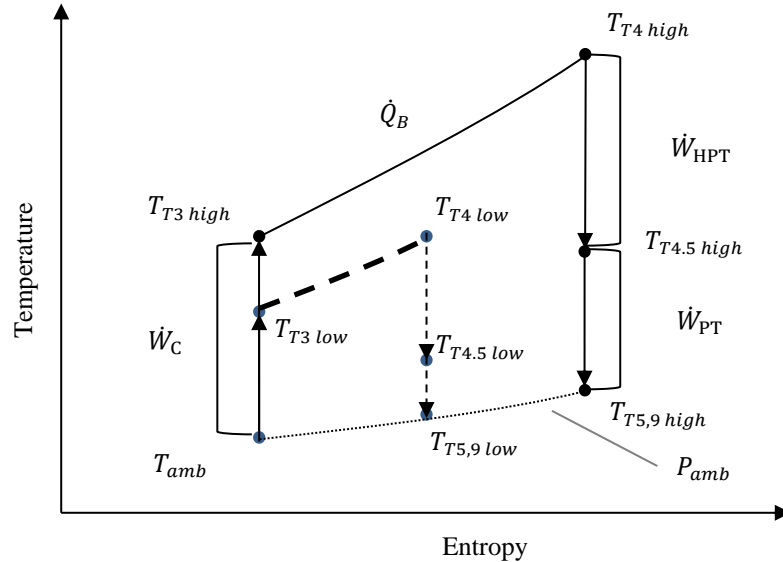


Figure 8. Temperature entropy diagram of Brayton cycle

For good turboelectric engine operability, the electrical power demand cannot exceed the shaft power available from the power turbine (PT). The total temperature at station five is assumed to be equal to the total temperature at station nine because the nozzle is assumed to be adiabatic. The total temperature at station 4.5 is measured by the engine control unit (ECU). Total temperatures at stations (3-9) will increase as the throttle is advanced and fuel flow rate increases. Pressure lines diverge as more heat (i.e. fuel) is added, thus more PT power is available at higher throttle settings even though the exhaust fluid temperature is much higher. The T-s diagram shows the increased temperature difference between station numbers 4.5 and 9 when the throttle is advanced. Fuel mass flow rate is the primary turbine engine control input; thus, the difference in total temperature between station three and four is an indirectly controlled parameter.

2.2.5 Concept of Operation

A proposed concept of operation can be shown below in accordance with the objectives of the study. Both fixed-wing and rotary-wing operation can be shown in Fig. 9, with the overview of the flight plan shown below. Note the major advantage of refueling between missions as opposed to the need to recharge or replace batteries. This seemingly simple modification the flight profile can drastically reduce the amount of downtime the vehicle is subject to under normal operation. The fixed-wing variant will be used in sparsely populated areas where a long range or large geographical footprint is needed, such as a transmission line shown on the right in Fig. 9. On the other hand, the rotary-wing vehicle will be used in areas with structures or where VTOL and hover capabilities are desired; an example of this is the gathering and distribution center shown on the left in Fig. 9.



Figure 9: Rendering of proposed concept of operation for rotary (left) and fixed (right) wing turboelectric vehicles

The proposed concept of operation (ConOP) for both the rotary-wing and fixed-wing vehicle shown above can be described by the following flight plan.

- 0-1: Autonomous VTOL/CTOL
- 1-2: Climb to altitude and hold
- 2-3: Cruise and inspection
- 3-4: Descent, loiter/hover, detect and mark
- 4-5: Ascent, finish cruise and inspection

5-6: Return to TO sight

6-7: Autonomous landing

7-8: Refuel and repeat (if necessary)

The flight plan described above can best be illustrated the schematic, shown in Fig. 10.

There may be multiple leaks or multiple refuels required depending on the size and condition of the pipeline undergoing inspection. If the fixed-wing variant has VTOL capabilities, it would undergo the same flight plan as the rotary-wing vehicle, with the only differences being those described above regarding the type of pipeline undergoing inspection by each vehicle.

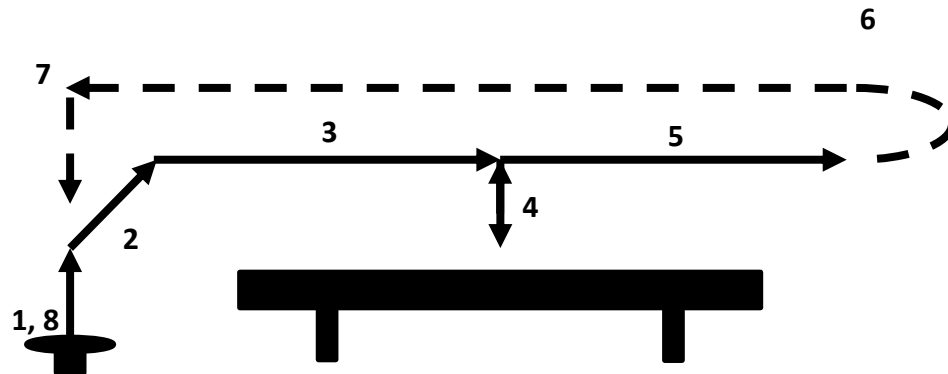


Figure 10: Schematic of proposed concepts of operation

2.3 Preliminary Studies

Several preliminary studies were performed as part of the conceptualizing and realizing a design for turboelectric propulsion and power. These studies stemmed from a few key questions, which included the question of theoretical range and endurance on a multirotor platform. This is the area in which hybrid systems pose the greatest margin for gains, necessitating a theoretical mission analysis comparing piston-hybrid, turboelectric, and all-electric configurations. The second study done was a baseline endurance test on a multirotor aircraft, as multirotor show the greatest potential for gains in endurance with a hybrid propulsion system. The purpose of this test was to determine the average endurance of a stock multirotor aircraft with zero payload for means of comparison in baseline testing. A third study was done, which focused on stability and control

considerations for hybrid systems. Specifically for the multirotor application, gyroscopic coupling can emerge when maneuvering thus a simple stability and control analysis was performed to see the affected axes. The stability and control analysis is given in the Appendix, and the remaining studies are discussed in the following sections.

2.3.1 Mission Analysis

A mission analysis was done to compare the various options available for powering a multirotor platform like that described in the concept of operation. This analysis is effectively a trade study of various propulsion systems including stock batteries, turboelectric, and series piston-hybrid. The platform used for the analysis is the DJI Agras MG-1, which has a maximum takeoff weight of 55 pounds. This was selected because the inherent weight of the hybrid system necessitates a large platform to produce improved range and endurance over batteries. A few assumptions were made when performing the mission analysis. One of these key assumptions was that the weight of the mounting hardware would be approximately the same for each type of propulsion system. The additional batteries or hybrid power systems both require additional hardware, which was assumed to be 2 pounds. The next key assumption is the conversion efficiency for the hybrid systems is approximately constant for the entire range of shaft power output, but is not the same between different power systems. Conversion efficiency, η_{conv} is defined as the thermal efficiency, η_{th} , of the combustion engines times the electrical efficiency, η_{elec} , as shown in Eq. 7. Making this assumption simplifies the comparison between energy density of fuel and batteries; this is the total energy available, E_{avail} , that can be supplied to the motors after the conversion has taken place, as shown in Eq. 8 where m_{fuel} is the fuel mass and h_{PR} is the fuel heating value. For the piston-hybrid case only, one pound of cooling considerations was added to the weight estimate. For the power management unit (PMU), or the device which interfaces the hybrid power with the battery backup power, it was assumed that the turbine PMU would weigh approximately 70% of the piston PMU. This is because the turbine has

a built-in starter, while the piston must be started by supplying power to the generator, effectively utilizing it as a starter. This additional board space on the PMU paired with a custom enclosure accounts for approximately 30% of the weight of the entire PMU. Table 1 presents takeoff and landing weights for each configuration, with the mass of fuel or batteries being determined by the difference in MTOW (Maximum Takeoff Weight) and deadweight not including the energy source.

$$\eta_{conv} = \eta_{th}\eta_{elec} \quad (7)$$

$$E_{avail} = m_{fuel}h_{PR}\eta_{conv} \quad (8)$$

The mission profile is very simple for this application, as only hover endurance is being considered. Due to the low amount of maneuvering, it can be assumed that the power is being used primarily for hovering and not for maneuvering. As seen in Table 1, mission analysis shows an endurance time of 19.5 minutes for the batteries, 39.6 minutes for the turbine hybrid system, and 85.6 minutes for the piston hybrid system when a 3-pound camera payload was included. Because the engines had not been fully characterized in the turboelectric system, the mission analysis used energy conversion methods to calculate the endurance of the systems, as outlined above. This result shows the turbine and piston hybrid systems are reasonable ventures for increasing the range and endurance of the Agras MG-1 or similar platforms. Turboelectric systems were selected for the project because they produce significantly less vibration, require less cooling, and exhibit a much greater high-end torque and higher power-to-weight ratio than piston engines, allowing them to be easily scaled up for large scale, high voltage applications. On the small scale, they allow for more sensitive instrumentation to remain stable throughout the flight without additional damping devices and require no auxiliary power to cooling devices or additional circuitry for startup. The actual implementation for the experimental purposes was performed on the smaller X-Fold dodecacopter due to budget and DoD manufacturer constraints. A completed design provides a proof of concept and configuration for application on larger systems like the MG-1.

Table 1. Results of mission analysis performed comparing piston-hybrid, turboelectric, and all-electric configurations.

	<i>Takeoff</i>	<i>Landing</i>	<i>Fuel/Battery</i>	<i>Endurance</i>
	<i>Weight (lbf)</i>	<i>Weight (lbf)</i>	<i>Weight (lbf)</i>	<i>(min)</i>
<i>Stock (one 12S, 16000mAh batt.)</i>	31.2	31.2	8.8	19.5
<i>Turboelectric</i>	54	42.2	11.8	39.6
<i>Piston-Hybrid</i>	54	45.5	8.5	85.6

2.3.2 Baseline Endurance Testing

To begin, a series of rotary-wing platforms were selected for review and judged based on a set of parameters set forth by the customer and the researchers; the xFold Travel 12 DodecaCopter was selected. The vehicle is powered by two 6 cell Lithium-Polymer (LiPo) battery pack, which produces a nominal 22.2 Volts ran in parallel. The vehicle is equipped with 6 pairs of T-Motor MN4014-11 330KV motors and CF 15x5R contra rotating propellers (CRPs). The baseline test to be performed was to validate hover endurance and power draw of the system varying several common environmental parameters, such as wind, temperature, and pressure. The test was run in the stock configuration and flown to the manufacturer’s specifications for takeoff, landing, and battery health. The results of the baseline endurance test can be shown in Table 2 with the associated confidence interval of the sample. Confidence was calculated utilizing a t-distribution with 4 degrees of freedom at 95 percent. The power and total energy to the vehicle was monitored as well and can be shown in Table 2. The total energy use was calculated in accordance with Ohm’s Law, as shown in Eq. 9.

$$E = \int_0^t i(t)V(t)dt \approx V_{avg} \int_0^t i(t)dt \quad (9)$$

For small, consistent changes in voltage the average voltage can be used in place of the integral without introducing large errors into the calculation. By measuring the total capacity

drawn from the battery, the integral of current with respect to time is known, and thus the product with average voltage yields the total energy use in watt-hours, or units of energy. This was done for each case; the average instantaneous power can then be tabulated by dividing the total energy used by the time of flight for each run. This can be shown in Eq. 10.

$$P = \frac{d}{dt} E(t) \approx \frac{E_{total}}{\Delta t} \quad (10)$$

Table 2. Results of endurance testing, xFold Travel 12, stock configuration

	<i>Average</i>	<i>St. Dev</i>	<i>DF</i>	<i>95% Conf.</i> (+/-)	<i>Percent</i>
<i>Endurance (min)</i>	17.57	0.66	4	1.03	5.9%
<i>Total Energy (W-hr)</i>	500.97	23.44	4	36.64	7.3%
<i>Power (W)</i>	1710.86	62.79	4	98.16	5.7%

Endurance is the parameter of interest, this is the baseline for comparison with the turboelectric hybrid. In comparison to the mission analysis, the baseline endurance testing showed a similar trend with respect to the baseline endurance testing, which is within the margin of uncertainty given various atmospheric conditions, battery health, and wind gusting compared to the ideal analysis done in the mission analysis.

CHAPTER III

POWER SYSTEM DESIGN, MODELING, AND VALIDATION

Beginning with theoretical and empirical data, the turboelectric propulsion and power system described will be designed, fabricated, and tested. This chapter will outline not only selection of components and their significance, but also present development and validation of an analytical model via experimental data. Results of this chapter will include electrical efficiency and voltage throughout the duration of the operating regime. The electrical model developed and validated in this chapter will serve as a stepping stone to development of an active throttle controller to regulate turbine throttle throughout the duration of operation. Results of this section will be used in refinement of the system moving forward.

3.1 Component Selection

The system designed in this study will be built around the turboshaft engine. This is due to several factors, the largest driver however is the availability of small scale turboshaft engines. There are a few options on the market, including the KingTech K60TP and the Jetcat SPT5, however due to budget restrictions and availability of the Kingtech turboprop, it was selected for use in the preliminary design. Benchmarking was done prior to selection; the anticipated electrical efficiency expected was on the order of 60 to 70 percent. For a 5kW electrical system, which is common among UAS, the required input power would be on the order of 7.1 to 7.6kW mechanical power. The Kingtech model which meets these requirements is the K60TP G2 turboprop engine. Kingtech quotes a peak mechanical power of 7.3kW at shaft speeds on the order of 6,500 to 7,500 RPM, respectively. The turbine is a dual-spool, indicating that the high

pressure turbine (HPT) and the low pressure turbine (LPT) are not mechanically coupled. This allows the output shaft to rotate at a different shaft speed than the core turbine. The manufacturer specifications are given in Fig. 5, as well as a photo of the turbine and the manufacturer power curve shown in Fig. 11.

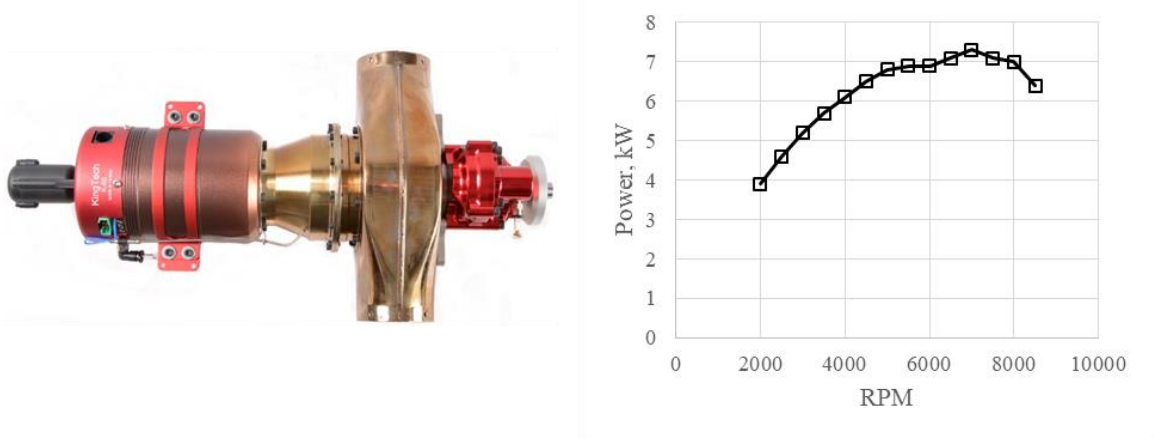


Figure 11. Kingtech K60TP [1] (left) and manufacturer power curve (right)

The second component to be selected was the electric generator. With increased interest in hybrid UAS, there has been an increased number of suppliers who manufacture and design custom hybrid generators, however due to cost and time restrictions a brushless DC (BLDC) motor was selected for use as the generator. There are several important parameters to be mindful of when selecting a generator, such as the speed constant, or KV rating, and the continuous current. These parameters are each important in their own way. The speed constant rating, or the amount of voltage per rotational speed, is important for precisely that reason. If the speed constant rating is too low, there will be too much torque required from the mechanical input to obtain the current required by the load. Lenz Law [31-32] states that the force generated from a coil rotating in an armature is opposite of the direction of the rotation. This reaction torque is the load torque the turbine engine will experience under standard operation. Turbine engines generally do not perform well at low shaft speed, being more susceptible to instabilities and stall, as the single stage power turbine would be very highly loaded. If the speed constant rating is too

high, the turbine engine could not generate the voltage required for its useful range of shaft speed. To tabulate the best speed constant, the Eq. 11 should be used, where V_L is the load voltage and shaft speed is the shaft speed at optimum peak power. The current required is governed by the electrical load which follows Ohm's Law, given in Eq. 12. The generator selected for this application is the Turnigy Rotomax 100CC; it has a peak power rating of 8kW at 51V and a speed constant of 167 RPM/VDC. The motor also has 24 poles, indicating that there will be 12 peaks to be single rotation.

$$K_v = \frac{V_L}{\omega_{t_{peak}}} \quad (11)$$

$$i_L = \frac{P_L}{V_L} \quad (12)$$

The final component to be selected is the rectifier. There are many types of rectifiers, however the only type being considered for this application are three-phase rectifiers. Three phase refers a signal in which there are three voltage waveforms, which are 120 degrees out of phase and period functions. Though efficiency will differ slightly between specific rectifiers, there are two types which can be used in this application: a full wave and half wave rectifier. A full wave rectifier was selected as the output signal has less ripple. This ripple could require signal conditioning, especially if high frequencies are play from high-pole count generators. It is important to ensure that the rectifier selected is able to handle both the voltage and current specified by the load, as diodes can break down with too much reverse voltage and are sensitive to heat, or current losses due to the voltage drop.

3.2 Electromechanical System Model

Several losses must be considered in order to accurately model the system. There are three major sources of losses: Ohmic losses inside the generator, friction losses on the rotating machinery, and semiconductor losses. Each of these loss factors will play a part in the overall system electrical efficiency. The model developed in this paper follows the model developed by

Moody et al. [33-34] published in the ASME Journal of Engineering for Gas Turbines and Power and within the AIAA.

3.2.1 Rectifier Model

The type of rectifier used for the system is a three-phase full wave rectifier bridge; the schematic of the circuit can be seen in Fig. 12. The fundamental three-phase full-wave rectifier voltage equation be shown in Eq. 13, where V_{out} is rectified voltage out, $V_{p,LL}$ is the peak line to line source voltage, and ΔV_D is the voltage drop across the diodes. The type of rectifier is a key parameter, as the rectifier type governs the magnitude of the average output voltage and the amount of ripple. The quoted value for maximum voltage drop as per the manufacturer is 1.63V. The load will be characterized as an equivalent impedance as a function of pilot input; the ESC consists of only diodes and IGBTs, which are conductive elements only. Modeling as a purely resistive load allows the phase shift ϕ between voltage and current to be assumed 0 degrees.

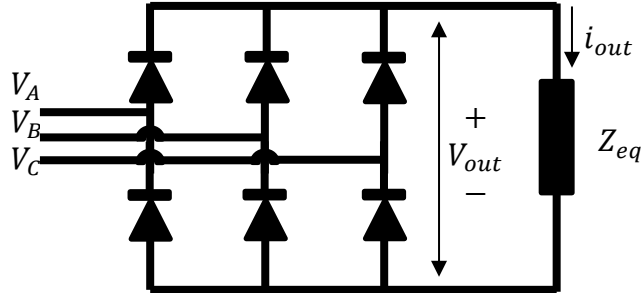


Figure 12. Equivalent circuit model of three-phase full wave rectifier

$$V_{out} = (V_{p,LL} - \Delta V_D) \quad (13)$$

The current supplied by the generator is a function of the load. It is also important to note that only the diode with the highest voltage conducts current at any point in time, while the diode with the lowest voltage allows the current a return path. Current across the load follows voltage as suggested by Ohm's Law in Eq. 14. The output voltage and current waveforms are shown in Figs. 13-14 below. The current waveform has positive and negative currents of equal magnitude, where the negative current is the return path for the positive current; this satisfies Kirchoff's Law,

and reinforces that only one path is available for current to flow at any 1 point in time. These equations will be combined with the generator inertial and electrical model for use in testing. It is important to note that both the current and voltage waveforms are two-pi periodic with respect to $\omega_e t$. The average DC voltage and current is obtained by integration, and equates to the form shown in Eq. 15.

$$i_{out} = V_{out}/Z_{eq} \quad (14)$$

$$P_{DC,avg} = \left(\frac{3}{\pi}\right)^2 P_{out} \quad (15)$$

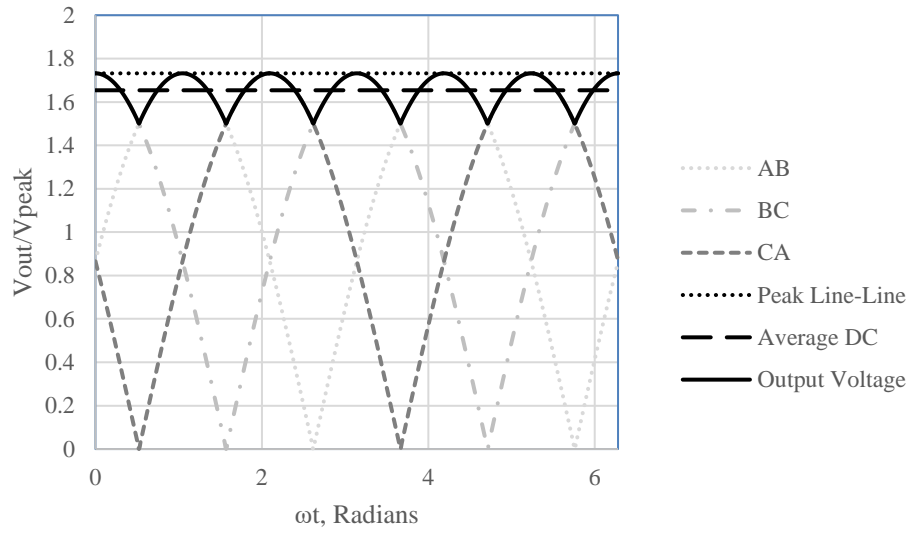


Figure 13. Voltage waveform transformation across the rectifier

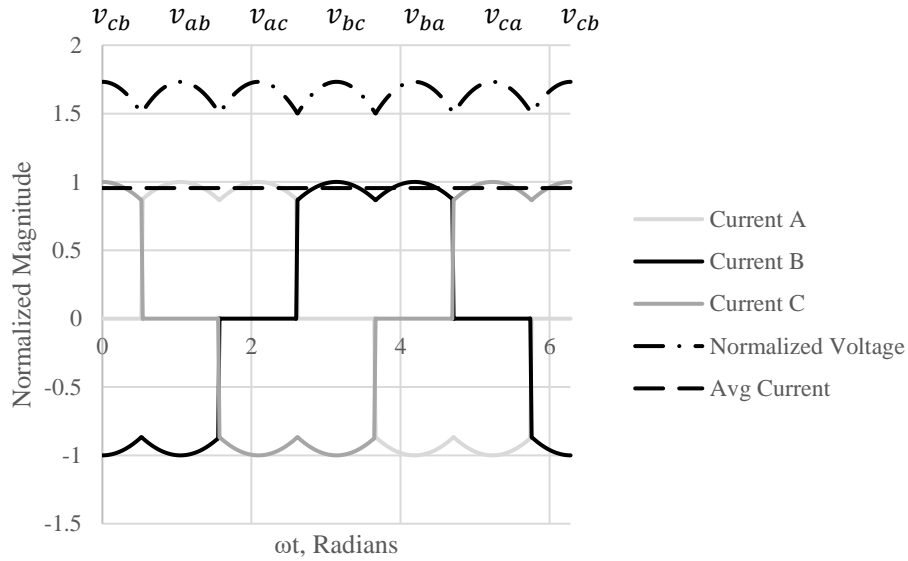


Figure 14. Current waveform exiting the rectifier

3.2.2 Generator Inertial Model

Equation 16 gives the dynamic equation of motion for the generator, where τ_T is the torque from the turbine engine, τ_L is the load torque, I is the generator mass moment of inertia, c is the friction coefficient, and ω_m is the mechanical speed of the generator and turbine. The free body diagram in Fig. 15 is used in reference to the dynamic equation of motion. Multiplying by mechanical speed, the LHS of the equation becomes the mechanical power delivered by the turbine, while the RHS transforms into the nonlinear ordinary differential equation shown in Eq. 17, where P_{gen} is the electrical power generated. The mechanical losses attributed to friction can be seen in Eq. 18, however with no prior information about the value of friction coefficient, it will be obtained experimentally. Electrical losses will be assessed in the next subsection.

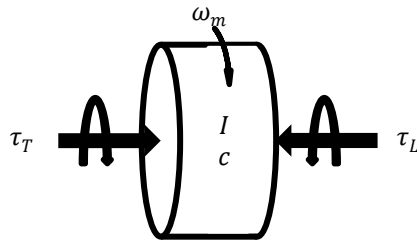


Figure 15. Free body diagram of the generator with applied torque

$$\tau_T = \tau_L + I\dot{\omega}_m + c\omega_m \quad (16)$$

$$P_T = P_{gen} + I\dot{\omega}_m\omega_m + c\omega_m^2 \quad (17)$$

$$P_{L,m} = c\omega_m^2 \quad (18)$$

3.2.3 Generator Electrical Model

Losses also occur within the electromechanical device or devices. The generator equivalent circuit shown in Fig. 16 will be used to model the generator electrical system dynamics. The configuration for this generator is known as a wye configuration, as opposed to a delta configuration. In this configuration, the central node is the common ground for each phase. Ohm's Law for the three phases is written in Eq. 19 in vector notation, where R is the phase resistance, L is the phase inductance (including mutual inductance), e_i is the phase back emf, i_i is the phase current, and V_i is the phase voltage out. Solving for voltage out, the equation takes the form shown in Eq. 20. It is important to note that for three phase generators mechanical speed and electrical speed are different, and vary proportionally by the number of pole pairs. This conversion is shown in Eq. 21.

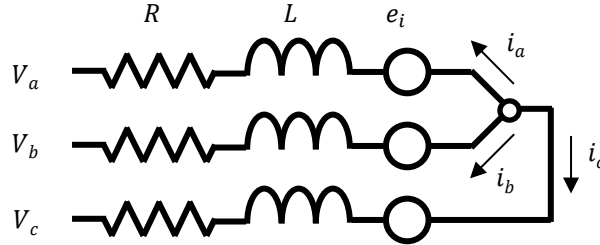


Figure 16. Equivalent circuit model for BLDC generator

$$\vec{e} - \vec{V}_{LN} = R\vec{i} + L\frac{d}{dt}\vec{i} \quad (19)$$

$$\vec{V}_{LN} = \vec{e} - \left(L\frac{d}{dt}\vec{i} + R\vec{i} \right) \quad (20)$$

$$\omega_e = \frac{p}{2}\omega_m \quad (21)$$

For voltage, phase A is the reference phase while phase B and C are shifted 120 degrees and 240 degrees from phase A, respectively. The phase of current relative to voltage is a function

of the electrical load, however because the signal is being rectified and the load is being modeled as purely resistive, the phase shift is 0 degrees. The expanded form of the vector equations can be shown in Eqs. 22-24, where phase current is the piecewise two-pi periodic waveform shown in Fig. 12, respectively. Phase A is shown in Eq. 23, while phases B and C are phase shifted by two-thirds pi and four-thirds pi, respectively. The use of the functions $u(t)$ and $\delta(t)$ are the Heaviside step function and the Dirac delta function, respectively.

$$\vec{e} = K_v \omega_e \begin{bmatrix} \sin(\omega_e t) \\ \sin(\omega_e t - \frac{2\pi}{3}) \\ \sin(\omega_e t - \frac{4\pi}{3}) \end{bmatrix} \quad (22)$$

$$\vec{i} = \begin{bmatrix} i_a \\ i_b \\ i_c \end{bmatrix}, \text{ where } i_a = i_{out} \left\{ \begin{array}{ll} 0 & 0 \leq \omega_e t < \pi/6 \\ u(\omega_e t - \pi/6) & \pi/6 \leq \omega_e t < \pi/2 \\ 1 & \pi/2 \leq \omega_e t < 5\pi/6 \\ 1 - u(\omega_e t - 5\pi/6) & 5\pi/6 \leq \omega_e t < 7\pi/6 \\ -u(\omega_e t - 7\pi/6) & 7\pi/6 \leq \omega_e t < 3\pi/2 \\ -1 & 3\pi/2 \leq \omega_e t < 11\pi/6 \\ u(\omega_e t - 11\pi/6) - 1 & 11\pi/6 \leq \omega_e t < 2\pi \end{array} \right\} \dots \quad (23)$$

$$\vec{V}_{LN} = V_{p,LN} \begin{bmatrix} \sin(\omega_e t) \\ \sin(\omega_e t - \frac{2\pi}{3}) \\ \sin(\omega_e t - \frac{4\pi}{3}) \end{bmatrix} \quad (24)$$

The total power generated in the motor can be found by Ohm's Law, shown in Eq. 25. Computing the dot products reduces the model to the form shown in Eq. 27. The dot product of the phase current vector with itself reduces to a scalar constant; of 2 times the current squared over each discrete interval; this makes resistive losses independent of electrical speed, time, and phase angle. Phase current dotted with the derivative computes to a function periodic on the interval one-third pi including the $u(0)$ and $\delta(0)$ functions. The lateral limits at zero converge to zero, making power losses through the inductor zero. The dot product of voltage and current equates to the expression shown in Eq. 26. Computing the average of the piecewise trigonometric terms over the period equates to a constant $\sqrt{3}$. Equation 27 is equivalent to Eq. 28, in terms of line to line voltage which is an alternate form of the equation.

$$P_{gen} = (\vec{V}_{LN} \cdot \vec{i}) + \left(L \left(\frac{d}{dt} \vec{i} \cdot \vec{i} \right) + R(\vec{i} \cdot \vec{i}) \right) \quad (25)$$

$$\vec{V}_{LN} \cdot \vec{i} = V_{p,LN} i_{out} \left\{ \begin{array}{ll} \sqrt{3} \cos(\omega_e t) & 0 \leq \omega_e t < \pi/6 \\ \sin(\omega_e t) + \cos(\pi/6 - \omega_e t) & \pi/6 \leq \omega_e t < \pi/2 \\ \sin(\omega_e t) - \cos(\omega_e t + \pi/6) & \pi/2 \leq \omega_e t < 5\pi/6 \\ -\sqrt{3} \cos(\omega_e t) & 5\pi/6 \leq \omega_e t < 7\pi/6 \\ -(\sin(\omega_e t) + \cos(\pi/6 - \omega_e t)) & 7\pi/6 \leq \omega_e t < 3\pi/2 \\ -(\sin(\omega_e t) - \cos(\omega_e t + \pi/6)) & 3\pi/2 \leq \omega_e t < 11\pi/6 \\ \sqrt{3} \cos(\omega_e t) & 11\pi/6 \leq \omega_e t < 2\pi \end{array} \right\} \quad (26)$$

$$P_{gen} = \sqrt{3} V_{p,LN} i_{out} + 2R i_{out}^2 \quad (27)$$

$$P_{gen} = V_{p,LL} i_{out} + 2R i_{out}^2 \quad (28)$$

Assuming the motor is balanced, peak line to line voltage will be the same across the phases, thus computing the peak voltage for a single phase is sufficient. It is known that regardless of path, one phase will always flow current out while a different phase offers the return path. Following a path through Fig. 16 yields the following result shown in Eq. 29. This result could also be obtained by dividing the electrical power equation by DC current, or by the Kirchoff voltage rule as described.

$$V_{p,LL} = \sqrt{3} K_v \omega_e - 2R i_{out} \quad (29)$$

3.2.4 Combined System Model

Lastly, combining the models together yields the following equations for the power generation system, as shown in Eqs. 30-32. The diode loss term, $\Delta V_D i_{out}$ is given by the rectifier manufacturer as a function of current.

$$P_T = (V_{out} + \Delta V_D) i_{out} + 2R i_{out}^2 + I \dot{\omega}_m \omega_m + c \omega_m^2 \quad (30)$$

$$P_T = \left(\frac{\pi}{3} \right)^2 V_{DC} i_{DC} + P_{l,rect}(i_{DC}) + \left(\frac{\pi \sqrt{2}}{3} \right)^2 R i_{DC}^2 + I \dot{\omega}_m \omega_m + c \omega_m^2 \quad (31)$$

$$V_{DC} = \frac{3}{\pi} (\sqrt{3} K_v \omega_e - \frac{2\pi}{3} R i_{DC} - \Delta V_D) \quad (32)$$

A parameter of interest is the overall system electrical efficiency, which is defined as the ratio of system output power to turbine input power. This is useful for design considerations, as

electrical efficiency will be written as a function of system parameters as shown in Eq. 33. This will effectively allow the system components to be optimized based on customer requirements, such as load power. The equation for overall system electrical efficiency is shown in Eq. 34 in terms of the component level loss terms. It is important to note that losses are proportional to a polynomial in current, and a square of shaft speed, however loss terms which depend on current are independent on shaft speed directly. These parameters can be combined as the voltage is measured and the speed constant of the generator is known; these two terms are and related by shaft speed. One key assumption in this equation is the system is steady.

$$\eta_{elec} = \left(\frac{3}{\pi}\right)^2 \left(1 - \frac{P_{L,rect}(i_{DC}) + \left(\frac{\pi\sqrt{2}}{3}\right)^2 Ri_{DC}^2 + c\omega_m^2}{P_T}\right) \quad (33)$$

$$\eta_{elec} = \left(\frac{3}{\pi}\right)^2 \left(1 - \frac{P_{L,rect}(i_{DC}) + P_{L,ohmic}(i_{DC}^2) + P_{L,m}(\omega_m^2)}{P_T}\right) \quad (34)$$

3.3 Design of Experiment I: Electrical System Characterization

For the first phase of testing, the electrical system characteristics were evaluated. For simplicity, the turbine engine core was replaced with an electric drive motor to allow for simple electrical power measurements and easy comparison between input and output powers. A list of components used in this experiment and their power ratings can be shown in Table 3.

Table 3. Components used in experiment for electrical system characterization

Motor	Function	KV [RPM/V]	Power [kW]
Rimfire 50cc	Drive Motor	230	5
Turnigy Rotomax 100cc	Generator	167	8
Vishay 3-Phase Rectifier	Rectifier	-	10
Castle Creations 160HV	Electronic Speed Controller	-	8
JP Hobby 120mm EDF	Electrical Load	760	5

The test setup can be shown in Figure 17. Beginning on the left, the drive motor is coupled to the generator via an aluminum misalignment-tolerant shaft coupler. This coupler was used in place of a rigid steel shaft coupler; this subtle change made it possible to test at higher shaft speeds but imposed a limit of 6000 RPM per the manufacturer recommendations. The voltage, which comes out in three-phase, must be rectified before a measurement is taken by the GT Power inline power meter. The GT Power measures eight DC electrical parameters including voltage, current, power, and total usage at high resolution, with an instrument range appropriate with that of the experiment. The range and resolution of the sensor for each parameter can be shown in Table 4. The input power to the drive motor is measured with a second GT Power of the same resolution. Rotational speed was measured by using an optical sensor and reflective tape, and calibrated against a voltage pulse counter incorporated into the Castle Creations ESC controlling the drive motor. The ESC is preprogrammed through CastleLink software to count voltage pulses, or each time a pole passes a coil; this pulse counter gives a very accurate readout RPM with no post-processing required. The difference between the two methods was on the order of ± 3 RPM at 6000, or $\pm 0.05\%$ at 6000 RPM. Hysteresis was checked by stepping back down the test matrix in reverse, which showed less than 0.5% variation on the data measured. Results were obtained in real time without data logging, so values presented as results signify a single data point representative of the time averaged value under steady operation.

Table 4. Range and resolution of GT Power inline power meter

	<i>Min</i>	<i>Max</i>	<i>Resolution</i>
Voltage (V)	0	60	0.01
Current (A)	0	180	0.01
Power (W)	0	6554	0.1
Total Usage (W-hr)	0	6554	0.1

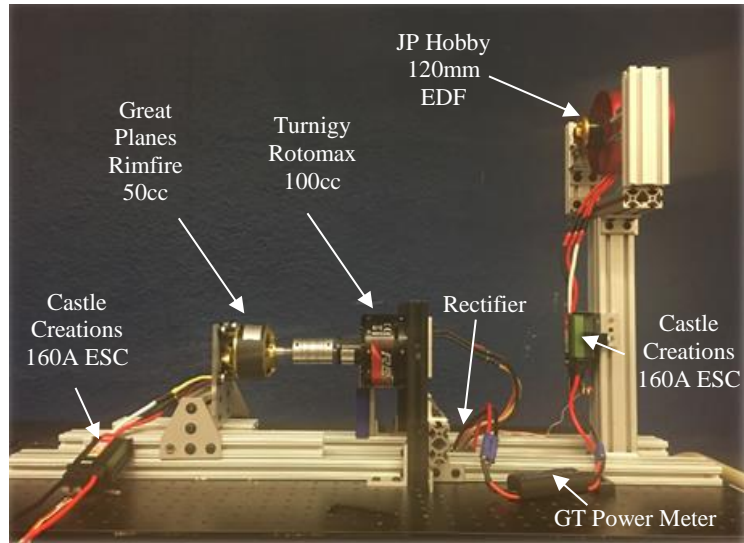


Figure 17. Photo of test setup, including labeled components

Data collected during the experiment were drive motor input power (electrical), generator shaft speed, and rectified power for each point detailed in the procedures. The torque, a derived quantity, will be determined by taking the measured power input minus the no load power at the unique shaft speed and dividing by the shaft speed in radians per second, as shown in Eq. 35. Torque is a derived quantity with respect to the electrical power input, but is sufficient for the purpose of this study. The test matrix can be shown in Table 5.

$$\tau = \frac{P_{in} - P_{NL}}{\omega_m} \quad (35)$$

Table 5. Test matrix evaluated during electrical system characterization

	Test Range	Step Size
Drive Motor (RPM)	0-6000	500
Electrical Load (%)	0-100	25

3.4 Test Facility

Testing was performed in the Oklahoma State University 3-ft by 3-ft wind tunnel facility, featuring a 1:16 contraction ratio and velocities up to 120 mile per hour. The wind tunnel is picture in Fig. 18. The tunnel is outfitted with an Inconel five-hole probe controlled with the

programming environment LabVIEW for high temperature vorticity characterization. Additionally, the facility can equip an anemometer, hot wire, and Kiel probe for other flow characterizations and atmospheric condition measurements.



Figure 18. Photo of the flexible use wind tunnel test facility

Only the live turbine engine tests were executed in the wind tunnel, with a near static freestream velocity. This is done to exhaust the turbine products of combustion, rather than to simulate a flight condition. The freestream speed was deemed low enough to not affect the performance of the turbine.

The electrical system tests were performed outside of the wind tunnel, however for future testing with the turbine engine, the wind tunnel will be required.

3.5 Results I: Electrical System Characterization and Theoretical Performance

There are two system parameters which contribute to losses in the power system: current and shaft speed. Consequently, the loss terms which vary with respect current are independent of shaft speed and vice versa. Each will be discussed in detail in the following sections.

3.5.1 Friction Losses vs. Rotational Speed

To evaluate frictional losses, the system was tested with no electrical load at a steady operating point. Data on the input power required was taken at intervals of 500 rev/min; no-load effects and ohmic losses from the drive motor are well quantified and were subtracted out. The equation of motion under these conditions reduces to that shown in Eq. 18. The plot of damping coefficient and total power loss are plotted vs. shaft speed in Fig. 19. It is important to note that

damping coefficient carries a high uncertainty at low shaft speed values, due to resolution of the transducer.

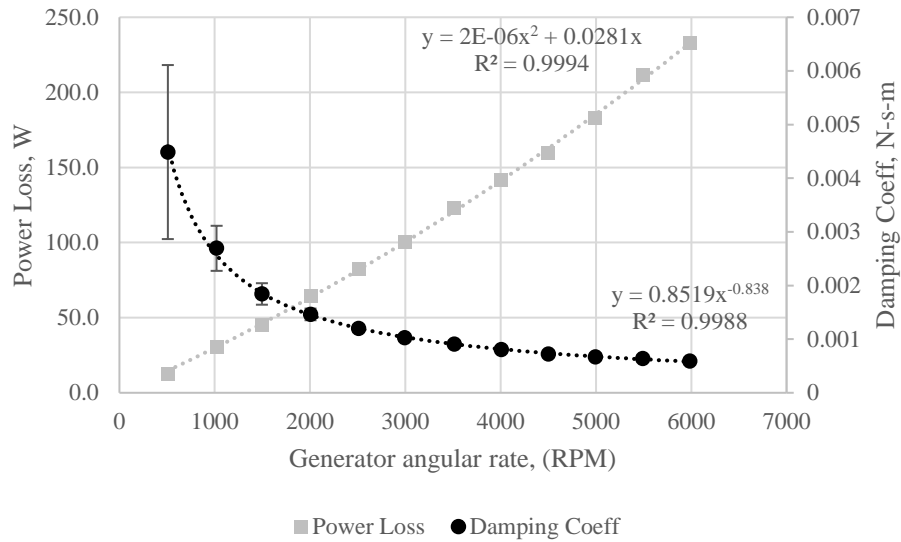


Figure 19. Plot of damping coefficient and total frictional loss vs. shaft speed

3.5.2 Theoretical Losses and Theoretical Efficiency

To evaluate theoretical losses in the generator and rectifier, Eq. 33 was used. The manufacturer gives loss data for the rectifier as a function of current; generator ohmic losses are a function of a constant times current squared. The friction values used are those obtained experimentally in Fig. 19. Using a manufacturer specified value of 0.021 ohm for generator phase resistance, total losses were tabulated and theoretical electrical efficiency was plotted over a range of current for different shaft speeds. The desired system input is on the order of 7.3 kW, thus any values of theoretical input power greater than this are not included in Fig. 20.

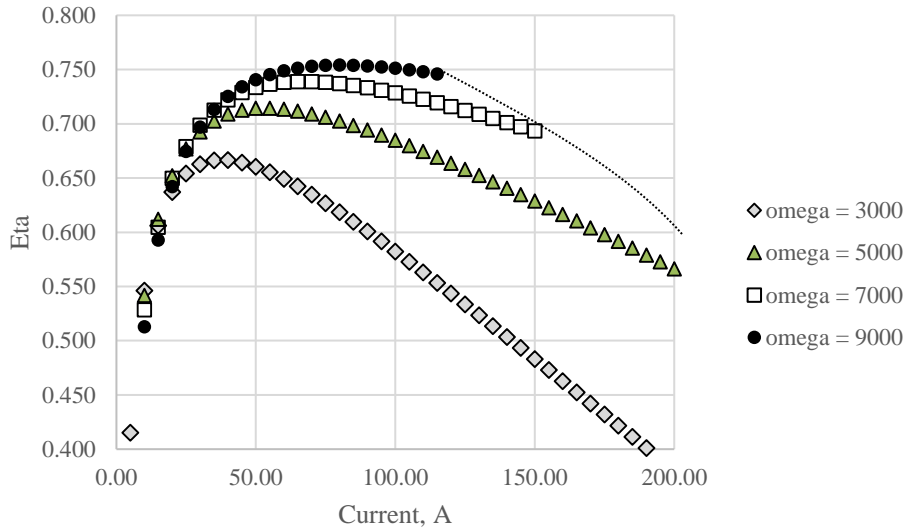


Figure 20. Plot depicting the theoretical electrical efficiency carpet plots as a function of current and shaft speed

Electrical efficiency depends on several parameters; some parameters are component specific while some are specific to the operating condition. Parameters such as winding resistance, rectifier voltage drop, and friction coefficient are specific to the components selected. High-efficiency systems will have components which minimize these parameters. In addition to this, operating condition contributes toward the overall system efficiency. Taking into consideration the relationship between voltage and shaft speed, it can be clearly shown in Fig. 20 that operating this specific system as a high voltage system generally outperforms a low voltage system with the same component parameters. In the system analyzed in this study, current losses dominate over frictional losses; it is important to note that frictional losses go as shaft speed squared, however the efficiency continues to rise. This, paired with Eq. 33 tells that as the proportion of voltage lost across the resistive and semi-conductive elements decrease, the system will operate at a higher electrical efficiency, even with the penalty of friction. There is an upper limit on this, however, which can be shown on Fig. 21, where the peak electrical efficiency is fit as a function of current; data labels indicate the shaft speed. For a system with the parameters shown, the peak theoretical electrical efficiency obtainable without exceeding 7.3kW input is on

the order of 0.77, which is consistent with literature in this area. [35]. If the actual turbine power curve were included this carpet plot would look slightly different, as the peak power able to be produced would vary as a function of shaft speed.

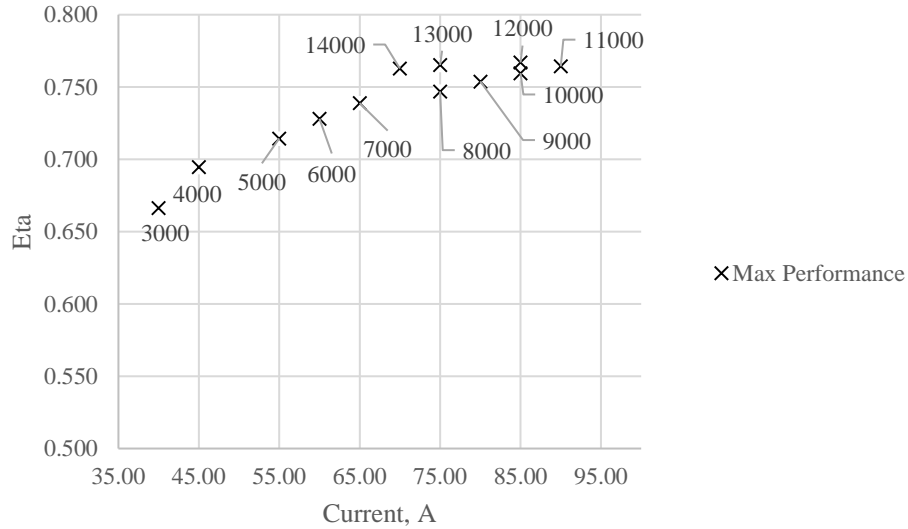


Figure 21. Peak theoretical efficiency as a function of current and shaft speed

3.5.3 Power System Voltage

One basis of comparison for the model is how well it predicts voltage. The measured voltage is plotted as a function of shaft speed in Fig. 22; the theoretical voltage is also plotted as a function of shaft speed and current, as suggested in Eq. 32. The voltage prediction aligns well with the modeled values of voltage under load. No error bars are depicted as the signal to noise ratio is very high. The same is true for the model, as shaft speed and current are both measured at high signal to noise. Being able to accurately predict the output voltage over a large range of current and shaft speed indicates that output power can be estimated at a high degree of certainty, as current is load dependent.

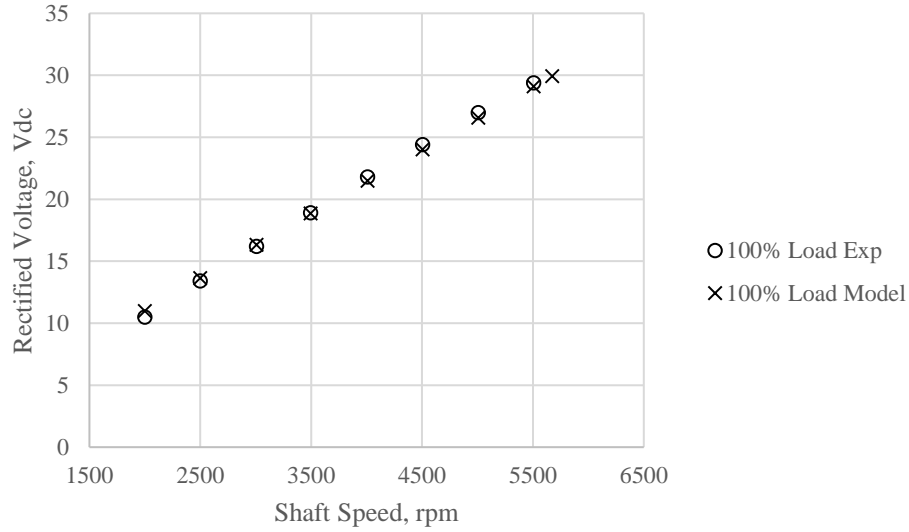


Figure 22. Plot of actual voltage vs. shaft speed against modeled values

3.5.4 Performance Parameter: Electrical Efficiency vs. Modeled Response

The measured electrical efficiency vs. current is shown in Fig. 23 for several load cases.

This value was computed using Eq. 36, shown below.

$$\eta_{exp} = \frac{P_L}{P_{in} - P_{NL}(\omega_m)} \quad (36)$$

Each data point is at a unique voltage, which is related to shaft speed and current in Eq. 41. The estimated performance is also plotted for the measured parameters as a function of Eq. 42. Electrical efficiency is a derived quantity thus carries some uncertainty, however error bars are not pictures as Kline-McClintock method for resolution error yielded uncertainty less than 1 percent on calculated theoretical efficiency. The actual efficiency carries a maximum resolution error of 11.6 percent of the calculated value; this is at the smallest value of current, however for current values greater than 16 amps, it quickly deteriorates to less than 1.5 percent.

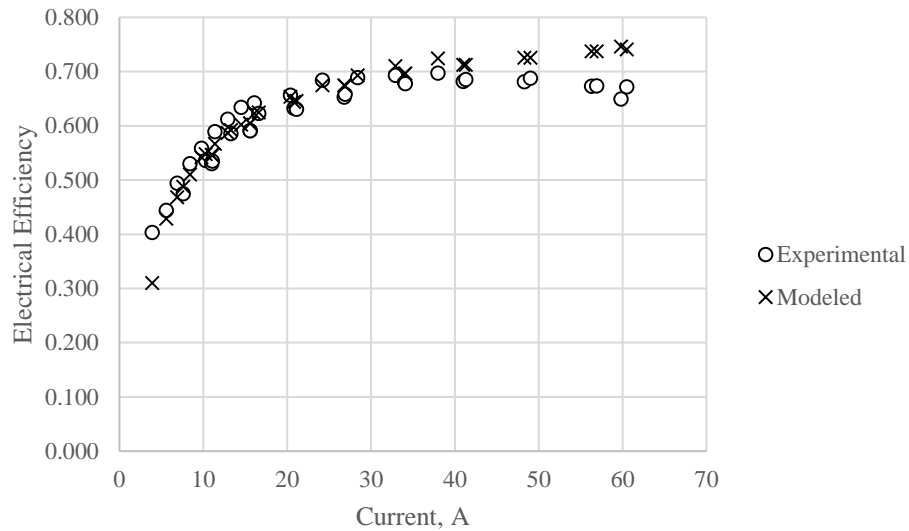


Figure 23. Plot of theoretical efficiency vs. actual efficiency as a function of shaft speed and current

As depicted in Fig. 23, the model is a good estimator of electrical efficiency at low values of current, however as current tends to increase the model begins to over-predict the system electrical efficiency. There are higher order effects which occur at higher values of current such as harmonics inside the motor casing. In addition to copper losses, iron losses within the magnets also become notable at higher frequencies and currents; these losses are difficult to predict. In addition to these effects which were not modeled, it is expected that the majority of the divergence was due to heating up of semi-conductive components, specifically diodes. Diode properties change as a function of heat, which likely caused the divergence at high values of current; power loss and consequently heat loss across a diode goes as current. With these considerations in mind, the model does quite well as the theoretical maximum for each unique case is on par or slightly above the experimental value. For design and overall sizing purposes, the model does well at estimating the system level trade-offs as well as the expected efficiency and voltage. Special attention should go toward the operating point when designing a turboelectric power system. The relations developed here can be used to size and select system level components if the operating condition is known, and vice versa.

3.6 Turbine-Driven Experiment Observations

The same test matrix evaluated in the previous section was attempted with the Kingtech K60TP in place of the Great Planes Rimefire 50CC. In addition to this a different misalignment coupler was used. The new shaft coupler is rated to up to 10,000RPM, is vibration-damped, and can handle misalignments up to 1 degree axially. The new benchtop test arrangement is shown in Fig. 24. The objective of this study was to assess issues that may arise when integrating a turbine engine into the power system. Issues assessed include controls and installation issues.

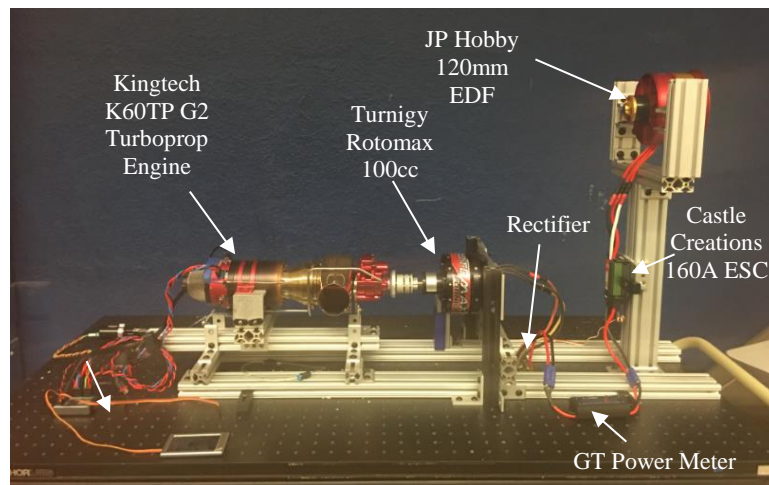


Figure 24. Photo of turbine-driven test, first attempt

Initially, the turbine engine and the EDF were controlled from the same receiver on separate channels, allowing a single operator to adjust throttle of each component simultaneously. The turbine engine was started and allowed to reach idle. The idle point was around 3000RPM on the output shaft and was steady in nature, this corresponds to an output voltage on the order of 18V. Next, the ducted fan was set into motion at a low throttle setting, and began drawing current. It was observed that immediately upon setting the fan in motion, the power turbine loaded and the shaft speed decreased below threshold voltage, which stopped the fan. This result was expected as the mechanical power had not changed, but the current increased, indicating that torque must also increase. The turbine throttle was then brought up to around 10 percent with a linear throttle curve, indicating approximately 10 percent shaft power; the fan was then set in

motion again. Again, the turbine loaded and the fan did not shut off. The throttles were then brought up near-simultaneously in attempt to reach the first operating condition of 25% EDF throttle at a specified shaft speed. In doing this, the system began to exhibit marginally stable dynamics which eventually caused the power turbine to stall, which resulted in premature termination of the test. This issue occurred on multiple occasions and damaged the turbine on the final attempt. Qualitatively, the issue stems from the response time of the electrical load relative the turbine engine. The electrical load has a much faster response time than the mechanical system driving the power generation system. Ohm's Law states that the increase in current will cause a decrease in voltage, assuming the system power is not changing. This increase in current is reflected in the generator in the form of an electro-motive force (EMF), also known as "back EMF." Back EMF is defined as the voltage generated when the armature rotates inside a magnetic field. Lenz's Law states that current in a circuit generated from motion in a magnetic field is directed opposite as the change in flux, and exerts a force in the opposing direction [31-32]. This rapid increase in torque occurs before the mechanical system has time to respond, even if the throttle of both systems were brought up near simultaneously. These phenomena coupled as the current and shaft speed are dependent, and the turbine exhibited oscillatory behavior prior to stall as a result of these dynamics. This behavior was not asymptotically stable, and qualitatively exhibited a limit cycle type response with respect to shaft speed. The turbine loading fluctuated immensely and the LPT is likely designed with little stall margin, causing the stall.

3.7 Conclusions, Observations, and Recommendations I: Modeled and Experimental Results

The conclusion made as a result of the first phase of testing is in response to Research Question I [which states: What are the system level design considerations when designing a hybrid turboelectric powertrain?]. The analytical model developed in this chapter was tested and validated across a range of operating conditions which varied with respect to current and shaft speed. The validation of this design tool proved it effective in accurately showing the system level tradeoffs when designing a turboelectric powertrain and proves operating condition to be

vital. The system parameters govern the peak efficiency able to be obtained as a function of operating condition, thus careful consideration should be paid to the design point. The model developed here allows for sizing and optimum selection of components for those designing or conceptualizing hybrid powertrains for a specific mission or application, assuming the electrical load requirements to meet the objectives are known. This conclusion successfully answers Research Question I and satisfies Objective I, which states:

Objective I: Develop and evaluate a design tool which focuses on the efficiency and operability of a turboelectric system which also addresses compatibility of the components of the power generation system including the turbine, generator, and rectifier.

In addition to this, it is expected that high speed motors, (i.e. those used in ducted fans) or those with high speed ratings (RPM/V) will experience greater oscillatory effects when running in hybrid mode than low speed motors (i.e. those used in large, high-pitch propeller applications) due to the greater sensitivity to voltage. This can be mitigated by the inclusion of signal conditioning. One additional key observation was made during the testing of the system; this observation was the highly coupled nature of the system when the turbine engine is included. The system exhibited behavior described as marginally stable, and ultimately lead the realization that some form of electrical damping is necessary. Electrical damping can come in several forms which include batteries, capacitors, and inductors. The recommendation moving forward is to include electrical damping in the system in addition to a battery. This will not only assist with electrical system damping, but will also help smooth the signal exiting the rectifier as described above. The battery will serve as a backup in case of system failure and also as a supplemental power supply. Some form of semi-conductive device will be required as protection from overvoltage/overcharging the battery, as will a device to regulate the current. This type of device is known as a power management unit. (PMU). PMUs are sold by several companies commercially, however they are in general large and costly. Instead, the recommendation is to

design and fabricate an in-house PMU which does the tasks described above. The system would be fully integrated, including a signal conditioning/filtering device, electrical damping device, and a device which allows for bidirectional current flow to and from the battery with a regulated input and output. Active throttle control of the turbine engine is also necessary, however this feature should be built into the PMU. This topic will be discussed in greater detail in the following sections.

CHAPTER IV

ELECTRICAL SYSTEM REFINEMENT AND TURBINE THROTTLE CONTROL

Results from Chapter III make it clear that the electrical system needs some degree of refinement before moving on into the vehicle integration stage. The topics which will be discussed in this chapter include but are not limited to the inclusion of feedback throttle control for the turboprop engine, signal conditioning, electrical damping, and a battery. One additional topic will be addressed, which is the explanation of why the power turbine stalled during preliminary testing. The results of these experiments will help draw conclusions about the system behavior and the expected challenges moving forward..

4.1 Stage Loading vs. Current

Given the outcome of the previous phase experimentation which included the turbine engine, it was determined that additional mathematical modeling must be done to relate what type of failure occurred and how to mitigate it. Relating the electrical system to the mechanical system for a dual spool turboshaft engine is most effectively done by the use of stage loading coefficient of the power turbine, ψ . Stage loading is a performance parameter which relates the amount of work being done by the turbine stage to the total change in fluid momentum of that stage [30, 36]. Turbines are susceptible to stall at high stage loadings. Stage loading is given in Eq. 37 below.

$$\psi = \frac{g_c c_p (\Delta T_t)}{(\omega_t r_t)^2} \quad (37)$$

The power balance shown in Eq. 5 is also key, as this relates the change in total temperature to voltage and current. Equating Eq. 5 and Eq. 31 and solving for ΔT_t , the change in

total temperature can be expressed by Eq. 38. Substituting Eq. 38 into Eq. 37, the equation for stage loading can be reduced to the form shown in Eq. 39, where K_v is the phase speed rating in Volt per radian per second, i_{DC} is the current, r is the power turbine mean radius, N is the gear ratio from the turbine speed to the shaft speed, and $P/2$ is the number of pole pairs of the generator, ω_s is the shaft speed, \dot{m}_c plus \dot{m}_f is the power turbine mass flow rate, and I is the generator mass moment of inertia. This equation has not made any assumptions about steady state operation, thus relating dynamic response to turbine operability.

$$(T_{T4.5} - T_{T5}) = \frac{\left[\left(\frac{\pi}{3}\right)^2 V_{DC} i_{DC} + P_{l,rect}(i_{DC}) + \left(\frac{\pi\sqrt{2}}{3}\right)^2 R i_{DC}^2 + I \dot{\omega}_m \omega_m + c \omega_m^2 \right]}{\eta_{mech} (\dot{m}_c + \dot{m}_f) c_{pt}} \quad (38)$$

$$\psi = \frac{g_c}{(\dot{m}_c + \dot{m}_f)} \left(\frac{\frac{\pi}{3} \sqrt{3} K_v \left(\frac{P}{2}\right) i_{DC}}{N^2 \omega_s r_t^2} + \frac{I \dot{\omega}_s}{N^2 \omega_s r_t^2} + \frac{c}{N^2 r_t^2} \right) \quad (39)$$

Mattingly and Boyer [30, 36] quote typical values for mixed flow axial turbines, which can vary between 1.4 and 2.0 for high pressure turbines. For low pressure turbines or power turbines, this number will most certainly be lower, as a large portion of potential energy in the form of temperature and pressure has already been extracted through the core turbine. It is expected that a stage loading on the order of 0.5 to 1.2 is a more reasonable estimation. Given this constraints, an operating map can be generated by holding voltage constant and varying current. The governing equation for voltage is given in Eq. 41, where shaft speed will fall out given a fixed voltage and chosen current for a specific generator. This type of operation most similarly simulates a battery. This equation is a powerful tool for selection of hybrid powertrain generators given a specific electrical load and maximum stage loading coefficient for the turboshaft engine. This equation also has implications in control schemes, as surges in stage loading due to rapid loading or unloading of the turbine can cause power turbine stall.

Plotted below in Fig. 25 is an operational map for the 7.3kW turboelectric system utilizing the K60TP, Rotomax 100CC generator, and Vishay three-phase full wave rectifier. The parameter of interest is the stage loading as a function of current for a fixed voltage. Shown

below are lines of constant voltage, which show the behavior of stage loading under a constant voltage with variable current. It is important to note that in the plot the steady assumption has been made, however transient results can also be analyzed and assessed using the same methods and techniques. Stage loading plotted as it is below is not dimensionless and has a multiplier of mass flow rate; at this time, there is not an accurate way to measure mass flow rate of air through the turbine with reasonable accuracy, but it will not be constant throughout the operational map. The plot shows several things, however the primary results of interest is the increase in stage loading as voltage is decreased. For the same current, stage loading will be on the order of 80 percent higher for the 20V load case in comparison to the 40V load case. This steady behavior shows clearly how issues can arise when driving low voltage system; to counter this, signal conditioning such as buck conversion can occur which will allow power to be generated at a higher voltage initially, but then stepped down to a voltage appropriate for the vehicle power system.

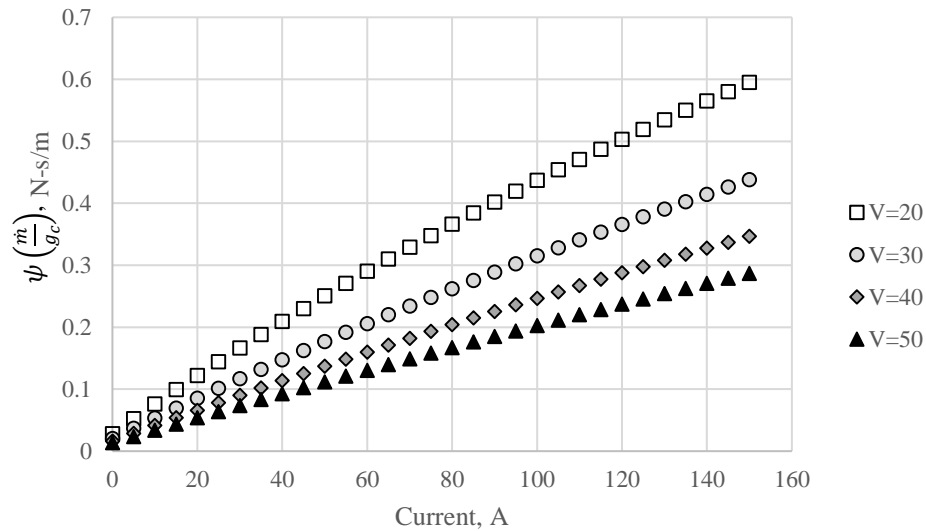


Figure 25. Stage loading vs current for values of constant voltage

4.2 PID Control Theory

In order to counter the oscillatory effects shown in the turbine based system demonstration, an active throttle controller must be designed and implemented. The type of controller selected for this application is the proportion-integral-derivative (PID) controller. PID control has been long used among engineers and is highly revered for its simplicity to integrate. PID controllers can be made both digital and analog, with the digital requiring micro-processing chips such as Arduino, Raspberry Pi, or NVIDIA micro-computer boards. The controller in this study will be made on an Arduino board which will undergo several iterations. The first iteration will be proportion control only, where the second and third iterations will include integral and derivative gains, if needed. PID control can best be described by Eq. 40 [37] where k_p is the proportion gain, k_i is the integral gain, k_d is the derivative gain, $e(t)$ is the error at some time t , and $u(t)$ is the control signal. Error is calculated by Eq. 41, where r is the reference state or setpoint, and y is the value at some time t . In the turboelectric system described in Chapter III, the only parameter being controlled to regulate turbine throttle is the fuel flow rate, as shown in Eq. 6.

$$u(t) = k_p e(t) + k_i \int_0^t e(\tau) d\tau + k_d \frac{de}{dt} \quad (40)$$

$$e(t) = r - y \quad (41)$$

Voltage is a function of shaft speed, while current is a function of the load resistance.

Rearranging Eq. 31 and computing several derivatives yields the equations shown below in Eqs. 42-44.

$$\frac{dV_{DC}}{d\omega_m} = \left(\frac{3}{\pi}\right)^2 \frac{(I(\dot{\omega}_m \omega_m + \dot{\omega}_m^2) + 2c\omega_m - \tau_t)}{i_{DC}} \quad (42)$$

$$\frac{dV_{DC}}{di_{DC}} = \left(\frac{3}{\pi}\right)^2 \left(\frac{(\Delta V_d + \frac{4\pi^2}{9} R i_{DC}^2)}{i_{DC}} - \frac{(P_{l,rect}(i_{DC}) + \left(\frac{\pi\sqrt{2}}{3}\right)^2 R i_{DC}^2 + I\dot{\omega}_m \omega_m + c\omega_m^2 - \tau_t \omega_m)}{i_{DC}^2} \right) \quad (43)$$

$$\frac{d^2 V_{DC}}{di_{DC} d\omega_m} = -\left(\frac{3}{\pi}\right)^2 \frac{(I(\dot{\omega}_m \omega_m + \dot{\omega}_m^2) + 2c\omega_m - \tau_t)}{i_{DC}^2} \quad (44)$$

The mixed partial derivative shows that for a specific torque from the turbine, and a fixed turbine power the change in voltage with respect to each parameter is strongly coupled. It is important to note the inverse current squared relationship, as this means the voltage rate of change is less sensitive to changes at higher values of current, but is extremely sensitive at low values of current. Though these factors are useful, they are highly theoretical so the control model will be tuned based on the measured system response relative to the control system parameters.

4.3 Design of Controller: Proportion Control

Results from the Chapter III indicated the need for throttle control; with these considerations in mind, a feedback controller was designed utilizing an Arduino Uno board. The Arduino board had several key functions, including but not limited to starting the turbine, sending and receiving both analog and digital signals, performing calculations, as well as writing the system state to a serial port for post processing. Each of these aspects were approached individually and evaluated thoroughly to ensure quality. The throttle control architecture is shown below in Fig. 26. Some of the specific details of the throttle control algorithm will not be shared in this document to protect sensitive information.

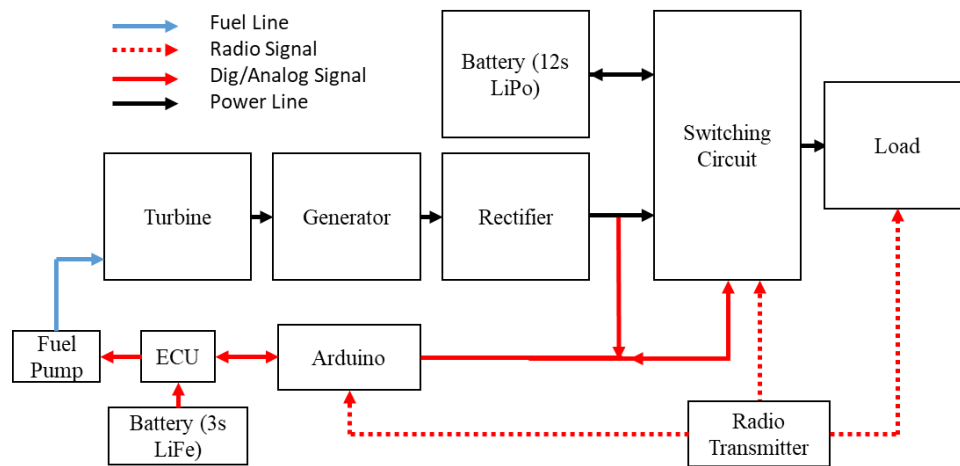


Figure 26. Schematic of the hybrid system with controller

4.3.1 *Starting/Stop Turbine*

In order to start the turbine, a small DC starter motor is attached to the front of the turbojet engine; this starter is controlled by the engine control unit (ECU) which is powered by a 3 cell lithium-ferrite (LiFe) battery, as shown in Fig. 26. The ECU also has a digital servo port, RxThro, which allows the turbine engine to be controlled from a digital input, such as a RC radio or servo tester. Given the high complexity associated with independently controlling two throttles manually, the turbine must be controlled separately via feedback control as mentioned in the previous section. The Arduino will act as the liaison, reading signals sent from the radio to the switching circuit and interpreting them with programmed logic. It is important to note that the KingTech turbine start sequence is initiated by sending three successive throttle commands. These commands are idle, beyond half-throttle, and returning to idle in order in a time-step less than three seconds. In order to cut the turbine engine, a sub-idle command is all that is needed. On an aircraft, this would be done by reducing the engine trim at the idle point.

The signal type is a digital signal thus utilizes a pulse-width-modulation (PWM) style signal for control. It is important to note that the engine throttle curve is set to linear, which indicates a linear mapping between servo position and power; there are also options built in for exponential throttle curves, however due to complexity associated with nonlinear control they were not considered for use with this system.

4.3.2 *Voltage Sensing: Rectified Voltage*

Easily switching between hybrid and battery configurations requires low equipotential difference between the two sources. As shown in Fig. 26, the rectified voltage feeds into the active switching circuit, which is controlled from the Arduino. The Arduino measuring the voltage utilizes 10-bit analog pins with a range of 0-5V, indicating that the voltage must be passively stepped down to a suitable range. To do this, a voltage divider must be designed and built for this application. The second consideration is the shape and frequency of the waveform; due to the rectification process, it is expected that signal conditioning will be required. This can

be done by adding a smoothing circuit as recommended by [38], making both the signal and power mimic a DC signal more closely. For this phase of testing, only a voltage divider will be realized into the physical system as the signal conditioning device had not been decided upon prior to testing.

4.3.3 Voltage Divider Design

A voltage divider was designed to accompany the turboelectric system throttle controller. The voltage divider will be load dependent, thus the electric propulsion system directly constrains the design. For this specific application, a target voltage of 47V is desired at the output of the rectifier; in order to center this voltage in the range of the sensor, a gain of 18.8 is required. Another consideration when designing a voltage divider is the amount of current which will be flowing through the board. Arduino pins are limited to no more than 40mA, thus to ensure safe operation throughout the entire voltage range a peak current value of no more than 10mA was set for calculations. Appropriate design equations shown in Eqs. 45-46. It is important to note that there are infinitely many combinations of resistances which will achieve the desired gain and meet the current constraint.

$$G = \frac{R_1}{R_{eq}} = 18.8 \quad (45)$$

$$R_{eq} \geq \frac{V_L}{i_{limit}} = 4.7k\Omega \quad (46)$$

When determining the resolution of the measurement, the voltage divider gain must be used in addition to the resolution of the Arduino analog pin resolution. Given the range of the sensor, 5V, the resolution of the sensor, 10 bit, and the gain of the voltage divider, 18.8, a full scale output resolution on the order of one-twentieth of a volt is realized. This is shown using Eq. 47.

$$res_{FS} = \pm \frac{1}{2} \left(\frac{5V}{2^{10}-1} \right) G = 46mV \quad (47)$$

4.3.4 Controller Logic

The system will utilize a PID controller as discussed in the previous sections. Some additional logic must be done by the microcontroller, however is not discussed in detail for aforementioned reasons. These elements of the program will be isolated and quality tested during the benchtop test before they are combined into the final throttle control model. During the testing and evaluation phase, it is crucial to ensure that data is being written real time to the operator, as certain components are at risk of overvoltage; the operator needs some type of real time feedback should the system malfunction or start to “run away”.

4.4 Design of Experiment II: Turbine Throttle Control

To test the turbine throttle controller, a test similar to the setup in Chapter III was used; the 7.3 kW turboelectric system described instead powers a single electric motor and propeller. The motor and propeller selected are compatible with each other in terms of RPM and power, and generate a sufficient amount of thrust for the fixed wing aircraft selected as a demonstrator vehicle. The selected components are given in Table 6 below.

Table 6. List of components used in turboelectric test and their power rating

<i>Component</i>	<i>Function</i>
Kingtech K60TP	Turboprop (7.3kW)
Rotomax 100CC	Generator (8kW)
Vishay 3-Phase Full Wave Rectifier	Rectifier (10kW)
Castle Creations 160HV	Electronic Speed Controller (8kW)
E-Flite Power 360	Propulsor Motor (6kW)
Engal 3 Blade 20x12	Propeller (\approx 5kW @ 8000 RPM)

Testing consisted of several key legs, which are discussed in greater detail below. The measurements taken included the turbine engine throttle servo position, rectified DC voltage, and throttle position of the load (electric motor and propeller). Test points included moving from idle

(17VDC) up to steady turbine operation under no electrical load (47VDC), gradually increasing from no electrical load to full electrical load under a near-constant voltage, steady operation at full electrical load under constant voltage, and gradual decrease from full electrical load to no electrical load. The result of this study, the voltage response, will be used to analyze the system damping, steady state friction of the turbine engine, and signal to noise ratio at steady operation. Due to nature of diode rectification in multipole motors, some amount of high-frequency noise is expected under steady operation without the smoothing circuitry installed.

Voltage measurements were taken from the voltage divider circuit discussed in the previous section. The divider used in this experiment was designed to step 41VDC down to 2.5VDC. The analog-digital converter (ADC) on the Arduino has a 10 bit resolution, which has a full-scale output resolution on the order one-twentieth of a volt, as shown in Eq. 47 and indicating a very high signal to noise ratio. The throttle position of the turbine engine and electric motor are normalized, as mechanical power of the turbine is not being measured directly.

4.5 Results II: Proportion Control Response

The turbine throttle control response as a function of voltage is shown in Figure 27. The control algorithm employs Proportion (P) feedback control; the controller was designed and tuned by trial and error over several iterations with the final tuning presented in Fig. 27. At this stage current is not being sensed by the throttle controller as there is only a single source, however current is measured by the electronic speed controller driving the BLDC motor. It is important to note that the KingTech K60TP has an adjustable throttle curve, which relates mechanical power out to servo position in; the ECU throttle curve for this test is linear, which means throttle position is mapped linearly with respect to mechanical power. Lastly, an artificial limit was imposed on the controller for the benchtop testing to ensure safe operation as well as not damage any components. Turbine throttle is limited to 89 percent. It is important to note that there is no switching circuit, battery, or smoothing circuitry included in the system. The peak power draw of

the electric motor and propeller is on the order 3.5kW on average. With these things in mind, there are several conclusions which can be drawn from the data.

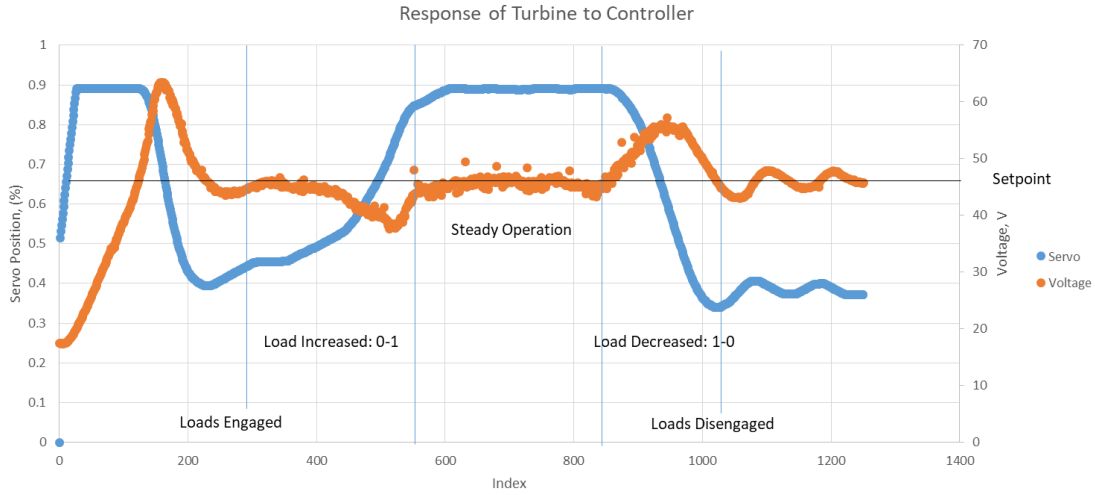


Figure 27: Turboelectric system response to proportion control

4.5.1 Electrical System Considerations

One immediately realization is that additional tuning of the controller is required; this is realized by the 15 Volt overshoot at the beginning of the operation. Utilizing Eq. 48 and the percent overshoot, PO, the damping ratio can be tabulated using a 31.9% overshoot. This calculation is shown below and yields a damping ratio of 0.342.

$$\zeta = \frac{\sqrt{\left(\ln\left(\frac{PO}{100}\right)\right)^2}}{\sqrt{\pi^2 + \left(\ln\left(\frac{PO}{100}\right)\right)^2}} \quad (48)$$

This damping ratio indicates that the system is extremely underdamped. Typical desirable values for damping coefficient range from 0.5-0.9, with an average value of around 0.7 being desired for most applications. This large overshoot likely needs derivative gain to slow the approach during spool up (PD). Additional evidence is shown at the end of the operation when the loads disengaged. Under no load, the system struggled to find its set point of 47V, (47V mimics the voltage of 12s Lithium-Polymer (LiPo) battery under load), resulting in a less severe overshoot but a clear oscillation on the signal voltage and throttle.

As expected, under steady operation noise is observed in the voltage data; this reinforces the need for signal conditioning, as the P gains are calculated using this analog signal. This noise is occurring at a higher frequency than the Arduino sample rate, as the signal is clearly aliased. This high frequency noise can be attributed to passive diode rectification in the circuit, as the three-phase full wave rectifier will rectify peak line-to-line voltages, resulting in this high-frequency ripple. Because the signal is aliasing, this indicates that the clock speed of the processor is less than that of the noise; this can be addressed under several different pathways. The BLDC generator used in a 24 pole device, indicating that there will be 12 voltage pulses per mechanical rotation appearing off of the rectifier. The mechanical speed measured was on the order of 7000 rev/min, indicating an electrical speed of 1400 Hz. The sample rate should be at least twice the frequency being measured to detect a frequency, but would be ideally ten times greater than the frequency being measured. Additionally rather than bumping up the speed of the Arduino, the signal should also be manipulated via smoothing circuitry as discussed in the previous sections. Signal conditioning is necessary not only for this, but for implementation of the derivative gain as high frequency periodic noise will be amplified in the system. Equation 49 shows an example of how this would appear in the system.

$$\frac{d}{dt} \left(A \sin \left(\frac{f}{2\pi} t \right) \right) = \frac{f}{2\pi} A \cos \left(\frac{f}{2\pi} t \right) \quad (49)$$

Overall, the system did exhibit stable behavior, but indicated improvement can be made to the control logic by including signal conditioning and rate control to decrease the overshoot. It is important to note that signal conditioning via hardware would very likely increase the system damping. Digital rate control is contingent upon successful implementation of this signal conditioning, as rate control in the current configuration would likely cause system instabilities due to the high frequency noise.

4.5.2 Mechanical System Observations

From the mechanical system perspective, the key observation made is the settling point of the turbine engine under no load. Under no load, steady operation, the mechanical system will behave as seen in Eq. 50 below. This equation was derived from Eqs. 5 & 31 by applying the steady, unloaded assumptions.

$$\eta_{mech}(\dot{m}_c + \dot{m}_f)c_{p_t}(T_{T4.5} - T_{T5}) = \tau_s \omega_s = c \omega_m^2 \quad (50)$$

The settling point of the turbine engine oscillated between 35 to 40 percent, with an average centered around 37 percent throttle. When the linear throttle mapping is considered, this indicates that 37 percent of the turbine engine mechanical power is dissipated to frictional losses somewhere in the system. These losses could be attributed to several things, including the health of the generator, turbine engine bearings, and the alignment of the mechanical coupler. A second theory is that the output power of the turbine engine is not consistent with the manufacturer specifications due to engine health, operating environment, or other factors. As a precaution moving forward, the system will be uncoupled and recoupled to ensure that the alignment of the two shafts is satisfactory.

4.6 Conclusions, Observations, and Recommendations II: Design of Throttle Controller

The throttle controller designed and realized in this section is a good precursor to the robust engine controller discussed in the upcoming sections. The controller described in this section successfully measures voltage, applies proportion control logic, and regulates turbine throttle without operability problems. System overshoot and underdamping was observed as well as high frequency noise during steady operation, indicating the need for electrical system damping, signal conditioning, and digital rate control; rate control is contingent upon implementation of signal conditioning. A smoothing circuit could slow the system, increasing the damping coefficient an appreciable amount. High system friction was also observed which invoked a thorough system check involving realignment of the generator and turbine output

shafts. It is inconclusive at this time if this changed the overall system friction. This phase of testing partially answers Research Questions I, II, and III, [which state: 1. What are the system level design considerations when designing a hybrid turboelectric powertrain? 2. What are the vehicle level design considerations when designing a vehicle utilizing a hybrid turboelectric powertrain? 3. Is a turboelectric sUAS a feasible alternative to purely electric sUAS?] and partially satisfy each of the three overall objectives. In relation to the overall Objectives I, II, and III the key takeaways are as follows:

Objective I & II, which are as follows:

Objective I: Develop and evaluate a design tool which focuses on the efficiency and operability of a turboelectric system which also addresses compatibility of the components of the power generation system including the turbine, generator, and rectifier.

Objective II: Determine vehicle-level challenges and constraints associated with integration and installation of the turboelectric system aboard a fixed-wing aircraft and mitigate/address them.

Turboelectric systems should be designed with a smoothing circuit. Not only does this affect the accuracy of the measurement used to control the turbine engine used to drive the system, but it also affects the waveform being supplied to the load and onboard avionics. This is a key feature, as high ripple can negatively affect high speed motors. Motors with high speed ratings are more sensitive changes in voltage which affect the rotational speed and consequently thrust.

Objective III, which is as follows:

Objective III: Demonstrate feasibility of turboelectric propulsion and power as an alternative to all electric systems in terms of operability.

The turboelectric system tested and evaluated in this chapter showed promising results for feasibility. The system was able to produce sufficient power to drive an electric motor and

propeller at some appreciable thrust value; the power generated by the turboelectric system, 3.5kW was on par with the power draw when powered by a battery driven system. This result alone shows that turboelectric systems at the small scale can compete with batteries in terms of electrical power capabilities.

Moving forward, it was determined that for the first phase of integration the battery backup discussed in the previous chapter will be implemented; this element was excluded for benchtop testing to not add additional complexities to the system being evaluated. This battery backup will interface with the switching circuit, which is controlled by the Arduino microcontroller. The switching circuit should include a system which allows for charging, however does not necessarily allow the capability of supplemental power; a system which does supply supplemental battery power will be needed to accommodate a distributed propulsion and power VTOL system during hover operation. By separating these two systems, it allows the fixed wing CTOL aircraft system to be more rapidly advanced, as fixed wing aircraft have glide capabilities making the segregated power system described above attainable in the required timeframe. The active switching circuit described above will be designed, realized, and integrated in the following sections. In the next phase of experimentation, integration of the system will be assessed on a Mugin 4500 airframe. It is recommended to integrate the system onto the vehicle in its current state with the addition of the switching circuit. Integral control can be added to correct steady state error. Additional control logic to switch between power systems should also be added. In addition to these electrical system advancements, thermal management should be taken into account, as the placement of the engine will be internal to the vehicle. Not only must the exhaust be evacuated from the cabin, but the rectifier, power electronics, and remainder of cabin must also be cooled. These topics will be the discussion of the following chapter.

CHAPTER V

FIXED WING VEHICLE INTEGRATION AND TESTING

This chapter will focus on the integration and testing of the turboelectric propulsion and power system into a fixed wing aircraft, the Mugin 4500. The discussion of the physical integration of the system includes fabrication or modification of components including but not limited to: propeller motor standoffs, fabrication of a custom turbine housing, discussion of the switching circuit, and sizing of an inlet and cooling holes. The remaining integration issues are well documented and fairly common among UAS designers, thus will not be discussed in detail. Thermal data from forward looking infrared (FLIR) cameras and thermocouple measurements will be presented, as well as over-arching vehicle level observations; the switching circuit will be evaluated qualitatively. This vehicle will serve as a ground test platform for use in turboelectric prototyping and optimization at the subscale.

5.1 Vehicle Integration: Mugin 4500

The vehicle selected for integration is the New Mugin Plus 4500. The Mugin 4500 is a fixed wing, CTOL platform which features a high aspect ratio wing and A-tail design. On the inside, the Mugin boasts large payload capacity making it ideal for integration of the turboelectric system described in this paper. The Mugin was selected for its large payload accommodations, however ease of procurement and cost also were factors in the selection of this platform. The specifications as given by Mugin are shown in Table 7 below as well as photo of the airframe in Fig. 28 [39].

Table 7. Mugin 4500 vehicle specifications [39]

<i>Specification</i>	<i>Value</i>
Wingspan	4500mm
MTOW	28kg
IAS Range	45-120 km/hr



Figure 28. Mugin 4500 in turboelectric ground test configuration

5.1.1 Propeller Motor Standoffs

In order to obtain as much originality of the test platform as possible, custom made motor standoffs were made. These standoffs were made using SolidWorks to ensure form, fit, and function were met with the vehicle using commercial off the shelf (COTS) standoffs, washers, and fasteners. The SolidWorks assembly is shown in Fig. 29.

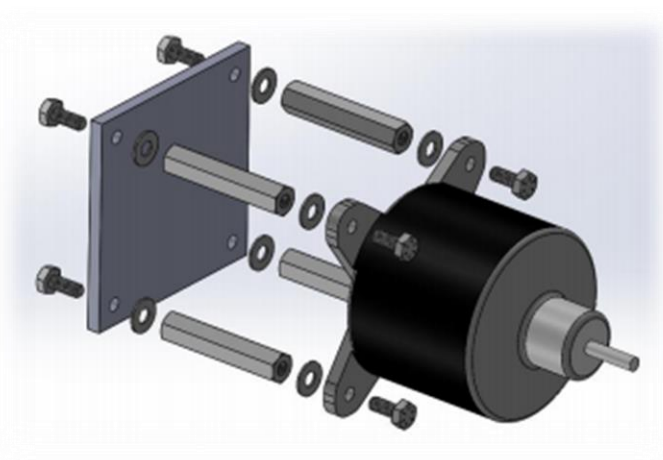


Figure 29. SolidWorks assembly of propeller motor standoff

After validation of the assembly in SolidWorks, the components were ordered and the subassembly was fabricated. An installation check was completed before the subassembly was fully integrated and holes were drilled into the vehicle. This was done so that the electric motor driving the propeller would mesh well with the cowling on the aft of the vehicle, shown on the left in Fig. 30. The electric motor used in this application was the EFlite Power 360 BLDC motor. The EFlite Power 360 has a peak power of 6 kW at 12S (44.4V nominal) and an engine speed rating of 180 RPM/V. This motor was selected as it closely aligns with the power available post-rectification. A steel backer plate was added to help distribute the stress through the airframe and prevent tear-out; this plate serves as a torsional support. This is shown on the left of Fig. 30. It is important to note that all components used are from the same alloy and do not pose a risk of galvanic corrosion over time.



Figure 30. Photo of propeller motor with standoffs, with and without cowling

5.1.2 Turboelectric Power System Housing

The first element of integration was the design and fabrication of a turbine-generator housing. Note that the preliminary turboelectric power system housing is not intended to be a final flight representative housing, but rather intended for use in ground testing as a stepping

stone to a final design. In order to demonstrate the versatility of a single unified turboelectric propulsion and power system, the housing was designed to fit inside the payload bay of the Mugin 4500 as well as mount to the chassis of the xFold Travel 12 dodeca-copter. The single largest constraint designing the custom enclosure was fitting the enclosure within the payload bay of the Mugin while retaining the ability to attach to the unmodified lower chassis for the xFold without changing the center of gravity location. Details of the center of gravity calculation are not discussed in detail, however it was concluded that there would be minimal change in flying configuration and the vehicle would still be trimmable and maneuverable. Upon fabrication, integration was evaluated on the xFold Travel 12 dodeca-copter, and is shown in Appendix A. Given these constraints, the configuration shown in Fig. 31 was selected for the initial design.

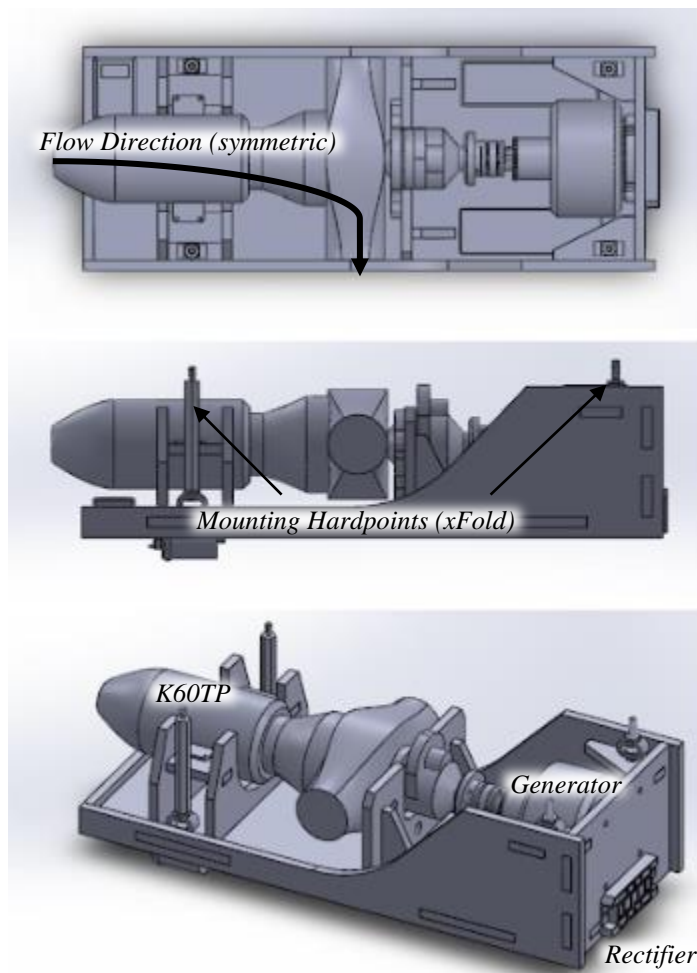


Figure 31. CAD of preliminary turboelectric housing, Rev I

Given the intricate nature of shaft alignment, it was concluded that the optimum fabrication technique would be to laser cut thin aeroply plywood. One major advantage of laser cutting is the ability to maintain very tight tolerances with relatively low material loss allowing for high accuracy with shaft alignment. Each component was measured carefully for hardpoint mounting location and recreated using SolidWorks shown in Fig. 31. Some assistance with geometry was taken from KingTech [1] CAD drawings of the K60TP.

The plywood selected for the fabrication of the enclosure was 1/8th inch birch plywood consisting of three plies. While this is excellent for ground testing, it is not intended to be used in the final flight representative design due to poor fire resistivity. The orientation of the plywood was arranged such that bending loads would be carried primarily in the strongest direction perpendicular to the grain. The first revision of the shelf can be shown in its assembled form in Fig. 32. From prior studies performed at Oklahoma State University of small turbojet powered sUAS, [unpublished] it was found that 1/8th inch birch plywood can easily handle the shear loads generated by a turbojet engine producing thrust on the order of 15 pounds and effectively transmit them through the body of the airframe. Given this result, it is assumed that the plywood will also fare well with the torsional loads generated from rotation with friction. Several other revisions of this platform were made to accommodate lighter manufacturing, cooling requirements, and address fitment issues from previous revisions. These results can be shown in Appendix A.



Figure 32. Prototype turboelectric shelf, initial design

5.1.3 Inlet Sizing

Two major considerations went into sizing the inlet for the turboelectric system: cooling and gas turbine operability. Factors such as operability and structural integrity affect the precise placement of the inlet. For continuity to be satisfied, exit holes must be included to evacuate air from the cabin once it has been used for cooling. In order to size these openings mass flow parameter was used. Mass flow parameter (MFP) is a compressible flow relation shown in Eq. 51, which is used to calculate the area required given a specific target mass flow rate and flight condition. MFP can be derived as a function of only the freestream Mach number and the ratio of specific heats; for the standard atmosphere the ratio of specific heats, γ , is equal to 1.4. The rearranged form of MFP which calculates inflow area required is shown in Eq. 52.

$$MFP = \frac{\dot{m} \sqrt{T_T}}{A P_T} = \sqrt{\frac{\gamma g_c}{R}} M \left(1 + \frac{\gamma - 1}{2} M^2 \right)^{\frac{-(\gamma + 1)}{2(\gamma - 1)}} \quad (51)$$

$$A = \frac{\dot{m}}{MFP(M,\gamma)} \frac{\sqrt{T_T}}{P_T} \quad (52)$$

5.1.3.1 Turbine Operability

Addressing turbine operability, the chief concern is avoiding choking the inlet. Choking the inlet at reduced throttle setting is extremely detrimental to operability, as additional mass flow of air is required when throttling up. Should the inlet be choked, this air is unavailable and the turbine will face major operability issues. These issues could include combustion instabilities, surge and stall, as well as overheating of the turbine. The mass flow rate of air needed to operate the K60TP is not quoted by the manufacturer thus was benchmarked based on engines of a similar rated maximum thrust values; the KingTech designation K60TP implies that the core engine is rated for 60 Newtons of thrust. Figure 33 shows benchmarked data for thrust vs. mass flow rate. It is assumed that the mass flow rate listed in the specifications is corrected to sea level static, standard day [40].

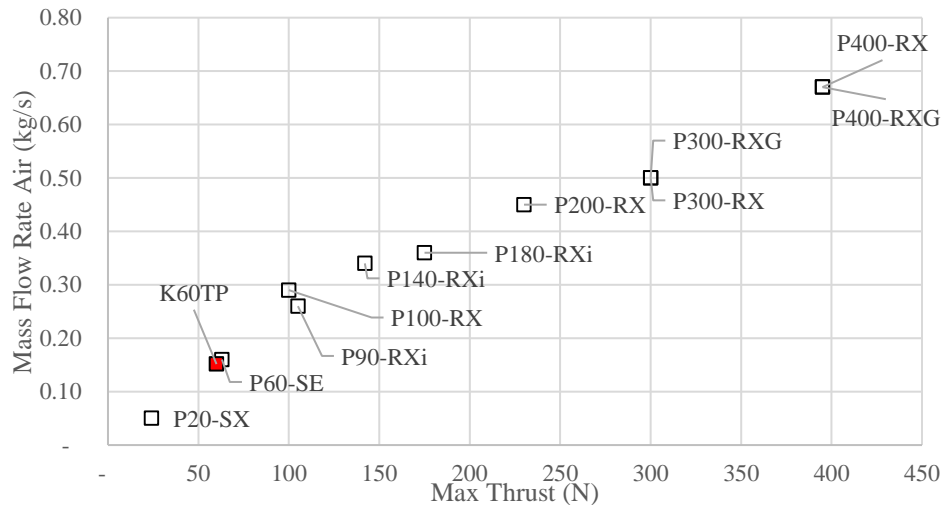


Figure 33. Benchmarking data for mass flow rate vs. rated thrust

Based on the figure the value of mass flow rate selected for the K60TP at peak power (60N), the estimated mass flow rate of air is 0.15 kilogram per second. This converts to 0.33 pounds per second. This value was obtained by linear interpolation between the P20-SX and the P60-SE thrust and mass flow values.

5.1.3.2 Cooling Requirements

To calculate the mass of air needed to cool the cabin some assumptions had to be made about the cooling environment. It was assumed that takeoff was the worst case scenario for cooling, as the turbine (in this application) is sized for takeoff. There are two elements being considered: rectifier cooling and cabin cooling. Beginning with rectifier cooling, the peak current draw was calculated using Ohms Law. Power loss through the rectifier is a function of current and is given by the manufacturer in the datasheet. Using Ohm's Law and manufacturer specifications about the propeller motor, current was estimated to be on the order of 120 amps. Figure 34 shows the manufacturer specifications for peak power loss as a function of current [41]. It is assumed that all power loss from the rectifier is being dissipated as heat.

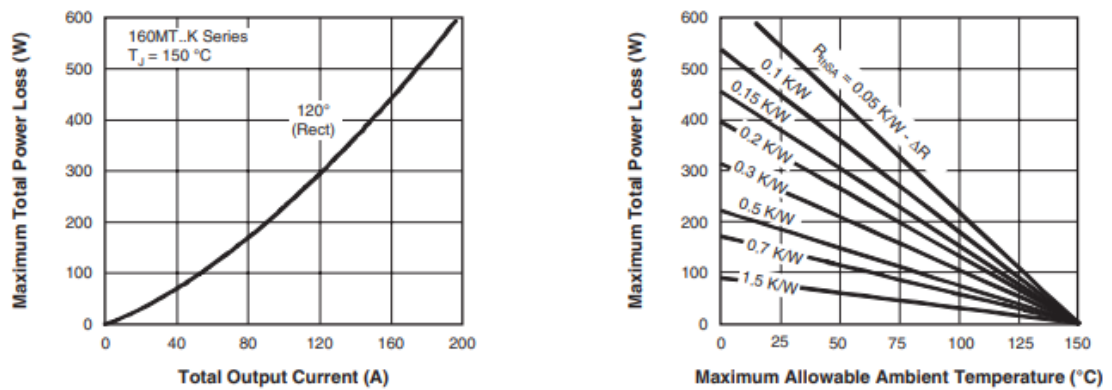


Figure 34. Manufacturer specifications for power loss vs. current (left) and maximum ambient temperature with heat sink vs. power loss (right) [41]

Based on a current of 120A, peak power loss at a junction temperature of 150C is estimated to be 300W. To accommodate hot day considerations (worst case scenario), ambient temperatures less than 50C will not be considered. Given these constraints a heat sink of thermal resistance 0.15 K/W or less must be selected.

Lastly, to ensure the cabin is adequately cooled a thermal analysis was done. In this study, a tradeoff of allowable ambient temperature was iterated on against mass flow rate for a desired cabin temperature. This simplified model takes into consideration the variables given in

Eq. 53, where Q is the heat loss from the turboelectric system due to inefficiencies, c_p is the specific heat of air, and ΔT is the temperature rise of the air. It is important to note that not all of the mass flow rate will be used for cooling, as shown in Eq. 54, where the mass flow rate partitioned for cooling is denoted by subscript c , the turbine by subscript t , and the total by subscript net , respectively.

$$\dot{Q}_{net} = \dot{m}_c c_p \Delta T \quad (53)$$

$$\dot{m}_t + \dot{m}_c = \dot{m}_{net} \quad (54)$$

Given a 70 percent electrical efficiency, it is estimated that of the 7.3 kW available input power, around 30 percent of that will be lost into the cabin as heat. The adiabatic assumption is also being modified to allow for some amount of heat transfer through the casing. Given the uncertainty involved with estimation, it is conservatively assumed that the turboprop will emit heat at 25% proportion relative to peak mechanical power through the casing, bringing estimated heat loss to around 4 kW. Using this as a working number, and limiting the temperature of the cabin to 50C (122F), Fig. 35 was produced. The design constraint of 50C (122F) is indicated by the dashed line on Fig. 35. Both standard day and hot day conditions are shown on the graphic.

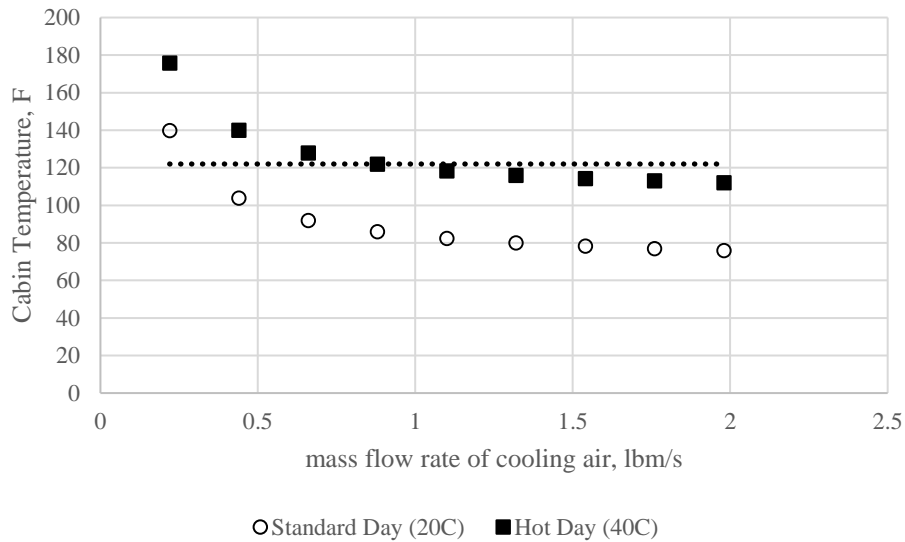


Figure 35. Trade study of mass flow rate of air vs. cabin temperature

The figure above shows the tradeoff between cabin temperature and mass flow rate for a fixed maximum allowable temperature of 50 degrees Celsius. The ambient temperature governs the size of the inlet and outlet holes due to the temperature change. Based on the study and constraints set forth to accommodate a hot day, a mass flow rate of 1 lbm/s is needed at the minimum. If the vehicle were to operate exclusively in cooler climates less airflow would be needed, however the hot day assumption allows for not only versatility but margin given that many of the calculated figures are estimated. For a standard day, only 0.4 lbm/s of cooling air is needed.

5.1.3.3 Inlet Size Calculation

Lastly, to size the inlet the net mass flow rate required based on cooling and turbine operability requirements was determined. Mass flow parameter is a function of the flight Mach number, thus a flight Mach number was estimated based on a manufacturer quoted range of flight speeds. Estimates of area required are given as a function of flight speed and temperature in Fig. 36. Flight speed is directly related to Mach number for a specific atmospheric temperature.

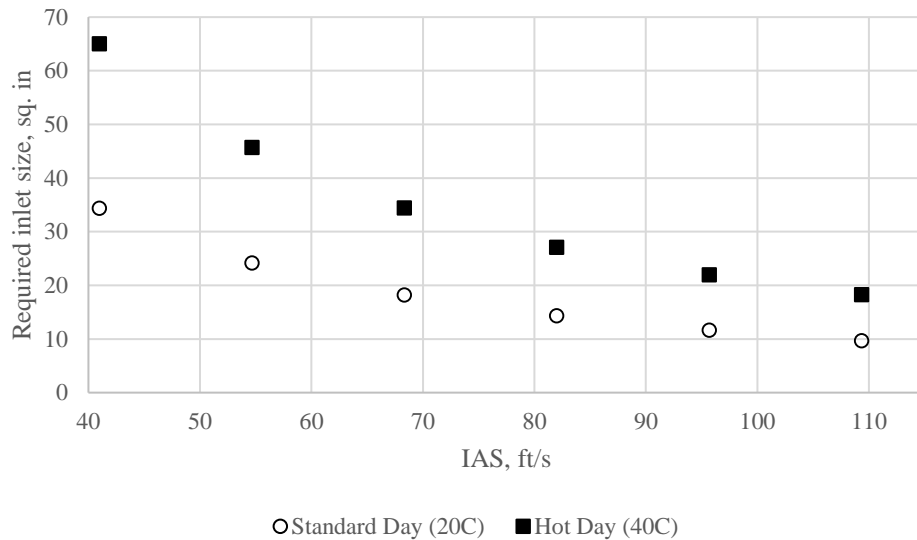


Figure 36. Area required vs airspeed, hot day and standard day estimates

As anticipated, the hot day assumption increases the required inlet area by a factor of nearly two for each point evaluated. Given the airframe size, it does not appear feasible to accommodate hot day (40C) operation at low speeds without compromising structural integrity of the hatch; too much material would have to be removed. Given the high amount of uncertainty due to preliminary estimations it may be possible to operate under the hot day condition, but without actual thermal data this possibility is unknown. The initial inlet size selected which is the best compromise between cooling and structure was determined to be 15.9 square inches; this is equivalent to a circular cross section of 4.5 inch diameter. Recall cooling was calculated based on the full throttle assumption, as this will be the worst case scenario; the minimum indicated airspeed (IAS) required to cool the cabin under steady, full throttle operation on a standard day (20C) is 80 feet per second. If additional cooling is deemed necessary the inlet size can easily be increased, however once the inlet is cut extensive work would be required to reduce the area.

To allow cooling air to evacuate the cabin, Eq. 55 was used. This equation is based on continuity with several assumptions tied to the calculation, which include incompressible air and minimal changes to the cooling air velocity.

$$A_{exit} = A_{inlet} \left(\frac{\dot{m}_c}{\dot{m}_{net}} \right) \quad (55)$$

Using this equation, the required exit size is 8.7 square inches, which will be divided over two holes of diameter 2.375 inches. This was done to minimize interference of the cooling holes with the motor mounting structure. A SolidWorks snip of the inlet and exit holes are shown in Fig. 37.

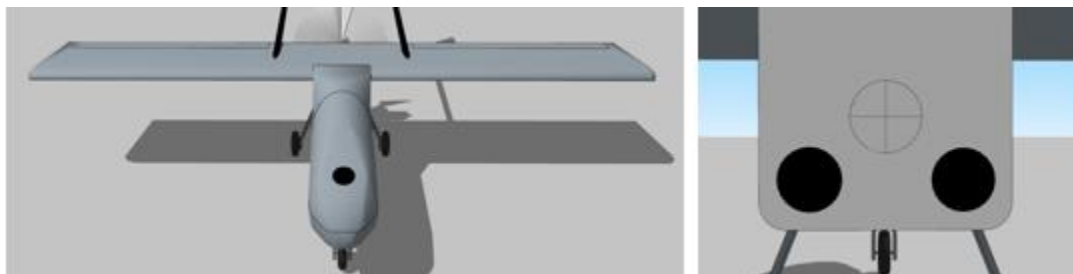


Figure 37. Approximate scale of inlet and exit holes for intake and exhaust air

5.1.4 Completed Integration

The vehicle integration consisted not only of the steps shown above but included multiple iterations of other tasks required to get the vehicle into a testable state. These revisions include but were not limited to: the placement of various components into the cabin, modification of the airframe to evacuate gas turbine exhaust, installation of a battery and electronics shelf, and mounting of the turbine engine shelf to the airframe. These topics will be discussed in detail in the following sections.

5.1.4.1 Component Placement

For the placement of components into the cabin there were many considerations that must be taken into account. The highest weighted consideration was overall vehicle static stability. If the aircraft is not statically stable, ballasts would have to be added to ensure stability criteria are met; this addition of dead-weight would be detrimental to range and endurance. The figure of merit used to denote static stability along the longitudinal axis is known as static margin and is denoted by S.M.. The equation for static margin is shown below in Eq. 56, but physically can be interpreted as the difference in center of lift and the center of gravity of the vehicle, normalized by the mean chord of the wing. For a vehicle to demonstrate static stability in flight, the center of gravity should be ahead of the center of lift. For fixed wing aircraft of this scale, S.M. values of between three and ten percent are desired.

$$S.M. = \frac{(x_{cg} - x_{cl})}{c} \quad (56)$$

To ensure that the objective of safe ground testing is attainable, several requirements were set. These requirements were placed at the level desired for a flightworthy vehicle, however there is room for relaxation should it be needed. They are as follows:

1. Hot gases from the exhaust of the turbine engine should be evacuated from the cabin via exhaust ducting. The exhaust pipes of the turbine engine should be sufficiently far away from all electronic components and fuel lines and not directly impinge on the airframe.

2. Electronic components including batteries should be isolated from fuel tanks, valves, and lines.
3. The shelf of which the K60TP is mounted to should incorporate vibration dampeners between the shelf and the airframe.
4. Wiring should be kept clear of hot components and rotational components.
5. The rectifier and heat sink should be placed in the path of the cooling flow and not obstructed by any piece of hardware.
6. The fuel tank should be placed aft of the center of lift of the aircraft. This occurs at approx. 0.25 chord from the leading edge of the wing. This allows stability to improve as the flight duration continues.
7. General airworthiness requirements for UAS must be met per CRF 14 Part 107.

Several designs were considered for the internal layout of the aircraft, however only the selected design is discussed in detail. After careful consideration the configuration pictured below in Fig. 38 was selected. Figure 38 shows the placement of hardware components used in the integration and installation of the turboelectric system in the aircraft, while the numbered components are identified in Table 8. The fuel tank was placed below the battery and electronics shelf to avoid fuel leaking on the batteries; it is also located just aft of the center of lift of the aircraft allowing stability to increase as the mission goes on. The largest fraction of deadweight including the turbine, generator, and turbine electronics is placed ahead of the center of lift, while the batteries are used as a ballast in the rear. This drives the c.g. of the aircraft to around 35 inches. Given an estimated center of lift at 36 inches, and a mean chord of 15 inches, the static margin falls out at approximately 6 percent. This is well within the bounds specified for an unmanned aircraft of this scale.

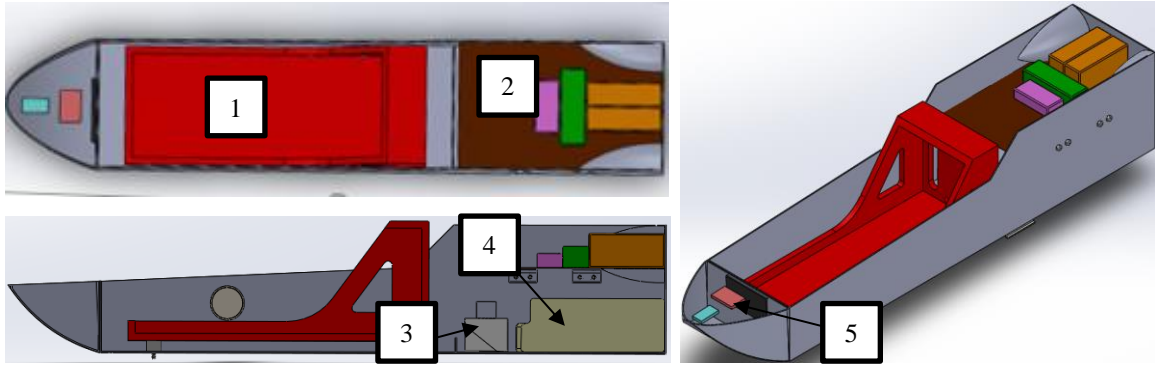


Figure 38. Layout of internals, Mugin 4500 airframe

Table 8. List of major components for Mugin 4500 turboelectric integration

<i>Component</i>	<i>Number</i>
Turboelectric Power System Housing	1
Battery and Electronics Shelf	2
Rectifier and Heat Sink	3
Fuel Tank	4
Avionics Bay and Turbine Electronics	5

Both the turbine shelf and battery and electronics shelf will hold multiple subsystem components, including a fuel pump, ECU, switching circuit, as well as several batteries. Airworthiness requires the radio receiver and onboard autopilot to have a power source isolated from the propulsion system batteries. Given this requirement, several different types of batteries are required to ensure the vehicle can operate and comply with airworthy standards. The placement of these batteries can be shown in Fig. 39 and the function of each battery is given in Table 9.

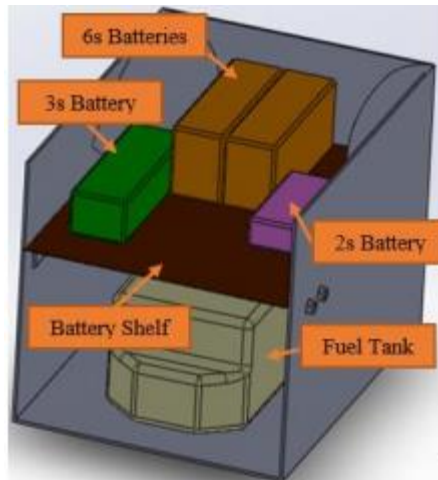


Figure 39. Section view of the rear compartment of the Mugin 4500

Table 9. List of batteries used and function

<i>Type</i>	<i>Function</i>
2s LiFe, 2100mAh	Futaba Receiver and Arduino
3s LiFe, 3800mAh	KingTech ECU and Fuel Pump
6s LiPo, 5500mAh (2x in Series)	Propulsion System

Upon arrival and physical installation of the components, it was determined that the rectifier would fit in a more direct path relative to the inflow cooling air. The rectifier was moved from the position shown in Fig. 38 to the position shown in Fig. 40, being placed directly above the BLDC generator and forward of the battery and electronics shelf. This simple modification allows for not only additional cooling air, but for a more modular design as the rectifier and heatsink are directly connected to the turbine shelf. In addition to this modification to the rectifier placement, several additional revisions are required for the electrical system.



Figure 40: Integrated turboelectric system showing the updated rectifier location

5.2 Electrical System Revisions

Several revisions must be made to the electrical system of the vehicle to accommodate airworthiness and safety requirements should a flight test be considered. The details of these revisions are not discussed in great detail for aforementioned reasons regarding sensitive information, but in summary a battery backup and switching circuit must be added. This is done to ensure that should the turboelectric system fail during operation there is an auxiliary power system onboard, allowing the pilot to land the vehicle safely. Due to the nature of this system, additional logic must be included in the throttle controller.

5.2.1 Battery Backup

A backup battery must be included in the turboelectric power system to ensure airworthiness requirements are met for future variants of the system. The inclusion of a battery will allow the system to continue to operate safely should the turbine fail or be switched off for quiet operation. The battery should be sized accordingly to comply with system requirements,

such as number of cells (related to voltage), charge/discharge rates (related to bi-directional current), and capacity (related to energy storage). Capacity is one of the most important factors, as this will ultimately limit time of flight in the event of an emergency landing or quiet operation. For example, if the system requires 50 Amps, and the battery capacity is 5000 mAh, the respective maximum time of flight on battery power is around 6 minutes from the time the turbine is disengaged. Other factors affected the decision such as availability and budget. The batteries selected for this application were two Gens ACE 6S 5500mAh lithium-polymer batteries placed in parallel. This gives 5500 total milliamp-hours of capacity at 12S (44.4V nominally). The switching circuit described in the next section enables switching between a purely battery driven system and hybrid power system; this revision of the switching circuit does not include supplemental power from the battery during hybrid operation.

5.2.2 Design of Switching Circuit

To accommodate multiple power sources and enable power system redundancy in case of failure, a switching circuit was designed. For switches, MOSFET transistors were selected; MOSFETs are excellent at switching quickly and are voltage activated. Unlike IGBT's or mechanical relays which are current activated, MOSFETs do not consume power on activation. The MOSFETs used in this application are triggered from the throttle controller. In the preliminary design of the switching circuit, source voltages and currents greatly affected the selection of parts. Current also limited the amount of semi-conductive components available for selection; continuous current on the order 50 to 100 amps makes many common parts undersized for this application. The MOSFET selected is able to meet requirements for both the voltage and continuous current and has the specifications listed below in Table 10.

Table 10. Specifications of driver and switching MOSFETs in switching circuit

Parameter Name:	SUP50020EL-GE3 NMOS Transistor
Max Drain-Source Voltage	60V
Max Gate-Source Voltage	$\pm 20V$
Gate Threshold Voltage	1.2V - 2.5V
Max On-State Drain Current	120A

In addition to the switching capabilities, the circuit also has been outfitted with hardware to accommodate battery charging capabilities as discussed in the previous sections. A smoothing circuit was added to help smooth any transient signals in system and also to provide power during dead-bands from switching. Given the high speed of the switches, only a few milliseconds of instantaneous energy are needed. This estimation of switching time drives the size of switching components. A boost or buck converter may be needed depending on the electrical load, making the switching circuit vehicle specific. A buck converter was considered for this application as information from the model showed higher efficiencies at higher voltages, however it was deemed unnecessary and the circuit design moved forward without implementation. It is important to note that given the high number of components associated with this circuit, each functional component will be evaluated individually. Specifically, the switching component of the circuit will be evaluated first and built up by adding the charging circuit, followed by the smoothing circuit and voltage converters (as needed), respectively.

5.2.3 Throttle Controller Revisions

Logic must be added to the controller to enable switching. For preliminary testing of the switching circuit, the throttle controller will read in a pilot command commanding when to switch power sources; future versions of the controller can easily automate this process based on a variety of safety and operability variables. Though this system is intended to control the 7.3kW turboelectric system described in the previous sections, this control architecture in general scales

to accommodate any size fixed wing turboelectric platform assuming the parts are sized accordingly for the expected current and voltage.

5.3 Design of Experiment III: Fixed Wing Integration Proof of Concept

In order to evaluate the integration of the turboelectric power system aboard fixed-wing sUAS, the following experiment was designed. The test article is shown in Fig. 41 below. The independent variables being evaluated are as follows:

- 1) Test and evaluate the function of the new throttle control logic and the successful operation of the switching circuit.
- 2) Evaluate gas turbine operability and cooling area allocations; evaluate the placement of the exhaust ducts in the critical operational case.
- 3) Evaluate the overall vehicle integration and report vehicle and component level considerations.

The critical case for hot gas impingement and high cabin temperatures was determined to be a very specific portion of the takeoff leg: the vehicle is on the ground, turbine set to takeoff throttle, zero forward velocity, with the propeller spinning at takeoff (max) thrust. A propeller advance ratio of zero was desired to truly simulate this leg of takeoff, therefore the vehicle is anchored to the ground in an area shielded from the wind as shown in Fig. 41. The propeller used in this experiment is an Engel three bladed 20 inch diameter by 12 inch pitch. In the scenario described above, there will be no ram air into the cabin to aide with forced convection, thus the cabin will have to be cooled by only natural convection and forced air from the turbine. The exhaust also evacuates the cabin at a 45-degree angle, oriented aft and down; this is the only case in which reflections off the ground can occur and potentially impinge on the wing.



Figure 41. Photo of the Mugin 4500 test article, integrated with turboelectric propulsion and power system

To begin the experiment, the pilot will indicate to the throttle controller to power on the turbine. The turbine will go through its automatic start sequence before the controller is given authority, digitally controlling the engine to operate the turbine. For this experiment, proportion control is sufficient as only the steady state temperature at max thrust is being evaluated. The power being supplied to the propeller is in the range of 3.7-3.8kW, which corresponds to approximately 75 Amps of current being supplied at 51 Volts. This is the peak power of the propeller at this combination of rotational speed and altitude. It is important to note that by changing the propeller, freestream velocity, or altitude the takeoff thrust and power would change and consequently the thermal signature of the system would change. The system temperatures will be monitored by use of a forward-looking infrared (FLIR) camera for a duration of at least sixty seconds to ensure the system has reached thermal equilibrium and no additional transient heating effects are present. The FLIR camera used is a FLIR BCAM SD, which has a range from -10 to 100C, a resolution at 10 ft of plus and minus 2% of the range, and a 0.1 degrees (Celsius) sensitivity at 25C. The FLIR camera will reveal component temperatures as well as local hotspots.

A thermocouple outfitted in the cabin will also yield important results about the cabin temperature. Placement of the thermocouple was determined based on an estimated worst case scenario location; the thermocouple was placed directly below the exhaust manifold of the turbine

engine protruding from the turbine shelf, with approximately 1.5 inches of air gap between the exhaust manifold and the thermocouple head. A photo outlining the placement of the thermocouple into the turbine shelf can be shown in Fig. 42. The thermocouple selected for this was a K-type thermocouple, which had a temperature range of 0°C-1024°C.



Figure 42. Photo of K-Type thermocouple location relative to turbine exhaust

From this experiment, conclusions regarding the placement of the exhaust pipes, internal components, and cooling area allocations will be answered. This test will also answer a valuable question about operability of the system in a hot confined space. Rectifier cooling is not anticipated to be an issue at this power setting given the selected heat sink, thus rectifier heat sink temperatures are not measured. If the current to the load were to increase by either means of changing the propeller or the number of propulsors, the assumption that sufficient cooling flow is reaching the rectifier must be re-evaluated.

5.4 Results III: Fixed Wing Integration and Switching Circuit Evaluation

The results of the study are discussed in the following sections. Results of interest include FLIR thermal imaging of the vehicle and surroundings, the cabin temperature and an overall

assessment and recommendation for the switching circuit. These results will indicate key considerations to assess when configuring aircraft internal layouts of new prototype turboelectric power sUAS.

5.4.1 FLIR Thermal Imaging Results

As stated above, the critical case for hot gas impingement is expected to be in takeoff configuration. Shown below in Fig. 43 are thermal images taken during a simulated takeoff roll. The ambient temperature on this day was 1 degree Celsius. In order to capture these images, the thermal camera was positioned and aimed at the aircraft and monitored until the observable temperature change was negligible. Once the temperature change ceased, the images shown in Fig. 43 were captured revealing where the local hotspots occur. Notice from the left image, that some amount of reflection does occur off the ground, which manifests itself as a temperature increase of approximately 30C on the leading edge of the wing relative to ambient. This is not an issue given the ambient temperature of 1 degree Celsius, however should the test be conducted with hot day conditions, test time should be limited. It is also observed that the landing gear mounts heat up a significant amount increasing by nearly 50C; these mounts do slightly protrude into the flow thus this result was expected. From the image on the right, the physical landing gear of the aircraft is safe from heat impingement. Observation of the exterior temperature of the hatch shown on the left image of Fig. 43 threw a red flag, increasing by 40C. This section of the cabin which contains the turbine engine does heat up substantially more than anticipated, indicating that additional cabin cooling is necessary. While the cabin temperature is not an issue at this temperature, test time should be limited should the test be conducted under hot day conditions as these results are subject to ambient temperature.

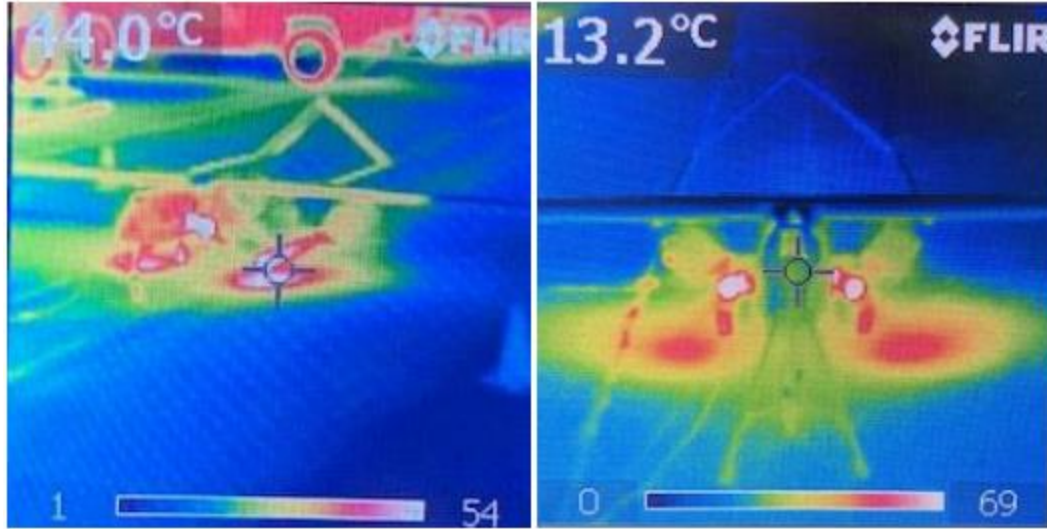


Figure 43. FLIR thermal imaging of the Mugin 4500 operating at max thrust

5.4.2 Cabin Temperature Readings

During the process of testing, the thermocouple mounted to the engine shelf failed. This unexpected failure of equipment led to the use of the OMEGA HH509 digital handheld thermocouple reader and K-type thermocouple. This equipment was brought to the test site as a backup and was calibrated within the range of the FLIR camera. The OMEGA HH509 has an accuracy of $\pm 0.1\% + 1\text{C}$, and a range of -210C to 1716C . The thermocouple which failed was being read by a thermocouple chip compatible with the throttle controller, thus digital data logging was available; this option was not available with the OMEGA thermocouple reader. To accommodate the approved test procedure, the thermocouple was placed in the same location and monitored until the temperature reached a steady state reading. For an ambient temperature of 1 degree Celsius, a cabin temperature of 66 degrees Celsius was measured, equating to a 65 degree Celsius (Kelvin) increase in cabin temperature in the simulated takeoff. Given that this was the worst-case scenario for heating, it appears that the system passes initial inspection. However, upon further consideration of the hot day condition, this same temperature increase would be disastrous for all semi-conductive components and circuit cards not equipped with heatsinks. This result solidifies the need to increase the amount of cooling flow to the cabin of the vehicle. This

would be done by increasing the size of the inlet and exit holes proportionally to accommodate the higher mass flow rate. Heat sinks should also be added to semiconductive components not currently outfitted with a heat sink.

5.4.3 Switching Circuit Assessment/Troubleshooting

During the testing phase of the system, the switching circuit was evaluated for successful operation and switching under the no load condition. The switching circuit was intended to be evaluated with all components, including the charging and smoothing circuits however issues arose with switches failing during steady operation. Switching is the primary function of the circuit, thus these additional components were removed to isolate the switching component. Initially, the circuit was evaluated under no load, with the hybrid power system spooled to 47 volts; this corresponded to approximately 30% turbine power under no electrical load. The control logic and switching function operated as expected in response to the pilot command, switching both directions. The turbine throttle was reduced to idle and the MOSFETs opened and closed as expected when switching from hybrid to battery power. Similarly, the throttle increased to yield the stable operating point of 47V out, and the MOSFETs switched accordingly when going the other way. This result indicated that software was likely not the culprit. As the electrical load was brought up to full throttle, it was observed that the components would fail over a short duration. This indicates that the current was very likely the cause of failure. Current failure most often refers to issues with overheating components. The components were not sinking heat into anything directly but were relying on convective cooling over the back plate of the built in heat sink. This is likely due to shorting of the MOSFET from a physical failure occurring as a product of overheating. This current, 75A, is at the top end of the MOSFET operating range. This information drives the solution toward heavier duty switches for the future iterations, regardless of additional cooling or heat sinks.

5.5 Conclusions, Observations, and Recommendations III: Fixed Wing Vehicle Integration

Results of the integration phase of testing yielded valuable knowledge that will be used to design future variants of the turboelectric power system. In relation to Research Question II, [which states: What are the vehicle level design considerations when designing a vehicle utilizing a hybrid turboelectric powertrain?] one of the largest vehicle level considerations is the cooling flow allocation for thermal management. Beginning with thermal management of the exhaust gas, it was determined that for the static case in the current configuration hot gas impingement does not appear to be an issue for either the wing or the landing gears. Should the takeoff weight, propeller, or number of electric propulsors change, the thermal signature will change as a result due to the change in mechanical power required. The cabin temperature does pose slight concerns when the hot day consideration is imposed, thus the recommended suggestion is to increase the size of the inlet and exit holes to accommodate a higher mass flow rate of air. On important consideration when doing this is the overall structure of the aircraft, as the exit holes are located very near the mounting plates for the rear propulsor and the inlet holes are cut into a hatch made of thin fiberglass. Uncovering and addressing these concerns with integration successfully satisfies Objective II, which states:

Objective II: Determine vehicle-level challenges and constraints associated with integration and installation of the turboelectric system aboard a fixed-wing aircraft and mitigate/address them.

Given the low operational temperature of semi-conductive devices as well as microcomputers, ambient temperature greatly affects the size of the cooling passages. In order to not compromise the integrity of the vehicle, forced cooling by means of auxiliary cooling fans mounted on the interior of the vehicle may be considered. If auxiliary cooling is not implemented, then additional cooling area should be added. In order to mitigate the structural concerns expressed above, additional cooling passages of lower area could be placed in various locations around the airframe, alleviating large stress concentrations. Ports on the underside of the

vehicle should be excluded as this poses a reliability issue with FOD ingestion. Overall, integration of this system yielded valuable information about the system and vehicle level considerations for future vehicles.

In relation to Research Question III, [which states: Is a turboelectric sUAS a feasible alternative to purely electric sUAS?] the modifications made to the stock airframe to accommodate the turboelectric power system were minimal. The turboelectric system functioned as anticipated; however, it does need a few minor revisions to reach a level of robustness on par with that of a purely electrically driven propulsion system. The minimal amount of modifications required to the vehicle plus the functionality demonstrated by the system in this phase of testing suggest that turboelectric systems can be used as an alternative to purely electric propulsion systems in terms of operability of the electric load, satisfying Objective III. Recall, Objective III states:

Objective III: Demonstrate feasibility of turboelectric propulsion and power as an alternative to all electric systems in terms of operability.

Several minor changes are required before the system is at a flightworthy state. Heavier duty switches should be used in place of MOSFET type switches. Once the switching circuit has been updated to accommodate heavier duty components, a smoothing circuit must be incorporated. This will help to ensure that the signal out of the switching circuit is closely representative of a DC signal. This can also add some degree of damping to the system allowing the regulated voltage output to be less susceptible to perturbations in loading. Lastly, additional tuning of the throttle controller is necessary to improve the response to perturbations as discussed in Chapter IV. With all of these revisions made, the turboelectric system will reach a state in which it is deemed a feasible alternative to a purely electrically driven system not only in terms of operability, but also in terms of reliability.

CHAPTER VI

CONCLUSIONS, RECOMMENDATIONS, AND OUTCOMES

This paper evaluates the feasibility of turboelectric propulsion and power for a sUAS based on three research questions which will satisfy three objectives; the research questions are given below:

1. What are the system level design considerations when designing a hybrid turboelectric powertrain?
2. What are the vehicle level design considerations when designing a vehicle utilizing a hybrid turboelectric powertrain?
3. Is a turboelectric UAS a feasible alternative to purely electric sUAS?

In response to Research Question I. The results of the first phase of testing and modeling yielded positive results. The analytical model developed to calculate electrical efficiency as a function of system operating condition and component level parameters was tested and validated across an operating range and showed high correlation and accuracy across this range. The validation of this model proves its effectiveness for use as a design tool when designing a turboelectric powertrain. This model yields important information about the selection of components, especially the generator and range of electrical loads which are compatible for the turboelectric system. The relationship between stage loading, gear ratio, current, and speed rating of the motor yield vital information about the low pressure turbine. If the operating map of the low pressure turbine is known, then the model developed in Eq. 46 can be used to size the generator, as all parameters except current draw are directly chosen by selection of a generator. This is a powerful relationship as the scale of the system increases and turbine performance

begins to increase. Ultimately, the development of this model successfully answers Research Question I, and satisfies Objective I, which states:

Objective I: Develop and evaluate a design tool which focuses on the efficiency and operability of a turboelectric system which also addresses compatibility of the components of the power generation system including the turbine, generator, and rectifier.

The first phase of testing also demonstrated the need for active throttle control, as the turbine exhibited oscillatory behavior when coupled to the electric generator and load. Active throttle control is still under development and will likely include both integral and derivative control in addition to the standard proportion control. The results of the second phase of testing showed the need for signal conditioning and electrical system damping. The damping ratio tabulated showed the system with the throttle controller was highly underdamped, and in need of signal conditioning, as high frequency noise was observed in the steady state response. Electrical loads which are sensitive to voltage (such as high speed motors) will experience oscillatory behavior as well if the signal is not conditioned. The addition of a smoothing circuit will effectively assist with both of these issues. Careful thought should go into sizing of the components, as overcharging can be catastrophic given the high amount of electrical energy. Based on all education and information acquired throughout the duration of this experiment, the recommendations moving forward with respect to Research Question I and Objective I are as follows:

- a) The optimum electrical load arrangement as per the model developed in Eq. 43 for turboelectric drivetrain is that of a high voltage and low current, respectively.
- b) Based on Eq. 46, the generator speed rating should be kept as low as possible but not so low as to exceed the max stage loading of the LPT. Relating this to Eq. 43, if the speed rating of the generator is low, this indicates the shaft speed is low (by comparison) and consequently friction is low (by comparison).

- c) Based on the damping ratio, sluggish response time of the turbine, and high frequency noise in the signal, a smoothing circuit should be added to the system post rectification. The addition of this circuit will not only smooth the signal and enable digital rate control, but can potentially add electrical damping to the system by increasing the time constant. This component is necessary for loads which are sensitive to voltage.

In relation to Research Question II, many insightful results came out of the integration of the turboelectric system onboard the Mugin 4500 airframe. Results of the integration phase of testing yielded valuable insight into vehicle level design choices to accommodate the propulsion and power system. In addition to standard integration concerns (static margin, FOD, leak containment, airworthiness requirements, etc.) and modifications to accommodate fitment of COTS components (standoffs, spacers, etc.), an additional consideration is the layout and modification of the airframe for thermal management. This includes not only allocation of adequate cooling flow, but also cooling of electronic components and evacuation of exhaust gas. Given the low operational temperature of semi-conductive devices as well as microcomputers, ambient temperature greatly affects the size of the cooling passages. Though still manageable at this scale the cabin temperature does pose concerns for the operability of the vehicle in select regions, specifically, regions which have a high annual temperature. This problem can be mitigated by additional cooling flow through the cabin, however this leads to removal of additional structure, as well as increased vehicle drag and limitations on speed. One of the most important considerations when weighing these options is the impact these modifications have on the vehicle's structural integrity. Auxiliary cooling is also an option worth considering should the impact be too great. In addition to cabin temperature, evacuation of the exhaust gas is also highly dependent on the airframe. Though it was not an issue in the current high-wing airframe in the current configuration, hot gas impingement from the exhaust plume on the airframe does factor heavily into component placement. For example, a low-wing aircraft would very likely drive a design that evacuates exhaust gas in a different manner than those discussed in this document to

avoid impingement on the wing. Successful integration of the turboelectric power system onboard the Mugin 4500 aircraft and discussion of these considerations successfully answers Research Question II and satisfies Objective II, which states:

Objective II: Determine vehicle-level challenges and constraints associated with integration and installation of the turboelectric system aboard a fixed-wing aircraft and mitigate/address them.

Based on all of the education acquired during integration and testing of the turboelectric power system in the Mugin 4500 airframe, the following recommendations emerge in relation to Research Question II and Objective II:

- a) The inlet and exit hole(s) should be cut larger to accommodate operation at elevated temperatures.
- b) Under the current electrical load, sufficient cooling should be attained with the completion of recommendation a), however should the electrical load be increased it is recommended to augment cooling with the addition of auxiliary cooling fans on electronic components. These components (though necessary) are the most sensitive to temperature, thus they limit the operating environment.

In relation to Research Question III, many observations about the feasibility of turboelectric propulsion and power for sUAS were made throughout the duration of this project related to operability. There are several key components which enable seamless operation of the turboelectric propulsion and power system; the most important element of electrical system operability is active power management via the switching circuit and active throttle controller. Though not physically completed in this study or discussed in great detail, the smoothing circuit plays a large part in operability from the perspective of the load. Switching between power sources is enabled by logic written into the active throttle controller to trigger switches used in the switching circuit. In this study a switching circuit was designed, fabricated, and evaluated in conjunction with the active throttle controller and was shown to perform its anticipated function

of toggling between power sources under load. The active throttle controller enables not only switching, but also power regulation and starting and stopping of the turbine. The ability of the turbine to regulate voltage was shown to be stable, however overshoots and signs of underdamping occurred; both of these issues can be mitigated by the addition of a smoothing circuit. The smoothing circuit will also allow loads that are more sensitive to voltage fluctuations to function with a higher degree of reliability. With the voltage ripple smoothed out, the system will function similarly to a battery from the electrical load perspective. Given the functionality of this system, turboelectric propulsion and power does appear to be a feasible alternative to a purely electrically driven system in terms of operability. This deliverable successfully answers Research Question III and satisfies Objective III, which states:

Objective III: Demonstrate feasibility of turboelectric propulsion and power as an alternative to all electric systems in terms of operability.

The feasibility in terms of range and endurance has not yet been quantified and is the topic of a future study. Given all of the education and knowledge acquired during design, implementation, and evaluation of the system, the following recommendations are suggested moving forward:

- a) A smoothing circuit should be added to the system prior to any additional tuning of the throttle controller. Addition of this circuitry will add damping to the system and potentially mitigate overshoots in the response. The circuit will also ensure that the voltage to the load is as close to a DC signal as possible and help mitigate “surging” of the electric propulsors.
- b) The switching circuit should be reconstructed utilizing heavier duty switching devices. During testing, the large majority of failures with the switching circuit occurred at high power settings, however the architecture was proven to work as anticipated at low power settings. Rather than using simple voltage activated switches such as MOSFET switches, it is recommended to use heavier duty switches. It is also recommended to automate the switching circuit logic such that switching will occur if a condition is met. This condition

could be as simple as monitoring the temperature of a component for overheating (such as the rectifier) or as complex as switching to battery once a geofence is crossed.

- c) With the addition of the smoothing circuit, the throttle controller should be tuned to minimize overshoot and approach a damping ratio of 0.7.

In conclusion, the turboelectric propulsion and power system evaluated in this study does show initial promise as a means of hybrid power for sUAS. Though no definitive conclusion has been reached regarding the range and endurance benefit of turboelectric power on group two sUAS, it has been shown feasible as an alternative to purely electrically driven systems. Though this technology is still under development, the models developed and results obtained in this study will pave the way to a unified turboelectric propulsion and power system in the near future.

REFERENCES

- [1] Zen Cart™ Team. “K60TP.”, www.kingtechturbines.com/products/index.php?main_page=-product_info&products_id=3.
- [2] GrabCad. “Rotomax 100cc render.”, <https://grabcad.com/library/turnigy-rotomax-100cc-size-brushless-outrunner-motor-167kv-1>
- [3] “U.S. Energy Information Administration - EIA - Independent Statistics and Analysis.” What Is U.S. Electricity Generation by Energy Source? - FAQ - U.S. Energy Information Administration (EIA), www.eia.gov/tools/faqs/faq.php?id=427&t=3.
- [4] “PIPELINE 101.” Pipeline101, pipeline101.org/Where-Are-Pipelines-Located
- [5] Marchese, Anthony J., and Dan Zimmerle. “The U.S. Natural Gas Industry Is Leaking Way More Methane than Previously Thought.” PBS, Public Broadcasting Service, 4 July 2018, www.pbs.org/newshour/science/the-u-s-natural-gas-industry-is-leaking-way-more-methane-than-previously-thought.
- [6] Office of Pipeline Safety.” PHMSA, www.phmsa.dot.gov/about-phmsa/offices/office-pipeline-safety.
- [7] Brelje, B., and Martins, J.,. “Electric, Hybrid, and Turboelectric Fixed-Wing Aircraft: A Review of Concepts, Models, and Design Approaches.” Progress in Aerospace Sciences, vol. 104, January 2019, pp. 1-19. DOI 10.1016/j.paerosci.2018.06.004

- [8] Thippavong, D., Apaza, R., Barmore, B., Battiste, V., Burian, B., Dao Q., Feary, M., Go, S., Goodrich, K., Homola, J., Idris, H., Kopardekar, P., Lachter, J., Neogi, N., Ng, H., Oseguera-Lohr, R., Patterson, M., Verma, S., “Urban Air Mobility Airspace Integration Concepts and Considerations” 2018 Aviation Technology, Integration, and Operations Conference, Atlanta GA. 25-29 June. AIAA 2018-3676 DOI <https://doi.org/10.2514/6.2018-3676>
- [9] Johnson, W., Silva, C., and Solis, E., “Concept Vehicles for VTOL Air Taxi Operations,” AHS Technical Conference on Aeromechanics Design for Transformative Vertical Flight, San Fransisco, CA, 16-19 January 2018.
- [10] J. Felder, H. Kim, and G. Brown, “Turboelectric Distributed Propulsion Engine Cycle Analysis for Hybrid-Wing-Body Aircraft,” AIAA 2009-1132, 47th AIAA Aerospace Sciences Meeting, Orlando, FL, 5-8 January 2009.
- [11] Welstead, J., and Felder, J. L., “Conceptual Design of a Single-Aisle Turboelectric Commercial Transport with Fuselage Boundary Layer Ingestion,” AIAA 2016-1027, 54th AIAA Aerospace Sciences Meeting, 2016.
- [12] Jansen, R., Bowman, C., Jankovsky, A., Dyson, R., and Felder, J., “Overview of NASA Electrified Aircraft Propulsion (EAP) Research for Large Subsonic Transports,” AIAA 20174701, 53rd AIAA/SAE/ASEE Joint Propulsion Conference, 2017.
- [13] Jansen, R., Bowman, C., and Jankovsky, A., “Sizing Power Components of an Electrically Driven Tail Cone Thruster and a Range Extender,” AIAA 2016-3766, 16th AIAA Aviation Technology, Integration, and Operations Conference, 2016.
- [14] Vratny, P. C., and Hornung, M., “Sizing Considerations of an Electric Ducted Fan for Hybrid Energy Aircraft,” Transportation Research Procedia, vol. 29, 2018, pp. 410– 426. DOI 10.1016/j.trpro.2018.02.037

- [15] Kirner, R., Raffaelli, L., Rolt, A., Laskaridis, P., Doulgeris, G., and Singh, R., “An assessment of distributed propulsion: Advanced propulsion system architectures for conventional aircraft configurations,” *Aerospace Science and Technology*, vol. 46, 2015, pp. 42–50. DOI 10.1016/j.ast.2015.06.022
- [16] Kirner, R., Raffaelli, L., Rolt, A., Laskaridis, P., Doulgeris, G., and Singh, R., “An assessment of distributed propulsion: Part B – Advanced propulsion system architectures for blended wing body aircraft configurations,” *Aerospace Science and Technology*, vol. 50, 2016, pp. 212–219. DOI 10.1016/j.ast.2015.12.020
- [17] Liu, C., Doulgeris, G., Laskaridis, P., and Singh, R., “Thermal cycle analysis of turboelectric distributed propulsion system with boundary layer ingestion,” *Aerospace Science and Technology*, vol. 27, 2013, pp. 163–170. DOI 10.1016/j.ast.2012.08.003
- [18] Donato, T., Spedicato, L., and Placentino, D. P., “Design and performance evaluation of a hybrid electric power system for multicopters,” *Energy Procedia*, vol. 126, Sep. 2017, pp. 1035–1042. DOI 10.1016/j.egypro.2017.08.310
- [19] Jaeger, M., and Adair, D., “Conceptual design of a high-endurance hybrid electric unmanned aerial vehicle,” *Materials Today: Proceedings*, vol. 4, 2017, pp. 4458–4468. DOI 10.1016/j.matpr.2017.04.018
- [20] Sliwinski, J., Gardi, A., Marino, M., and Sabatini, R., “Hybrid-electric propulsion integration in unmanned aircraft,” *Energy*, vol. 140, 2017, pp. 1407–1416. DOI 10.1016/j.energy.2017.05.183vc
- [21] Hung, J., and Gonzalez, L., “On parallel hybrid-electric propulsion system for unmanned aerial vehicles,” *Progress in Aerospace Sciences*, vol. 51, 2012, pp. 1–17. DOI 10.1016/j.paerosci.2011.12.001
- [22] Riboldi, C. E., “An optimal approach to the preliminary design of small hybrid electric aircraft,” *Aerospace Science and Technology*, vol. 81, 2018, pp. 14–31.. DOI 10.1016/j.ast.2018.07.042

- [23] "DA-100L." Desert Aircraft, www.desertaircraft.com/collections/da-engines/products/da-100l.
- [24] Wilson, S. (2011). INTELLIGENCE ADVANCED RESEARCH PROJECTS ACTIVITY (IARPA) - Office of Smart Collection, Great Horned Owl (GHO) Program, Proposers' Day Overview Briefing, IARPA-BAA-11-12, August 15
- [25] T. Rotramel, "Optimization of Hybrid-Electric Propulsion Systems for Small Remotely-Piloted Aircraft," MS Thesis, Air Force Institute of Technology, Department of Aeronautics and Astronautics, March 2011.
- [26] K. McKinney, "Evaluation of Hybrid-Electric Power System Integration Challenges for Multi-Rotor UAS," MS Thesis, Oklahoma State University, School of Mechanical and Aerospace Engineering, 2018. <https://hdl.handle.net/11244/317806>
- [27] K. McKinney, J. Feight, R. Gaeta, J. Jacob, "Implementation Implications of Hybrid Electric Power Systems on Multi-Rotor UAS", AIAA 2018-0986, 2018 AIAA SciTech Forum, Kissimmee, FL, 8-12 January 2018.
- [28] Hays, T., "High Energy Density Propulsion System Dynamometer for Small Engines" MS Thesis, Oklahoma State University, School of Mechanical and Aerospace Engineering, 2009.
- [29] K. Rouser, N. Lucido, M. Durkee, A. Bellcock, and T. Zimbelman, "Development of Turboelectric Propulsion and Power for Small Unmanned Aircraft", AIAA 2018-4618, 2018 AIAA Joint Propulsion Conference, Cincinnati, OH, 9-11 July 2018.
- [30] Mattingly, J., and Boyer, K., Elements of Propulsion: Gas Turbines and Rockets, 2nd ed., AIAA Education Series, AIAA, New York, 2016. DOI 10.2514/4.103711
- [31] Hughes, A., Electric Motors and Drives Fundamentals, Types and Applications, 3rd ed., Elsevier Science, Burlington, MA. 2006.
- [32] Serway, R., and Jewett Jr., J., Physics for Scientist and Engineers with Modern Physics, 9th ed., Brooks/Cole, Boston, 2014.

- [33] Moody, K., Replogle, C., and Rouser, K., “Design, Characterization, and Integration of a Turboelectric Power System for Small Unmanned Multirotor Aircraft,” AIAA 20194460, AIAA Propulsion and Energy 2019 Forum, Indianapolis, IN, 19-22 August 2019
- [34] Moody, K., Replogle, C., and Rouser, K., “” ASME Journal of Engineering for Gas Turbines and Power, GTP-19-1749. 2019 (accepted, ready for publication)
- [35] M. and C. Wisniewski, “Development and Analysis of a Group 1 UAV Series Hybrid Power System with Two Engine Options,” AIAA 2016-5011, 52nd AIAA/SAE/ASEE Joint Propulsion Conference, Salt Lake City, UT, 25-27 July 2016.
- [36] Mattingly, J., Heiser, W., Boyer, K., Haven, B., Pratt, D., Aircraft Engine Design, 3rd ed. AIAA Education Series, AIAA, New York, 2018, DOI 10.2514/4.105173
- [37] Aström, K. and Murray, R., “Feedback Systems: An Introduction for Scientists and Engineers, draft v2.4a.” 2006.
- [38] Rashid, M., Power Electronics: Circuits, Devices & Applications, 4th ed., Pearson Education, New York. 2014
- [39] “Mugin Plus 4500mm Plane Frame Kit.” Mugin UAV, www.muginuav.com/product/new-mugin-plus-4500mm-plane/.
- [40] “Engine Data Sheet Without Prices.” Chief Aircraft, 14 July 2015, www.chiefaircraft.com/pdf/jetcat-data.pdf.
- [41] *Three Phase Bridge, 130 A to 160 A*, Vishay Semiconductors, 17 August, 2017. [online] <https://www.mouser.com/datasheet/2/427/vs-130mt80k-1769090.pdf>
- [42] Nelson, R., Flight Stability Automatic Control, 2nd ed., McGraw-Hill Education, New York, 1997.

APPENDICES

APPENDIX A: MULTIROTOR INTEGRATION

After examining the viability of the study and the factors that would contribute to the controllability of the finalized system, the turboelectric system was integrated into the xFold Travel 12 dodeca-copter. As expected, there were multiple design challenges that occurred during the process, so multiple iterations were made off the initial design. Prior to design, fabrication and integration of the components, a notional static stability and control analysis was performed to see where the effects of gyroscopic coupling would come into play.

A.1 Stability and Control Considerations

There is some concern regarding gyroscopic effects when designing a multirotor which is powered from a turboelectric system. This concern necessitates the need to perform a stability and control analysis. Euler's equations for rigid body dynamics suggest that rigid bodies with multiple degrees of freedom will experience gyroscopic effects due to the angular momentum of rotating internal components. Because of this, the expected torque and angular momentum must be evaluated to thoroughly assess the handling and control characteristics of the integrated vehicle. The fundamental equations can be shown in Eqs. 57-60, where H_T is the turbine angular momentum, I_T is the turbine mass moment of inertia tensor, ω_T is the turbine shaft speed, and τ_T is the turbine torque.

$$\tau_T = I_T \dot{\omega}_T \quad (57)$$

$$H_T = I_T * \omega_T \quad (58)$$

$$\tau_T = \begin{vmatrix} I_T \dot{\omega}_T \\ 0 \\ 0 \end{vmatrix} \quad (59)$$

$$H_T = \begin{vmatrix} I_T \omega_T \\ 0 \\ 0 \end{vmatrix} \quad (60)$$

It is important to note that the orientation of the turbine on the body will govern in which axis the gyroscopic coupling will occur for the body, as rotations will couple in axes perpendicular to the axis of angular momentum. Mounting constraints on the lower chassis determined the turbine will be mounted parallel to the vehicle roll axis, or x-axis. The values of inertia, shaft speed, and angular momentum for the turboelectric power generation system can be seen in Table 11. Torque is dependent on how quickly the shaft speed is changing, thus cannot be estimated at this time and only appears as a transient term. Note these values are approximated based on weights and estimate angular speeds for a common mission power setting.

Table 11. Turboelectric power generation system values of inertia, and angular momentum

Component	Inertia (lbm-ft²)	Angular Speed (RPM)	Angular Momentum (lbm-ft²-s⁻¹)
Turbine Core	0.000087	130000	1.45
Generator	0.066	4200	29.11

Little has been attempted with integrating turbine engines on multirotors, so very little is known about the dynamics at play. Knowing these relationships will allow quantification of inertial parameters which effect the stability and control of the vehicle as well as the structural design. To evaluate this, a model was developed for flight conditions with and without the turboelectric system included. The tuning of the autopilot would likely need to be adjusted, however this model will evaluate the stability of the system with the current tuning and determine the magnitude of changes to be made. A few assumptions were made to simplify the model, such as the mission profile. The mission profile was simplified to a hover endurance mission, as was done in the mission analysis. This allows drag terms to be neglected as a significant contributing

factor to moments and also allows simplification of the dynamic moment derivation to a static moment derivation. The model begins with Euler’s equations for a rigid body rotating in free space, the equation of motion for the system appears as it does in Eq. 61, where M is the aerodynamic moment vector, I is the body inertia tensor, H_b is the body angular momentum vector, and ω_b is the body angular rate vector about the principle axes. The cross product is a result of differentiating the body frame in the inertial frame of reference.

$$\tau_b = I_b \dot{\omega}_b + \omega_b \times H_b \quad (61)$$

The principle axes can be shown in Fig. 44 where X, Y, and Z correspond to the roll, pitch, and yaw axes, respectively.

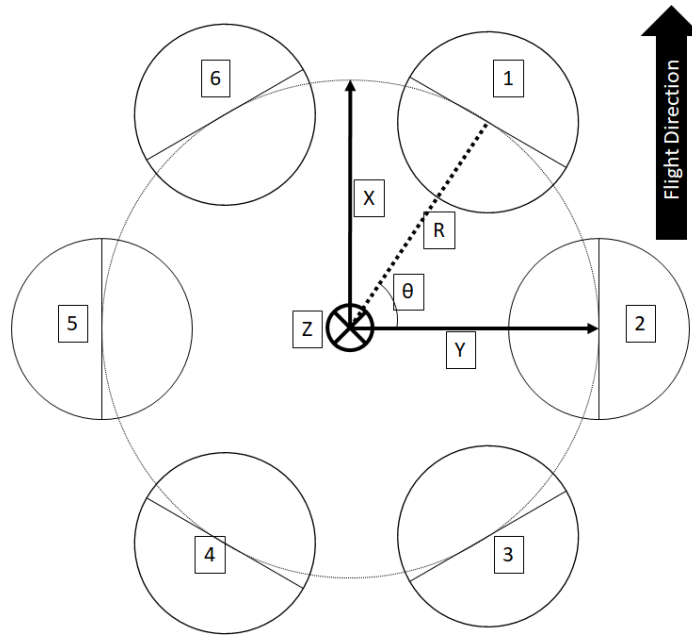


Figure 44. Free body diagram of the dodecacopter used in the stability and control analysis

Using τ_b to show the moments in each principle axis, the equation simplifies to the form as shown in Eq. 62, where the torque of the turbine, τ_T , is included. The inertia tensor, I , can be shown in Eq. 63. The products of inertia, I_{xy} , and I_{yz} , can be neglected as the multicopter is symmetric about the roll-yaw plane. The x-z product of inertia cannot be neglected for the case with the turbine included as the body is no longer symmetric about the y-z plane. Inclusion of this product will add additional nonlinearities to the model with the turboelectric system. Lastly, the

angular momentum of the body, H_b , can be shown in Eq. 65, which includes the turbine angular momentum.

$$\tau_b = \begin{bmatrix} R\cos(\gamma)(T_6 + T_4 - T_3 - T_1) + R(T_5 - T_2) \\ R\sin(\gamma)(T_1 + T_6 - T_4 - T_3) \\ 0 \end{bmatrix} + \tau_T \quad (62)$$

$$I_b = \begin{bmatrix} I_{xx} & 0 & -I_{xz} \\ 0 & I_{yy} & 0 \\ -I_{xz} & 0 & I_{zz} \end{bmatrix}_b \quad (63)$$

$$\omega_b = \begin{bmatrix} \omega_x \\ \omega_y \\ \omega_z \end{bmatrix}_b \quad (64)$$

$$H_b = \begin{bmatrix} I_{xx} & 0 & -I_{xz} \\ 0 & I_{yy} & 0 \\ -I_{xz} & 0 & I_{zz} \end{bmatrix}_b \begin{bmatrix} \omega_x \\ \omega_y \\ \omega_z \end{bmatrix}_b + \begin{bmatrix} I_T \omega_T \\ 0 \\ 0 \end{bmatrix} = \begin{bmatrix} I_{xx}\omega_x + I_T\omega_T - I_{xz}\omega_z \\ I_{yy}\omega_y \\ I_{zz}\omega_z - I_{xz}\omega_x \end{bmatrix} \quad (65)$$

Solving this equation for ω_b and evaluating, as shown in Eq. 66, yields a system of first order, highly coupled nonlinear differential equations. These equations agree with Nelson's [42] model for an aircraft rotating in free space superimposed with several additional terms from the inclusion of the turbine.

$$\dot{\omega}_b = I_b^{-1}(\tau_b - \omega_b \times H_b) \quad (66)$$

It is important to note the gyroscopic coupling of the turbine with the pitch and yaw motions; these nonlinear terms fall out of the cross product as a result of the turbine angular momentum. Though still nonlinear, if the xz product of inertia can be assume negligible the equation can be simplified further, however at this time this assumption cannot be verified. If the stability of the vehicle were to be assessed in detail, the nonlinear model would have to be linearized about an equilibrium point and the roots analyzed. The roots of the system, or eigenvalues, would have to be assessed on the linearized model which must include the autopilot stability augmentation system (SAS) gains. Detailed analysis of overall vehicle control is beyond the scope of this study; the purpose of developing a control matrix is to see the rough order of magnitude gyroscopic effects and where they will appear. If a detailed analysis is required for

future considerations, the real part of the eigenvalue (with the inclusion of the SAS control matrix) must be negative, indicating an asymptotically stable node.

A.2 Design Rational

The focus for the project was the design of the shelf, which supports all the turbo-electric components. A few high-level requirements assisted the design and physical constraints. The shelf must be able to support all of its equipment with the exception of a fuel tank (that will be located on the body of the platform), ensuring minimal additional resources would be utilized from the platform, in this case volume. Additionally, the exception allows the turboelectric integration into most platforms ensuring non-obstructing airflow for the jet, while fuel tanks could be utilized to offset that center of gravity (c.g). For the future of the project and to support testing and analysis on multiple platforms, the shelf must retain minimal volume. Two of the major platform types for testing are fixed wing aircrafts and multirotors. Also, the shelf must be designed for ease of accessibility for all of its components, providing ease of maintenance and troubleshooting. Finally, the shelf must have a minimum FOS (Factor of Safety) of 2.0, to ensure the robustness of overall hardware, as well as the project.

For the xFold platform specifically, there are two major mounting considerations taken into account. The shelf must be mounted below platform's c.g., giving increased stability assuming no changes are made to autopilot tunings. Additionally, this mounting consideration ensures exhaust from the jet will have minimal effects on aerodynamics of the platform. The other consideration was having a minimal difference between overall c.g. with the shelf, including all its components, and c.g. of the platform itself, also, ensuring minimal aerodynamic changes to the platform.

A.2.1 *Revision 1: Fitment and Installation Check*

The first revision is the integration check of the system. A majority of the first iteration was designed and assembled in CAD, derived from the theoretical concepts. The chosen material

for the shelf is the birch plywood. This material is very well known for its durability, due to its manufacturing processes. It has multiple layers allowing the stresses and forces to be evenly distributed in both directions. Birch plywood contains a small number of knots or jagged edges, compared to other types of wood, making it less likely to fail. Furthermore, due to its wide range of use in carpentry, birch plywood is very economical. All the structural parts were manufactured and laser cut using this material. Basic analytical calculations suggested that the back plate would take the majority of the force, therefore most likely to be cause of the failure, if one were to occur. The estimated, or calculated, weight of the shelf (plywood structure) was 1.08 lbs. Post assembly, the measured shelf weight was 1.15 lbs. The reason for 0.07 lbs. of differential is believed be the addition of adhesive utilization for connective purposes, as well as manufacturing imperfections. The finished first iteration can be seen in Figure 45.

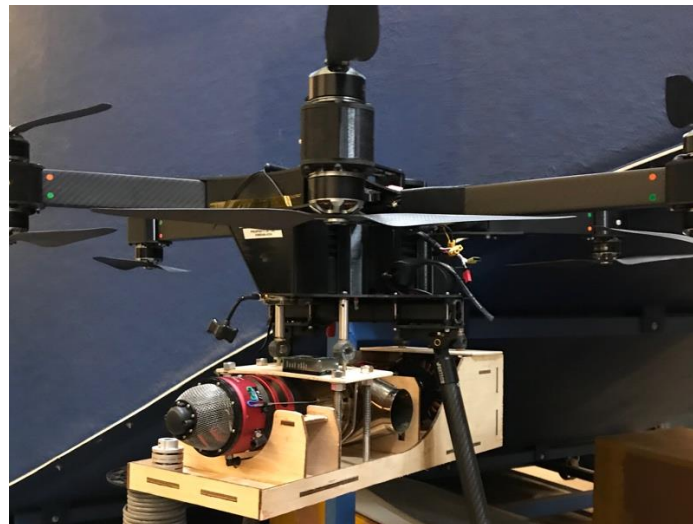


Figure 45. First iteration for turboelectric integration

A.2.2 Revision 2: Revised Fitment Issues/Weight Reduction

The second revision, as seen in Fig. 46, addressed the technical issues encountered in first, and was formed from a collaboration with all involved parties to ensure the project objectives were met. The choice of material for the shelf was kept the same, for reasons stated in previous revision. Major changes for the shelf included the addition of lightening holes to reduce

weight and a minor reconfiguration of parts, to idealize the c.g. location as much as possible. The first revision and calculations made it clear that plywood was performing its intended task exceptionally, especially for the back plate which took majority of the torque produced by the generator due to the shaft connection. With all the changes and previous revision error taken into a consideration, the estimated weight of the shelf was 1.01 lbs. Post assembly, the measured weight of the shelf was 1.09 lbs. A differential of 0.08 lbs. of error is believed to be caused by reason stated in revision one. Following assembly, The major concern was direct jet exhaust exposure to the platform's legs. A thermal experiment was conducted to verify initial assumption regarding flow mixing and structural integrity of the platform, as explained the following section.

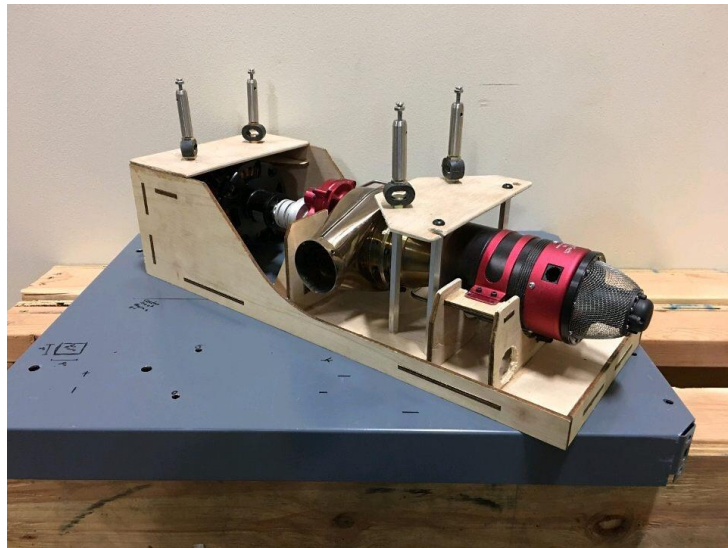


Figure 46: Second iteration for turboelectric shelf

A.2.3 Revision 3: Future System

The third revision will build on the baseline of revision two with the lessons learned during fabrication. Once again, the purpose of revision three is to address issues encountered in revision two with material choice of carbon fiber to significantly reduce the weight of the overall system. The carbon fiber laminate with plywood core mixture is intended to provide similar strength while reducing the weight with high strength ratios. Furthermore, the carbon fiber could easily be integrated with different types of material, but plywood will be used for this

project. Utilization of exotic material increases the manufacturing cost, but it can easily be offset by the performance of the overall system. This also means the manufacturing process must be heavily quality controlled. An additional benefit of using carbon fiber laminate is its exceptional heat resistance. Although heat is not a major concern for the shelf due to its current placement, this combination leaves options for future work to aggressively reduce weight via reintegration without the worry of thermal destruction. With the changes solely in the materials, the estimated weight should be reduced by 40%, based on mass density differential between carbon fiber and birch plywood. In addition, it is recommended to add two 90° downward jet exhaust ducts, per FLIR thermal testing in following section.

A.3 Structural Analysis

After completing the integration design, the structural integrity was analytically and experimentally examined. Much of the analysis for the design was simplified due to time and inability to perform dynamic, experimental tests. For greater accuracy in calculating the c.g for the turboelectric system (and the dodecaopter), each component was weighed. The c.g location for each component was measured from the component c.g to the back plate of the shelf, which was chosen as the datum for the shelf. The moments from each component were summed to find the shelf c.g location in the x direction. For the z direction, the c.g was estimated directly in the middle of the shelf because the components are symmetrical across the z axis. Table 12 shows the c.g locations in the x and z axis along with the total weight of the shelf.

Table 12: Final revision shelf characteristics

<i>x c.g. Location (in)</i>	7.97
<i>z c.g. Location (in)</i>	-6.00
<i>Shelf Weight (lbf)</i>	14.21

The turboelectric system is attached to the dodecaopter by four stainless steel bolts. After examining similar projects, the team decided the bolts would be the weakest portion of the

integration system. Because there are more iterations that will change the shelf material in the future of the project, the weak points of the shelf (such as the back of the shelf) were not examined. It is assumed that the final material will result in the bolts continuing to be the weakest portion of the structure. Loads from the shelf are acting on the bolts in tension, and there is a shear on the bolts due to motor torque and the weight of the shelf when the dodecacopter is tilted on an axis. All four bolts are attached to the dodecacopter away from any edge that could initiate edge cracking. On the turboelectric platform, the bolts are screwed into aluminum standoffs that have yield values above the bolts. The direct stress on each bolt, calculated using the total weight of the shelf and the location of the bolts in reference to the datum, can be seen in Table 13 with a loading factor, LF, of 2.5. Based on the material properties of stainless steel, the static direct stress has a safety factor of over 100. Though the system is able to safely hang from the dodecacopter, the bolts allow for easy removal for travel and storage.

Table 13. Direct stress on bolts in static case

<i>Bolt Number</i>	<i>Load (lbf)</i>	<i>Direct Stress (psi)</i>	<i>With LF of 2.5 (psi)</i>	<i>Bolt Yield Load (psi)</i>	<i>Safety Factor</i>
1	3.158	225.6	451.2	30000	133
2	3.158	225.6	451.2	30000	133
3	3.948	282.0	563.9	30000	106
4	3.948	282.0	563.9	30000	106

Table 14 shows the results from calculations performed for the worst-case shear stress on the structural bolts attaching the turboelectric system to the dodecacopter platform. The worst case for shear stress is when the platform is flying at a 45-degree angle with a loading factor of 2.5. In that moment, the bolt experiences the most force perpendicular to its longitudinal axis because that is the steepest angle of flight for the dodecacopter. Due to a lack of experimental data and an incomplete control matrix, the shear stress due to motor and generator torque could not be included. But the safety factor being over 28 on all four bolts encourages the assumption

that the bolts will be able to withstand the inclusion of the motor and generator torques in the worst-case shear.

Table 14: Shear stress on bolts in worst case scenario

Bolt Number	Shear Stress (psi) With LF of 2.5 (psi)	Bolt Shear Yield (psi)	Safety Factor
1	296.3	592.5	35.44
2	296.3	592.5	35.44
3	370.3	740.6	28.35
4	370.3	740.6	28.35

Table 15 shows the results from calculations performed for the von Mises stress considerations using the direct stress, shear stress, and preload stress. The preload stress, σ_{PL} , was calculated using Eq. 67, which provides an estimated preload stress value for bolts in nonpermanent joints using the tensile yield strength, S_{ty} . Eq. 68 was used to calculate the von Mises stress, σ_{vM} , on each of the bolts using the direct stress, σ_t , and shear stress, τ_{sh} with a loading factor, LF of 2.5. The safety factor of over 5 for each bolt provides a cushion for the assumptions that could not be calculated due to incomplete data.

$$\sigma_{PL} = 0.64S_{ty} \tag{67}$$

$$\sigma_{vM} = \sqrt{(\sigma_{PL} + LF * \sigma_t)^2 + (3 * LF * \tau_{sh})^2} \tag{68}$$

Table 15: von Mises stress calculations for bolts, worst-case scenario loading

Bolt Number	Von Mises Stress (psi) With LF of 2.5 (psi)	Allowable Stress (psi)	Safety Factor
1	1017	4585	6.54
2	1017	4585	6.54
3	1240	5731	5.23
4	1240	5731	5.23

Torque is a factor that cannot be dismissed in the structural analysis but do to the control system remaining incomplete at the end of the project timeline, the complete effects of the torque

due to acceleration or deceleration from the turbine, generator, and rotors could not be calculated. As long as the system functions properly, there should be equal and opposite torques from the power turbine and the generator on the turboelectric system. With the high safety factors for the bolts in the worst-case situations, it can be assumed that the resultant force due to torque will not exceed the bolt yield strength.

A.4 Thermal Considerations

Post integration of the first revision, the xFold's leg structural integrity became a major concern among the advisors and all involved parties, due to direct exposure of extreme temperature from the jet exhaust. Placing the jet 12 in. forward from the c.g. of the platform brought the overall c.g. within flight acceptable region. Inadvertently, it created the issue of exposing the leg to extreme temperatures of 620°C at turbine exhaust. Initial assumptions were that the airflow from the propellers mixing with the jet exhaust would reduce the temperature significantly, roughly 300°F, to not have any structural integrity issues. Even though this assumption is important for this platform only, it was imperative to verify.

To verify the assumptions, an experimental apparatus was manufactured for the worst case scenario, as illustrated in Figure 47. The worst-case scenario is its startup sequence, starting the jet engine first, followed by platform's propellers, prior to any type of mixing. The legs were built to scale with tolerances of 0.25in. using PVC pipes. Just as a real flight, the shelf and all necessary hardware were mounted to the testing plate on top of PVC legs. The material of choice for the legs was PVC pipes, due to a melting temperature that is half of the xFold's leg material as well as availability and cost. If PVC pipe were to show major signs of failure, then current configuration would not comply, by the FOS for the platform's legs.

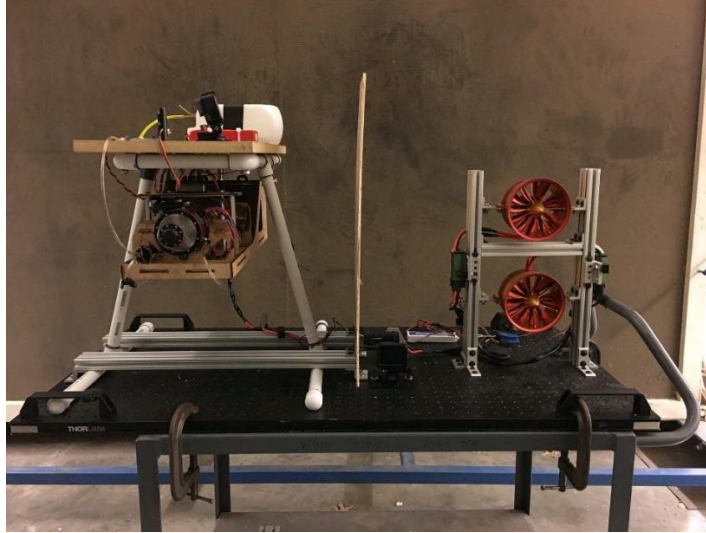


Figure 47. Complete assembly for thermal testing

For the testing, the experiment was to be run as if it were a real flight, bringing the jet engine to maximum throttle causing the maximum temperature possible. The experiment was stopped when clear signs of burning and structure failure were noted, as displayed in Figs. 48 and 49. The burning occurred immediately after the engine was brought out of idle, so it was clear that changes were required to make the setup viable for flight.

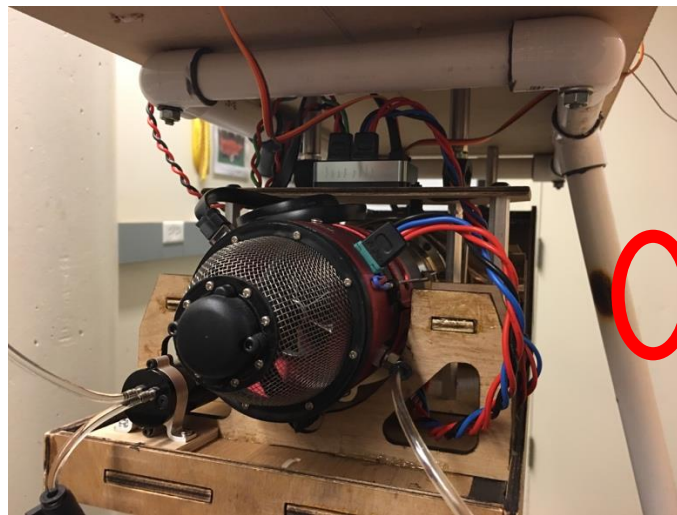


Figure 48. Experimental leg platform damage during thermal testing

The FLIR thermal camera exhibited the direct exposure of core jet exhaust on the platform's leg. Figure 48 and 49 display high and low temperature gradients of jet exhaust and

the legs. It was clear that without continuous flow from platform's propellers the legs will not comply by FOS.

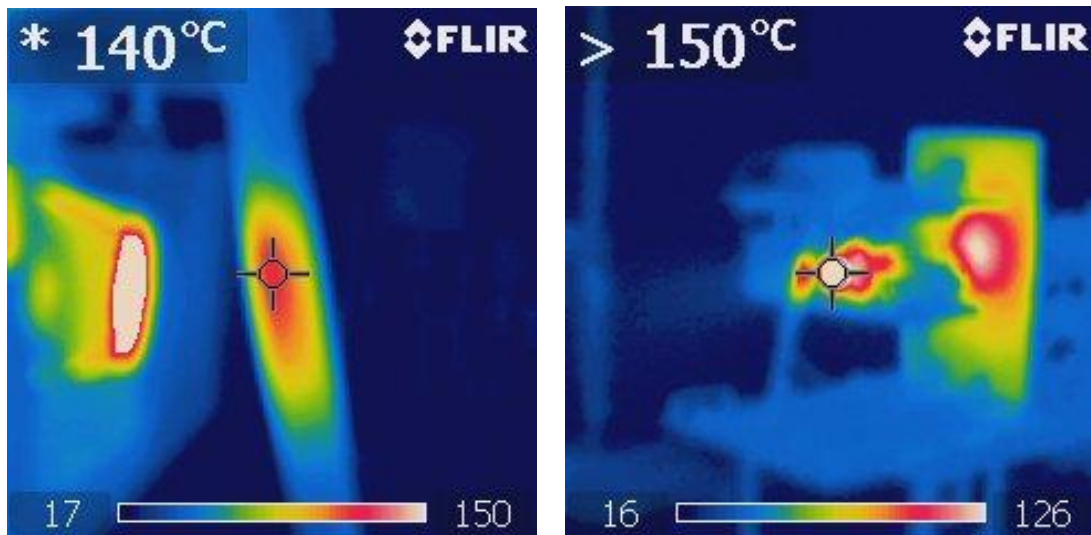


Figure 49. Thermal Imaging data from xFold integration test on mock-up stand

For Revision 3: Future work, it is recommended to duct the flow downward. This change will definitely cause additional weight to be added, but it's much safer and easier compared to reconfiguration of the system on the shelf to maintain c.g. within flight acceptable region of the platform.

A.5 Test Flight

A test flight was performed to create a baseline battery endurance and pilot controllability on the xFold platform, along with evaluating structural integrity of the shelf. Evaluation of the baseline flight test would provide key values to be examined for this project. The objective of this test was to evaluate the assumptions, theoretical vs. tested values, and support integration of revision one, as described in the previous section. Important baseline values to be gained were the endurance of the platform with all systems attached, as platform take-off weight was then equal to the mission weight for this project. As seen in Fig. 50, the jet and rest of the components were attached to the platform, but the turboelectric system was not powered on because the purpose of the baseline test flight was to achieve endurance value to compare against the theoretical value

and future flight tests. The theoretical endurance, for this configurations, is 19.5 minutes. Due to locational difficulties, and lack of practice flying with the new c.g. for the platform, the endurance was not able to be evaluated effectively. This was unfortunate, but there was still valuable information learned from the test.

The turboelectric system was also not powered so the pilot could establish a basic evaluation of stability effects due to lowering platform's overall c.g. and create a controllability baseline. The controllability of the platform was theoretically derived utilizing stability and control equations [42], as illustrated in the previous section. Furthermore, equations 62-65 show that with the turboelectric system not running, the controllability of the platform would not be compromised in steady and level flight, validating the assumption. The controllability aspect of the flight test was analyzed using pilot's perspective, as full effect analysis would require further research which would be out of scope for this effort. From the pilot's perspective, the platform was increasingly stable and flew nominally. Throughout the course of the project, the pilot was the same and controlled variable to be accurate as possible. Another important aspect of this test, parallel to purpose of revision one, was the structural integrity aspect. The shelf was designed and manufactured utilizing the FOS described in the previous sections, yet it was imperative to ensure the structure would hold together for any forces from the platform. After the flight test, it was determined there were no signs of structural integrity issues.

In conclusion, the baseline test flight was nominal as it met all objectives and gained baseline values to be compared against for future testings. Furthermore, this test also gave confidence to all parties involved, that the turboelectric system has advantageous controllability effects and no adverse effects on the shelf and its components from the platform. Future testings are recommended to ensure adverse effects on the platform due to the self and its components, specifically the jet.



Figure 50. Weight and structural flight test

VITA

Kylar Julian Moody

Candidate for the Degree of

Master of Science

Thesis: DESIGN, ANALYSIS, AND INTEGRATION OF A TURBOELECTRIC
PROPULSION AND POWER SYSTEM FOR UNMANNED
AIRCRAFT

Major Field: Mechanical and Aerospace Engineering

Biographical:

Education:

Completed the requirements for the Master of Science in Mechanical and
Aerospace Engineering at Oklahoma State University, Stillwater, Oklahoma in
May, 2020.

Completed the requirements for the Bachelor of Science in Mechanical
Engineering and Aerospace Engineering at Oklahoma State University, Stillwater,
Oklahoma in 2018.

Experience:

Research Assistant with Oklahoma State University, Aerospace Propulsion and
Power.

Professional Memberships:

AIAA Student Member, ASME Student Member

